Development of Photothermal Optical Coherence Tomography for *In Vivo* Imaging of Contrast Agents

By

Jason Tucker-Schwartz

Dissertation

Submitted to the Faculty of the

Graduate School of Vanderbilt University

in partial fulfillment of the requirements

for the degree of

DOCTOR OF PHILOSOPHY

in

Biomedical Engineering

August, 2015

Nashville, Tennessee

Approved:

Melissa Skala, PhD

Craig Duvall, PhD

E. Duco Jansen, PhD

Sharon Weiss, PhD

Thomas Yankeelov, PhD

ACKNOWLEDGEMENTS

There are too many people to thank, but I will certainly try. First, the work in this dissertation was completed with the gracious assistance of numerous colleagues and advisers. Their knowledge and contributions were essential to the research and made me a better scientist. For that, I am incredibly thankful.

Thank you to my adviser Dr. Skala. Her knowledge in the field of biomedical optics and substantial donation of advising time was essential to both the success of this research and my training. Dr. Skala's well-rounded and comprehensive training allows me to leave Vanderbilt feeling confident in a broad set of skills. I would also like to thank each of the additional members of my committee for their thoughtful guidance and generous contributions of time. Dr. Duvall was an integral collaborator, providing essential knowledge and assistance in nanoparticle development and applications. Dr. Jansen's expertise in laser-tissue interactions and *in vivo* systems, as well as his general familiarity and experience with the fields of biomedical optics and imaging were crucial. Additionally, Dr. Jansen provided significant additional counseling in professional development. Dr. Weiss provided essential experience and knowledge in nano-photonics and photonics instrumentation. Finally, Dr. Yankeelov's extensive knowledge of molecular imaging, specifically *in vivo* preclinical and clinical imaging, was vital to the research.

I want to give a very special thank you for the hard work and contributions of each of the co-authors of my publications. Each of you went above and beyond to make sure our research was of the highest quality, and lent me a significant portion of your time. For that, I thank you. No research is done alone, and this work would never have happened without your gracious assistance.

I'd like to add an additional and special thank you to Dr. Chetan Patil, a research professor in our lab. He provided significant hands on expertise, advising, and assistance in OCT. He is a valued colleague and friend who was and continues to be incredibly helpful and supportive.

A Ph.D. is an exciting and intellectually stimulating pursuit, but is not without its difficulties. I am forever in debt to everyone who helped me through the long days and nights, encouraged me when things were difficult, and cheered me up when I needed it most. My friends, both within and outside of the Vanderbilt community, are an incredibly valuable support system, and I love you all. I'd particularly like to acknowledge Isaac, Christine, Amy, Kelsey, and Spencer for being so encouraging and helpful throughout the years at Vanderbilt. Outside of Vanderbilt, my friends from childhood, high school, and college to this day continue to be an incredible support system that allowed me to succeed at Vanderbilt.

I'd like to thank my entire family for their support, guidance, and love. My parents have always encouraged my brother and me to enjoy life and also excel at what we love to do. It is for these reasons that my brother and I both pursued Ph.D. degrees. My parents demonstrate to me every day how to be exceptional as professionals, and more importantly as people. Their love and support has been around forever, and it is the reason that I feel confident when I embark into new and uncharted territory. Additionally, my brother has paved the way for me on some many fronts, from athletics to academics. His experience and support has always made me feel comfortable when I begin new adventures, and this Ph.D. was no different.

Last, but absolutely not least, thank you to my wife, Monica. She is my best friend and my rock. She is the one who is there by my side on a daily basis, and she has never wavered. Monica is the most loving, strong, supportive, and fun person I have ever known. Her love and support is unconditional, and her thoughtfulness knows no bounds. Every day I spend with her makes me truly happy, and her love and support gives me the drive to work hard and excel. Thank you Monica.

TABLE OF CONTENTS

Appendix

LIST OF TABLES

Table

LIST OF FIGURES

Figure

CHAPTER 1

Introduction

1.1 Motivation

Molecular and functional imaging in living animals is commonly used to study diseases including cancer and cardiovascular disease that cause the greatest burdens of morbidity and mortality in the developed world [1-3]. When performed at high resolution, *in vivo* optical imaging can identify fine spatial differences in pathological expression, drug delivery, and treatment response that are critical for understanding and treating these diseases [4-6]. In cancer in particular, high resolution imaging is essential for capturing spatial heterogeneities in molecular expression and the tumor microenvironment that cause significant barriers to treatment efficacy and drug delivery [7, 8]. Confocal and multiphoton microscopy (fluorescence, scattering, absorption, etc.) have been the standard for high resolution (<1 μm) functional and molecular imaging in living systems [5, 6], although their imaging depths are limited to a few hundred micrometers. Wide field optical imaging techniques, including bioluminescence and fluorescence imaging, supply sensitive imaging of target agents over large centimeter fields of view in animals, but with poor spatial resolution in the millimeter regime. Magnetic resonance imaging (MRI) and nuclear imaging techniques are standards for functional imaging without any practical limitations to depth penetration. However, MRI instrumentation is prohibitively expensive with limited molecular sensitivity, while nuclear methods require ionizing radiation and are limited to millimeter scale spatial resolution [3, 9]. The overall goal of this dissertation is to develop a high resolution and wide field of view imaging system to noninvasively track contrast agents and drug delivery vectors in preclinical animal models in three dimensions at depths greater than microscopy, with a particular focus on cancer.

Optical coherence tomography (OCT) fills a unique spatial niche between high resolution

optical microscopy and lower resolution whole body imaging techniques. With micrometer scale spatial resolution and penetration depths greater than 1 mm, OCT can allow for both cellular-level resolution and penetration depths in tissue that exceed microscopy [10]. This three-dimensional, non-invasive imaging technique provides an especially attractive scale for monitoring mouse models of disease and can provide tissue morphology [11], blood vessel morphology [12], and blood flow information [13]. These capabilities make OCT a valuable tool for preclinical imaging of diseases such as cancer where tissue and vessel morphology are key biological parameters in the study of disease [14]. However, contrast in standard OCT images is based on differences in scattering cross section and refractive index, both of which are mostly minimal and nonspecific amongst molecular species in tissue and contrast agents. Therefore, it remains a significantly active area of interest to supplement standard OCT images with sensitive and specific molecular contrast.

This dissertation develops photothermal OCT (PTOCT) for *in vivo* imaging of a variety of contrast agents and drug delivery vectors in live animals. PTOCT leverages the photothermal heating phenomenon, where photon absorption by an imaging target leads to a temperature change in the surrounding microenvironment. These local temperature changes cause thermoelastic expansion of the sample and shifts in the local index of refraction, both of which can be imaged with OCT in the presence of background tissue scattering [15]. This work aims to 1) characterize and optimize instrumentation for the use of PTOCT in live animals, 2) demonstrate advantages of *in vivo* PTOCT by tracking the pharmacokinetics of nanoparticles in cancer models in the context of tissue and vessel morphology, and 3) attempt to increase the throughput of PTOCT and perform real time imaging. The development of *in vivo* PTOCT combined with existing morphological and hemodynamic imaging capabilities of OCT will enable more comprehensive studies of drug delivery and molecular expression in mouse models of disease, particularly cancer.

1.2 Specific Aims

Aim 1: Characterize and optimize PTOCT for *in vivo* imaging using gold nanorods. A standard spectral-domain OCT system was altered for PTOCT imaging, and the behavior of the photothermal signal was characterized and compared to an analytical model of heating. PTOCT imaging was then demonstrated in solid phantoms containing gold nanorods, a nanoparticle contrast agent and drug delivery vector under heavy development for cancer applications. Finally, trace concentrations of gold nanorods were localized from within tissue by *in vivo* PTOCT imaging in a live mouse.

Aim 2: Image spatial heterogeneities of intra-tumor gold nanoparticle delivery *in vivo* using PTOCT. Female nude mice with dorsal window chambers and 4T1 mammary tumors were injected with polyethylene glycol (PEG)-coated gold nanorods. PTOCT images were collected over a number of time points to confirm nonspecific uptake of the nanoparticles due to the enhanced permeability and retention effect in tumors, alongside images of tissue and vessel morphology. The biodistribution as a function of space and time in the tumors was compared across multiple mice, and the specificity of the imaging signal was verified using multiphoton microscopy. Using cancer as a model application system, this Aim demonstrates the feasibility for future preclinical studies investigating drug delivery and molecular imaging of contrast agents.

Aim 3: Apply optical lock-in techniques to increase throughput and allow for real time *in vivo* imaging of multiple contrast agents. Optical lock-in techniques allow for real time PTOCT imaging and can potentially reduce scan and signal processing times for increased throughput *in vivo* PTOCT studies. Acousto-optic modulators were integrated into the system to generate frequency shifts in the reference arm matched to the photothermal amplitude modulation frequency. Frequency shifting the reference arm signal allowed for real time differentiation of the modulated background signal from the demodulated photothermal signal to supply the

photothermal optical lock-in OCT (poli-OCT) signal. The poli-OCT signal was assessed with respect to imaging parameters and the optimal shot-noise limited mode of operation was verified at millisecond integration times. The effects of motion artifact and blood flow on the poli-OCT system were characterized, and *in vivo* feasibility was demonstrated with local injections of gold nanorods and indocyanine green, an FDA approved small molecule fluorophore.

1.3 Dissertation Outline

This dissertation has been organized in the following manner:

Chapter 1 offers an introduction and motivation for the dissertation, additionally supplying an overview of the Specific Aims.

Chapter 2 provides background on the role of preclinical molecular and functional imaging in medicine and particularly cancer, an overview of existing preclinical imaging modalities, a technical description of OCT and the need for augmented contrast, and introductory details of PTOCT.

Chapter 3 reports the technical insight required for *in vivo* imaging using PTOCT, and demonstrates its sensitivity to gold nanorods. This work provides the fundamental insights that allow PTOCT to be used for sensitive and specific imaging of contrast agents *in vivo* and the groundwork for future *in vivo* imaging studies. This work was published in *Biomedical Optics Express* in 2012 [16].

Chapter 4 contains an example *in vivo* application of PTOCT: noninvasive tracking of drug delivery vectors in the context of tissue and vessel morphology in preclinical models of cancer. Gold nanorods, under development as contrast agents and drug delivery vectors for cancer, were injected intravenously and tracked over time in multiple mice. The work in Chapter 4 demonstrates the strengths of PTOCT, its potential for further *in vivo* studies, and a benchmark *in vivo* study for

future comparison. This work was published in *Biomedical Optics Express* in 2014 [17].

Chapter 5 demonstrates the use of optical lock-in techniques to potentially accelerate the imaging and analysis speed of PTOCT for real time *in vivo* imaging. Replacing the post-acquisition frequency analysis of PTOCT with the real time optical lock-in analysis of poli-OCT can potentially increase throughput compared to PTOCT. For the work presented in Chapter 5, poli-OCT instrumentation was built, the signal was characterized, and *in vivo* imaging was performed using an FDA approved fluorophore, another class of contrast agent that PTOCT can effectively image. In addition, gold nanorod injections were imaged similar to Chapter 3, at ten times faster scan speeds and in real time. This work was published in *Biomedical Optics Express* in 2015 [18].

Chapter 6 includes a set of concluding remarks. The concluding remarks summarize the work found throughout the dissertation, suggest future directions of research, and point out some of the scientific contributions of the work.

Appendix A identifies a third class of contrast agent to which PTOCT is sensitive: carbon nanotubes. A carbon-based nanoparticle containing iron caps, carbon nanotubes both absorb photons and exhibit superparamagnetic characteristics that make them responsive to PTOCT and MRI, respectively. The sensitivity of carbon nanotubes to both imaging modalities at relevant *in vivo* concentrations was verified, and a multi-scale phantom was imaged to demonstrate the complementary strengths of MRI and PTOCT. This work was published in *Optics Letters* in 2012 [19].

1.4 References

1. World Health Organization., *Global status report on noncommunicable diseases 2010* (World Health Organization, Geneva, Switzerland, 2011), pp. ix, 162 p.

2. M. de Jong, J. Essers, and W. M. van Weerden, "Imaging preclinical tumour models: improving translational power," Nat Rev Cancer **14**, 481-493 (2014).

3. J. K. Willmann, N. van Bruggen, L. M. Dinkelborg, and S. S. Gambhir, "Molecular

imaging in drug development," Nat Rev Drug Discov **7**, 591-607 (2008).

4. A. Marusyk, V. Almendro, and K. Polyak, "Intra-tumour heterogeneity: a looking glass for cancer?," Nat Rev Cancer **12**, 323-334 (2012).

5. A. J. Walsh, R. S. Cook, H. C. Manning, D. J. Hicks, A. Lafontant, C. L. Arteaga, and M. C. Skala, "Optical Metabolic Imaging Identifies Glycolytic Levels, Subtypes, and Early-Treatment Response in Breast Cancer," Cancer Res **73**, 6164-6174 (2013).

6. G. M. Thurber, K. S. Yang, T. Reiner, R. H. Kohler, P. Sorger, T. Mitchison, and R. Weissleder, "Single-cell and subcellular pharmacokinetic imaging allows insight into drug action in vivo," Nat Commun **4**(2013).

7. R. K. Jain, L. L. Munn, and D. Fukumura, "Dissecting tumour pathophysiology using intravital microscopy," Nat Rev Cancer **2**, 266-276 (2002).

8. M. R. Junttila and F. J. de Sauvage, "Influence of tumour micro-environment heterogeneity on therapeutic response," Nature **501**, 346-354 (2013).

9. M. L. James and S. S. Gambhir, "A molecular imaging primer: modalities, imaging agents, and applications," Physiological reviews **92**, 897-965 (2012).

10. W. Drexler and J. G. Fujimoto, *Optical Coherence Tomography: Technology and Applications* (Springer, 2008).

11. D. Huang, E. A. Swanson, C. P. Lin, J. S. Schuman, W. G. Stinson, W. Chang, M. R. Hee, T. Flotte, K. Gregory, C. A. Puliafito, and J. G. Fujimoto, "Optical Coherence Tomography," Science **254**, 1178-1181 (1991).

12. A. Mariampillai, B. A. Standish, E. H. Moriyama, M. Khurana, N. R. Munce, M. K. K. Leung, J. Jiang, A. Cable, B. C. Wilson, I. A. Vitkin, and V. X. D. Yang, "Speckle variance detection of microvasculature using swept-source optical coherence tomography," Opt Lett **33**, 1530-1532 (2008).

13. G. J. Liu, A. J. Lin, B. J. Tromberg, and Z. P. Chen, "A comparison of Doppler optical coherence tomography methods," Biomed Opt Express **3**, 2669-2680 (2012).

14. B. J. Vakoc, D. Fukumura, R. K. Jain, and B. E. Bouma, "Cancer imaging by optical coherence tomography: preclinical progress and clinical potential," Nat Rev Cancer **12**, 363-368 (2012).

15. M. C. Skala, M. J. Crow, A. Wax, and J. A. Izatt, "Photothermal optical coherence tomography of epidermal growth factor receptor in live cells using immunotargeted gold nanospheres," Nano Lett **8**, 3461-3467 (2008).

16. J. M. Tucker-Schwartz, T. A. Meyer, C. A. Patil, C. L. Duvall, and M. C. Skala, "In vivo photothermal optical coherence tomography of gold nanorod contrast agents," Biomedical optics express **3**, 2881-2895 (2012).

17. J. M. Tucker-Schwartz, K. R. Beavers, W. W. Sit, A. T. Shah, C. L. Duvall, and M. C. Skala, "In vivo imaging of nanoparticle delivery and tumor microvasculature with multimodal optical coherence tomography," Biomed Opt Express **5**, 1731-1743 (2014).

18. J. M. Tucker-Schwartz, M. Lapierre-Landry, C. A. Patil, and M. C. Skala, "Photothermal optical lock-in optical coherence tomography for in vivo imaging " Biomed Opt Express **6**, 2268-2282 (2015).

19. J. M. Tucker-Schwartz, T. Hong, D. C. Colvin, Y. Xu, and M. C. Skala, "Dual-modality photothermal optical coherence tomography and magnetic-resonance imaging of carbon nanotubes," Optics letters **37**, 872-874 (2012).

CHAPTER 2

Background

2.1 Preclinical Molecular and Functional Imaging

The Role of Preclinical Molecular and Functional Imaging

Sensitive and specific noninvasive *in vivo* imaging of contrast agents and endogenous molecules can supply molecular and functional information in animal models, providing essential insight into mechanisms of disease formation and progression, drug delivery, and treatment response. During the drug discovery process, for example, imaging of treatment response and drug delivery in preclinical (e.g. mouse) models of disease are essential to bridge the gap between exciting *in vitro* discoveries and their potential final application in the clinic (Fig. 2.1) [1, 2]. The ability to noninvasively monitor blood vessel morphology and oxygenation, molecular receptor status of cells, and drug delivery are all examples of molecular and functional imaging that have impacted drug discovery and our understanding of pathophysiology [3, 4]. Furthermore, monitoring these factors from within a live animal allows for the full biological system to remain intact and overcome the obstacles of *in vitro* cellular systems that may not accurately recapitulate blood flow, microenvironment factors, and molecular and cellular diversity, among other considerations [5]. Noninvasive imaging from within live animals also allows for spatial and temporal dynamics to be captured and for each animal to serve as its own control, increasing statistical power and saving time, money, and animal lives in the research setting compared to invasive and destructive imaging [1, 2, 4]. Mouse models in particular, are indispensable and allow drugs to be tested for safety and efficacy prior to human testing and permit researchers to unravel the fundamental causes of disease progression [1, 5]. These factors make molecular and functional imaging in mouse models of disease an essential tool for biomedical research.

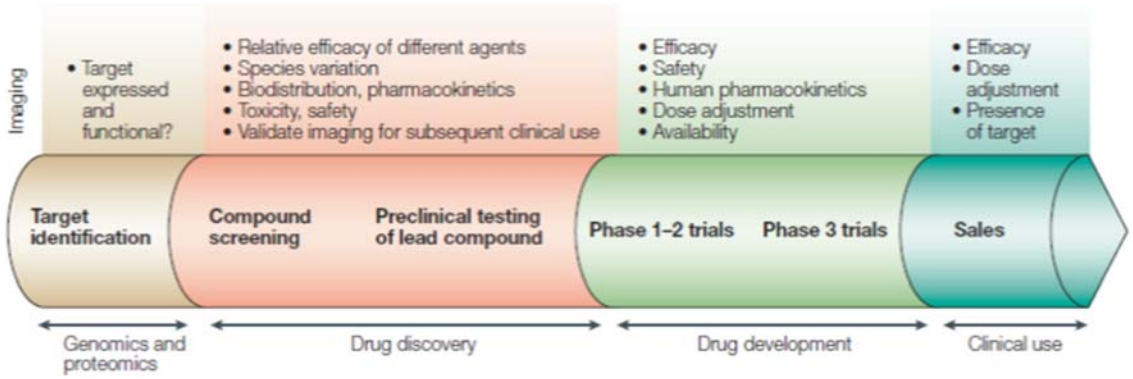

Fig. 2.1. Role of imaging of preclinical disease models in drug development. When developing new drugs for the clinic, exciting new discoveries are often made in cellular *in vitro* systems. However, because of the expense and risk of human clinical trials, preclinical model systems of disease (often in mice) are imaged to test drug efficacy and safety prior to use in humans. Reprinted with permission from [2]. Copyright 2003 Nature Publishing Group.

Imaging the Complexities of Cancer

Although preclinical imaging can supply essential insight into illnesses, there is still room for improvement, particularly in diseases such as cancer. In cancer, cellular-level spatial and temporal heterogeneities in genotype and phenotype are a major source of drug resistance, treatment failure, and ultimately death (Fig. 2.2, top) [6, 7]. For example, breast cancer is the leading form of non-preventable death due to cancer amongst American women with an estimated 40,000 total breast cancer deaths a year in the USA [8, 9]. An important subpopulation of breast cancer patients includes tumors that contain overexpressed, amplified, or mutated human epidermal growth factor receptor 2 (HER2) [10]. Patients with HER2+ tumors most often receive supplementary molecular therapy with anti-HER2 antibody therapy called trastuzumab (Herceptin®) [11, 12]. Herceptin is used to battle the proliferative and aggressive nature of cells overexpressing HER2, and to sensitize the cells to further treatment. However, more than 66% of HER2+ metastatic breast cancers do not respond to, or eventually escape the effects of Herceptin, suggesting *de novo* and acquired mechanisms of drug resistance [12-14]. One reason for the limited success of Herceptin and other molecular therapies is the incomplete knowledge of the dynamic effects of these drugs *in vivo*,

particularly at the molecular scale where heterogeneities in tumor phenotypic expression could directly affect drug efficacy on the tumor mass [15]. Intravital imaging of these cellular level heterogeneities are essential for understanding treatment response in cancer, especially the complex response to multiple drugs in combination, a treatment development strategy currently endorsed by the Food and Drug Administration [16].

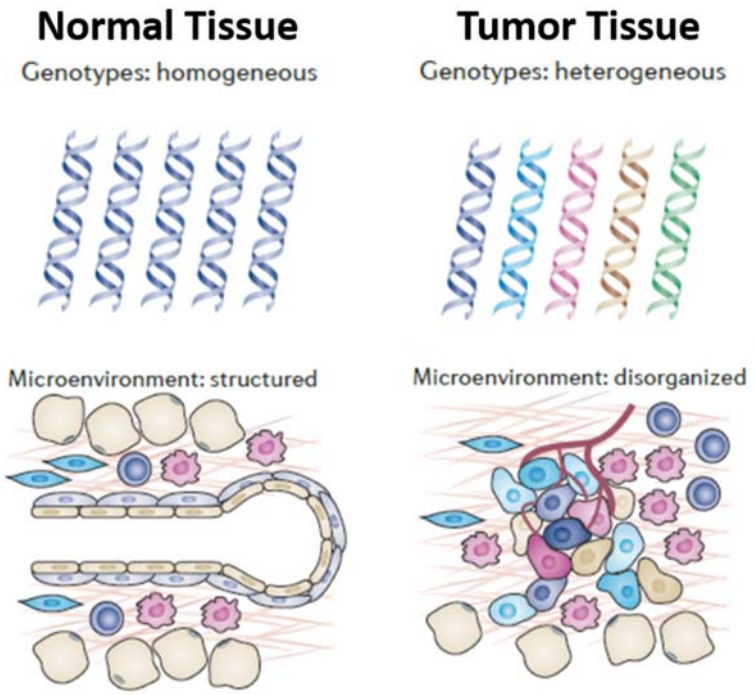

Fig. 2.2. Heterogeneities in cancer. (top) In normal tissue, the underlying genotype and phenotype of a given cellular population are fairly homogenous, while tumor tissue contains a high level of genetic diversity. (bottom) Similar trends are observed in the microenvironment, where normal tissue exhibits highly structured microenvironment features and tumors exhibit heterogeneities and general disorganization in almost all aspects of the microenvironment. These heterogeneities all contribute to tumorigenesis and incomplete treatment response. Reprinted with permission from [7]. Copyright 2012 Nature Publishing Group.

In addition to molecular expression, physical barriers to drug delivery and heterogeneities in the tumor microenvironment can limit treatment effect (Fig. 2.2, bottom). Extracellular matrix composition, interstitial fluid pressure, impaired lymphatic drainage, and vascular permeability all directly impact drug delivery throughout a solid tumor, and all of which exhibit significant spatial and temporal heterogeneities, particularly during treatment [3, 17]. These microenvironment

factors are not just passive consequences of tumor phenotype, but actively contribute to tumor survival and growth [7, 17]. For example, heterogeneities in structural stability and permeability of newly formed tumor vasculature as well as the high and variable interstitial fluid pressure in solid tumors can result in incomplete drug delivery throughout the tumor [18] and hypoxic regions that have in turn been linked to more aggressive tumor features [7, 19]. Observations like these have made tumor vasculature a key point of interest during drug development and studies of cancer pathogenesis [18, 20-24]. However, imaging vasculature or any one other tumor feature alone is often not sufficient to understand treatment response and pathophysiology in cancer since the dynamic interplay between numerous cellular and environmental factors impact drug delivery, tumor survival, and treatment resistance [3, 7].

The heterogeneity and disorganization of solid tumors has led to some positive discoveries, particularly in the development of nanoparticle treatment strategies [25, 26]. In cancer, the sprouting of leaky vasculature containing 100-200 nm pores [20] as well as the impaired function of the lymphatic system allows long-circulating nano-sized particles to preferentially accumulate into tumor tissue, a phenomenon referred to as the enhanced permeability and retention (EPR) effect (Fig. 2.3) [26-29]. Since endothelial cells in healthy tissue do not contain pores large enough to pass nanoparticles of the same size, nano-sized drug carriers present a significant opportunity to achieve high drug load at the tumor and avoid other critical healthy tissues in a patient [26]. In addition, nanoparticle properties can be tuned to aid the transport and increase specificity of otherwise toxic drugs. Nanoparticle drug delivery strategies can incorporate polymer, gold, and a number of other materials into the design, each with their own set of strengths and weaknesses. Biodegradable polymer solutions can degrade safely in the body without the concern of toxic residuals in the patient, and have been FDA approved for some treatment strategies in cancer [26]. Gold nanoparticles are biologically inert and exhibit exquisite photothermal properties that have

led to ongoing clinical trials for controlled release of chemotherapy [30] and for heat-based destruction of tumor cells [31]. However, even though nanoparticles preferentially accumulate into the tumor tissue due to the EPR effect, physical barriers as discussed previously can still inhibit delivery of the treatment throughout the tumor tissue [21, 32]. Imaging the high resolution discrepancies of intra-tumoral nanoparticle uptake and distribution could be key during nanoparticle treatment development and optimization, and for understanding the impact of drug delivery patterns on treatment resistance in tumors. Tracking nanoparticle delivery in tumors is explored more closely in Chapter 4.

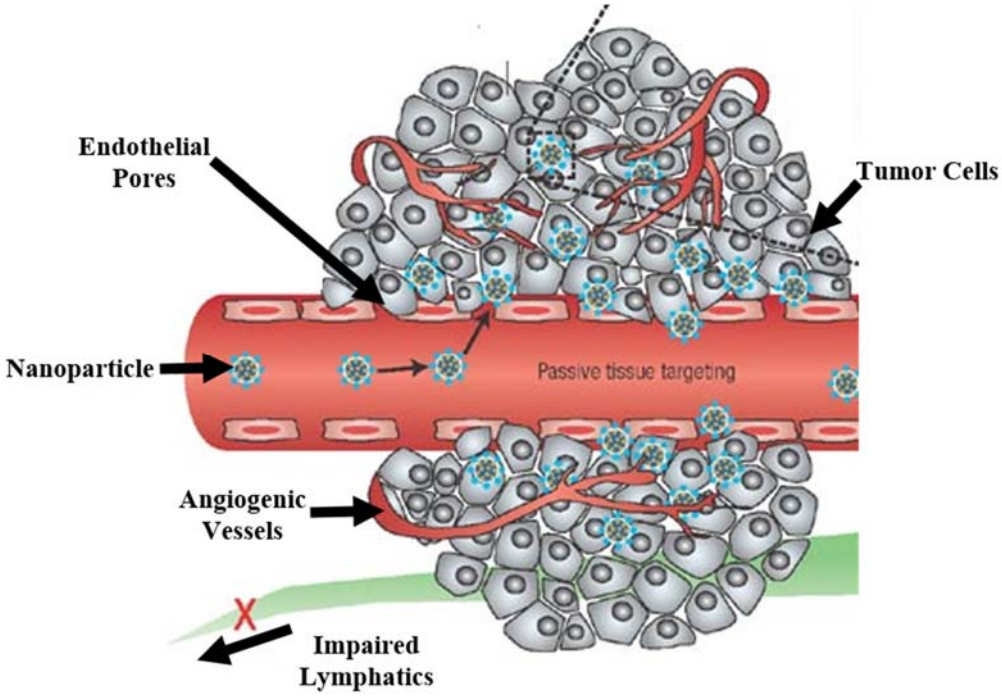

Fig. 2.3. Enhanced permeability and retention of tumors. Long-circulating nanoparticles of a specific size can preferentially accumulate in tumor tissue due to increased permeability of the tumor vasculature and ineffective lymphatic drainage. Reprinted with permission from [29]. Copyright 2007 Nature Publishing Group.

The complexities and spatiotemporal heterogeneities of cancer suggest that *in vivo* imaging of multiple biological endpoints from within the same animal over time is necessary for developing therapeutics and studying cancer pathogenesis [17]. To achieve this goal, there are a number of well-established mouse models of cancer [1] as well as accompanying chronic surgical procedures

that allow direct visualization of the tumor [16]. Surgical excision of the skin and subsequent implantation of transparent windows over the tumor allow for intravital imaging of solid tumors in locations such as the brain, mammary glands, abdomen, and dorsal region [16]. Dorsal window models allow for direct visualization of the underlying tissue with minimal motion artifact, and therefore are often the surgical model of choice for high resolution intravital optical microscopy (Fig. 2.4) [33]. Even with well-established animal models of disease and methods for direct visualization, the complexities and heterogeneities in cancer systems as well as the dynamic interplay between cells, extracellular components, and vasculature makes noninvasively studying drugs, drug delivery, and their treatment effects a daunting task. Therefore, a wide field of view *in vivo* imaging modality that can observe the high resolution dynamics of a variety of imaging endpoints (e.g. tissue structure and viability, microvessel morphology, drug delivery, etc) could be vital for preclinical studies of cancer. The need for such an imaging tool is the basis of the work in this dissertation.

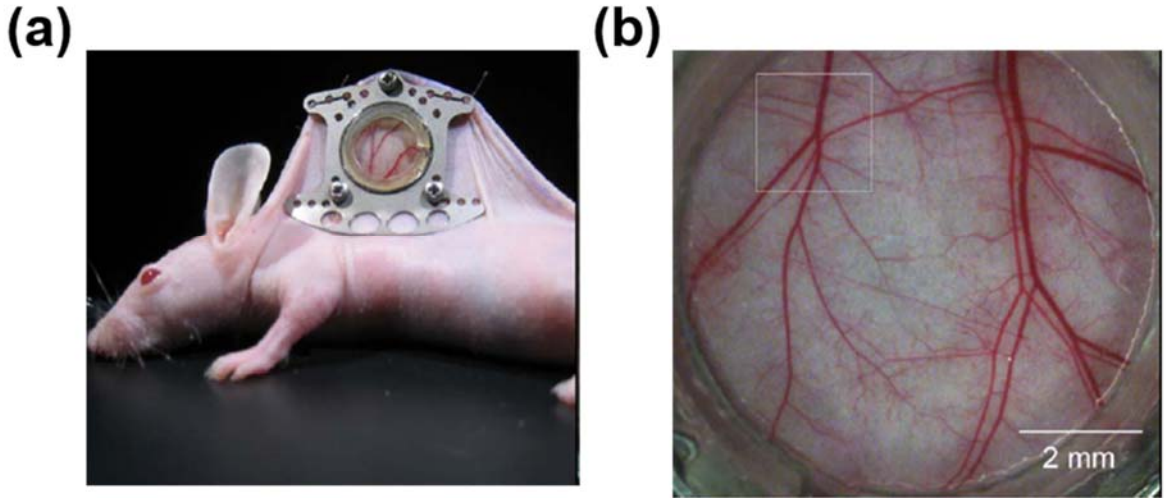

Fig. 2.4. Dorsal window chamber models in mice. Removal of the skin and surgical implantation of a window chamber over the mouse dorsal skin allows for direct visualization of underlying tissue, promoting the use of high resolution intravital microscopy *in vivo*. (a) Photograph of live mouse with dorsal window chamber. (b) Close up of visible tissue from within the window. Reprinted with permission from [34]. Copyright 2008 Optical Society of America.

2.2 Preclinical Molecular Imaging Modalities

Sensitive and specific identification of exogenous contrast agents and endogenous molecules, the basis of molecular and functional imaging, allows for the analysis of a wide range of biological features in tissue. These features can include tissue viability, vessel morphology and flow, drug delivery, and molecular expression among others. Current preclinical molecular and functional imaging modalities span a wide range of image resolution, penetration depth, and capabilities (Fig. 2.5, Fig. 2.6, Table 2.1). Common example imaging modalities include those that are depth-limited due to scattering-based attenuation (e.g. optical microscopy, ultrasonic imaging) and whole body (e.g. MRI, PET/SPECT) techniques. These imaging tools supply molecular and functional information *in vivo* through the identification of contrast agents, drugs, and endogenous forms of contrast.

The highest achievable resolution for *in vivo* imaging is with optical microscopy that can achieve sub-micrometer resolution (Fig. 2.5). Optical microscopy is attractive due to its exquisite sensitivity, wavelength specificity, and range of contrast mechanisms including reflectance, fluorescence, Raman scattering, and absorption [35]. High resolution optical imaging including confocal and multi-photon microscopy offer high resolution (<1 μm) imaging, but are limited by imaging depths of a couple hundred microns [36]. In addition to high resolution microscopy, cost effective lower resolution (1 mm) optical imaging techniques including bioluminescence and fluorescence tomography exist that allow for wide centimeter fields of view [1]. These imaging modalities acquire information from deeper structures and over the length and width of an entire mouse, but lose the high resolution features inherent to optical microscopy and are on a resolution scale that is not well matched to the size of preclinical tumors (< 2 cm) [37].

Another form of depth-limited *in vivo* imaging is ultrasound, a three dimensional imaging modality with deeper penetration than optical microscopy but with lower resolution. Ultrasonic

waves are emitted by a transducer in contact with the sample, and backreflections that occur due to impedance mismatches within the tissue are measured. Although ultrasound is traditionally used as an anatomical imaging tool, molecular and functional imaging can be achieved with the use of microbubble contrast agents. However, extravascular applications are limited due to the relatively large size (micron scale) of the microbubbles [35]. Ultrasound can also be used to measure optical photon absorption events from within tissue, an imaging modality referred to as photoacoustics [38]. In photoacoustics, photons from a pulsed laser are absorbed by a molecule and subsequently cause the tissue to release an ultrasonic wave. The most common form of photoacoustic imaging is photoacoustic tomography, with lateral resolution approaching 0.5 mm and axial resolution of approximately 150 μm at penetration depths of 3 cm. More specialized scanning versions of photoacoustic microscopy can achieve lateral resolution near 50 μm up to depths of 3 mm [38]. Greater depths than optical imaging are achievable with photoacoustic tomography, but photoacoustics requires both optical and ultrasonic instrumentation, direct contact with the sample, and achieves resolution worse than optical microscopy when imaging deep.

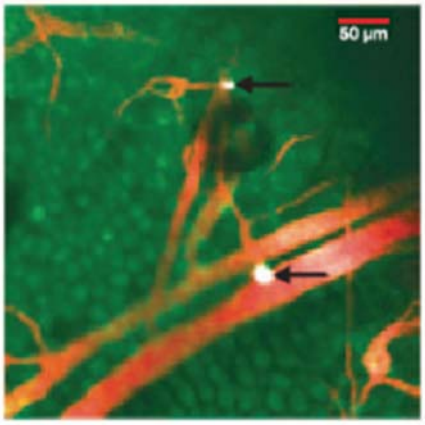

Fig. 2.5. Depth-limited molecular imaging modalities. High resolution intravital optical microscopy imaging of vasculature (red), tumor cells (green), and quantum dots (arrows). Reprinted with permission from [39]. Copyright 2008 American Chemical Society.

Although optical and ultrasonic imaging technologies are limited in their depth penetration due to scattering, a number of alternative molecular imaging tools exist that are not practically limited

by depth. These include positron emission tomography (PET), single photon emission computed tomography (SPECT), and magnetic resonance imaging (MRI) (Fig. 2.6). PET and SPECT rely on radioactive isotopes and are the most common clinical molecular imaging modalities [40, 41]. In PET imaging, a positron emitting isotope attached to a molecular target is injected into the body, and subsequent positron annihilation events release gamma photons in opposing directions that are read by the scanner. Radioactively labeled fluorodeoxyglucose is commonly employed in PET imaging to identify areas of overactive metabolism indicative of tumors and their metastases [35]. SPECT operates under a similar principle to PET, but directly identifies gamma radiation emitted from within the body (Fig. 2.6a). Both PET and SPECT are sensitive on a picomolar concentration scale to radioactive particles (radionuclides) injected into the body and are not hindered by depth, but have poor millimeter scale resolution, are expensive, do not supply anatomical information, and require the use of ionizing radiation. In addition, a cyclotron that produces the radioactive isotopes for injection in PET and SPECT must be readily available, particularly for isotopes with a short half-life.

Another *in vivo* whole body imaging tool used for molecular and functional imaging is MRI. MRI measures water molecule protons using high strength magnetic fields and radiofrequency gradients, and can achieve in-plane resolution below 100 μm with exquisite soft tissue contrast [2]. In addition to its high resolution, a strength of MRI is the tunable contrast that is achievable due to the wide array of pulse sequences. Anatomical structure, blood flow and volume, cellularity, and hypoxia are all measurable with MRI [42]. Additionally, molecular imaging with MRI can be performed (Fig. 2.6b) using specialized contrast agents containing gadolinium [43] or superparamagnetic iron oxide nanoparticles [44, 45]. However, MRI is not especially sensitive to contrast agents when compared to other molecular imaging tools, and the instrumentation is quite expensive [35].

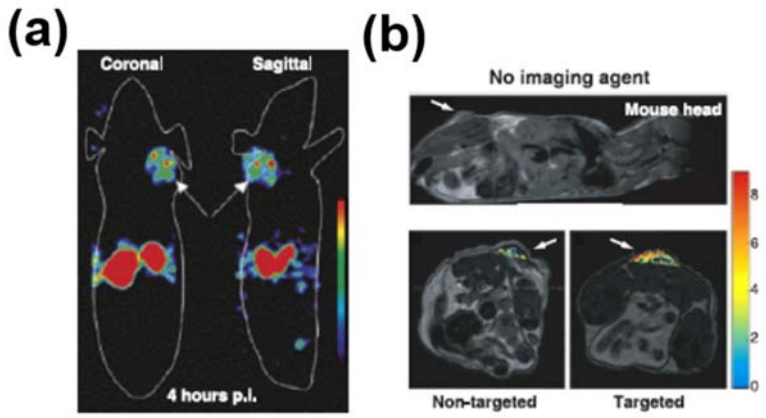

Fig. 2.6. Whole body molecular imaging modalities. (a) SPECT imaging of mice bearing human prostate cancer xenografts. Reprinted with permission from [46]. Copyright 2011 American Chemical Society. (b) MRI images of a mouse glioma using nonspecific (bottom left) and targeted (bottom right) superparamagnetic iron oxide nanoparticles. Reprinted with permission from [47]. Copyright 2008 John Wiley and Sons.

Available preclinical molecular imaging tools allow for a wealth of knowledge to be collected in mouse models of disease (Table 2.1). However, as discussed previously, high resolution heterogeneities of molecular and functional endpoints throughout a solid tumor are key to cancer and its disease progression [3, 5, 7, 17]. Therefore, there is still an unmet need for noninvasive and sensitive high resolution (micrometer scale) molecular and functional imaging tools for cancer in the spatial regime that includes greater imaging depths (>1 mm) and wider fields of view (millimeter scale) than microscopy. In addition, the ability to image multiple functional endpoints including tissue structure/viability, vasculature structure and hemodynamics, molecular expression, and drug delivery with the same tool would allow for more comprehensive studies of cancer and its response to treatment.

Imaging Technique	Spatial Resolution	Depth Penetration	Source of Contrast
Optical Microscopy	>200 nm	<0.4 mm	Fluorescent, scattered, absorbed, Raman scattered light, etc.
Bioluminescence	1-5 mm	< 5 cm	Bioluminescent light
Fluorescence Tomography	1-2 mm	< 5 cm	Fluorescent light
Ultrasound/PA	45-500 um lateral	3 mm - 3 cm	Scattered ultrasonic waves/photon absorption
PET	1-2 mm	no limit	Ionizing radiation
SPECT	0.3 - 1 mm	no limit	Ionizing radiation
MRI	100 μm	no limit	Electromagnetism

Table 2.1. Preclinical molecular imaging modalities. Spatial resolution and depth penetration are variable among the most common preclinical molecular imaging modalities. Adapted from [1, 2, 38].

2.3 Optical Coherence Tomography

Optical Coherence Tomography (OCT) is an interferometric imaging technique that provides high resolution (~1-30 μm) three dimensional images in tissue with deeper penetration than optical microscopy (~1-2 mm), allowing for the evaluation of subsurface morphology and functional features *in vivo* [48]. OCT fills a niche between high resolution microscopy and preclinical ultrasonic imaging techniques (Fig. 2.7). The resolution and penetration depth regime of OCT is ideal for investigating spatial heterogeneities and dynamics in preclinical models of cancer, such as the optically accessible dorsal skin fold mouse window chamber [24]. OCT has also found its way into human use in the clinic, becoming the standard of care for retinal imaging [49] and an emerging tool for intravascular imaging in the field of interventional cardiology [50]. OCT can supply information on anatomical structure [51-54], tissue viability [23, 24], microvessel morphology [34, 55-57], blood flow and velocity [58-61], and other functional characteristics of tissue [62, 63] and contrast agents [64-66].

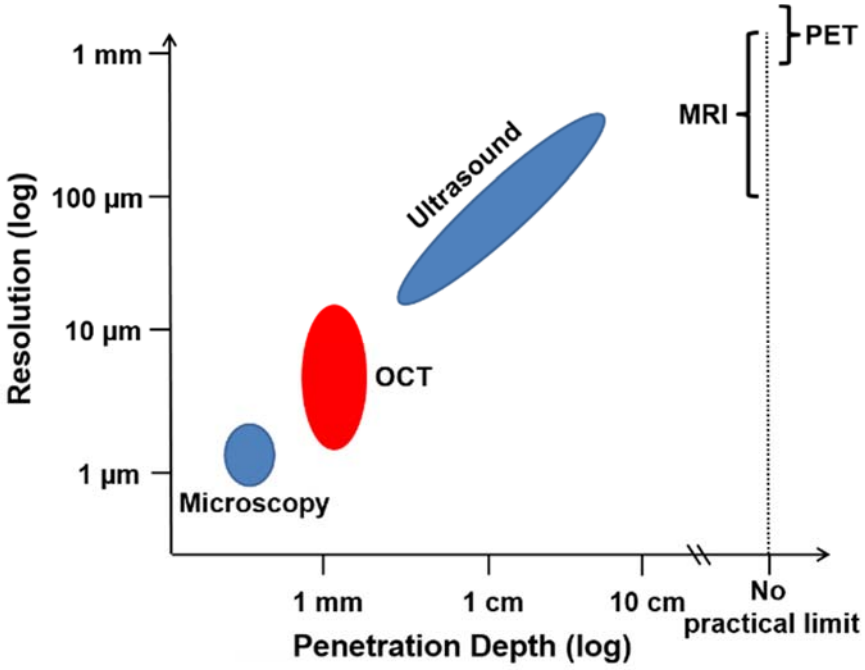

Fig. 2.7. Spatial imaging niche of OCT. OCT (red) occupies a unique niche in imaging allowing for both high resolution (micron scale) and deep (1-2 mm) signal penetration in tissue.

Optical Coherence Tomography Basics

OCT estimates the optical reflectivity profile of a sample by measuring the light scattering events as a function of depth. The optical reflectivity profile is indicative of the tissue microstructure, making OCT images a noninvasive estimate of tissue morphology. As light propagates through a heterogeneous medium such as tissue, the photons can undergo a number of processes including scattering and absorption. When scattered, photons are diverted in any number of directions. OCT shines light into a sample and measures those photons that are back-scattered , similar to how ultrasound measures backreflected ultrasonic waves. However, unlike ultrasound that travels at approximately 1500 meters per second in water and can be timed going into and out of the sample, light travels at hundreds of millions of meters per second. Therefore, the location and intensity of scattering events from within the sample is indirectly measured using interferometry of a low coherence light source [48, 67]. The coherent detection technique employed by OCT allows for high resolution images to be collected at deeper depths than traditional microscopy [48, 68]. In

addition, because optical scattering is more varied across soft tissues than acoustic scattering, OCT supplies greater soft tissue contrast than ultrasound [24].

In low coherence interferometry employed by OCT, a light source composed of many wavelengths is split between two physical paths, towards either a sample or a reference reflector (i.e. a mirror) (Fig. 2.8a). Depth in the sample (i.e. tissue) is gated by resolving the difference in path lengths between scattering locations in the tissue and that of the known reference reflector. If the light travels a similar distance between the two light paths, it creates a sinusoidal pattern of interference as a function of wavenumber (k), the spatial frequency representation of wavelength. When the roundtrip distance the light has traveled is very closely matched, within a few micrometers, the interference pattern is composed of a low frequency sinusoid (yellow, Fig. 2.8). As the distance between the two light paths increases, the frequency of the sinusoidal interference pattern increases as well (red, Fig. 2.8). OCT measures the scattering from all points in depth by the superposition of varying frequency sinusoids in the interference pattern. In spectral-domain OCT (SD-OCT) as used in this dissertation, the complete interference pattern is captured simultaneously by a spectrometer system (Fig. 2.8a). The spectrometer first disperses the light as a function of wavelength (λ) and then digitally acquires the wavelength-dependent data using a charge-coupled device (CCD). Once the digitized spectrometer data is rescaled to be linear as a function of wavenumber (k, where $k=2\pi/\lambda$), a Fourier transform operation reveals the location and relative reflectivity of each scatterer in the sample (Fig. 2.8b). Each acquisition event captured by the spectrometer allows the reflectivity profile of a sample at one lateral position as a function of depth (i.e. one A-scan) to be calculated. The light source incident on the sample is then scanned to different transverse positions using fast tilting galvonometer mirrors to create a two-dimensional scan as a function of lateral position and depth (B-scan) or a three-dimensional image volume (C-scan).

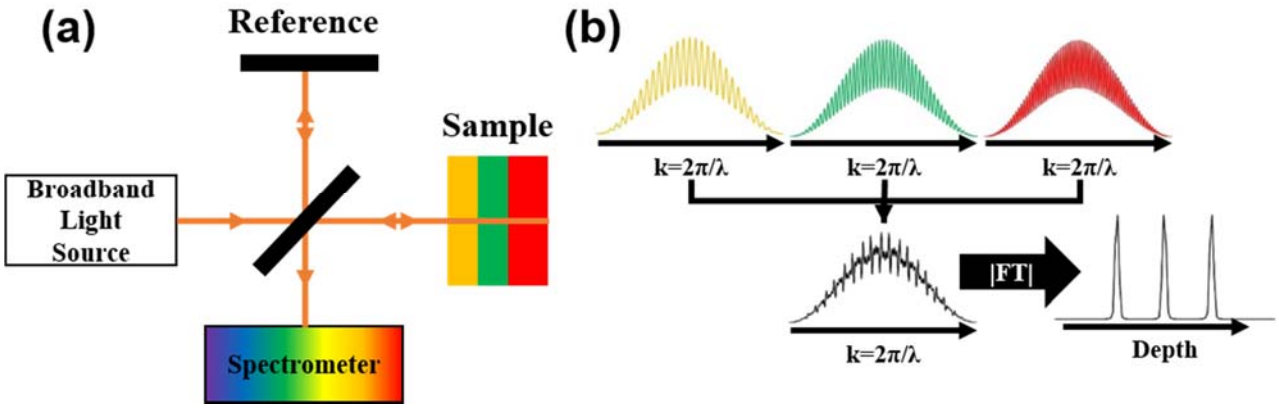

Fig. 2.8. Spectral domain optical coherence tomography basics. (a) In SD-OCT, a broadband light source is split between a sample and reference reflection. The returning light then interferes and is recorded by a spectrometer. (b) As the path length mismatch between the sample and reference increases, so does the frequency of the interference pattern as a function of wavenumber. A Fourier transform (FT) reveals the reflectivity profile as a function of depth.

OCT Governing Equations and Wavelength Selection

Unlike conventional microscopy, the fundamental governing equations for lateral (x-y dimension) and axial or depth (z) resolution in OCT are decoupled [48, 69]. The lateral resolution (Δx) and depth of field (*DOF*) are determined by the focusing optics of the system. The lateral resolution determines the distance limit in the lateral dimension that two points can still be separated in the image, while the depth of field determines how far in the axial dimension an object can shift and remain in focus. For a collimated Gaussian-shaped beam of diameter D and wavelength λ_0, a lens with focal length F will create a focused spot with lateral resolution Δx according to (2.1.

$$\Delta x = \frac{4\lambda_0}{\pi}\frac{F}{\mathrm{D}} \tag{2.1}$$

Using single mode fibers or placing a pinhole in the detection side of the OCT system allows for confocal performance, increasing the lateral resolution even further. The focusing optics also determine the *DOF* of the system, the distance in the depth dimension over which the image remains in focus in the lateral dimension. The *DOF* is calculated according to (2.2.

$$DOF = \frac{8\lambda_0}{\pi}\left(\frac{F}{\mathrm{D}}\right)^2 \tag{2.2}$$

In standard microscopy, the axial resolution is also directly tied to the focusing optics. However, the axial resolution in the depth dimension (Δz) in OCT is determined by the wavelengths of the imaging source [48]. For an imaging source with center wavelength λ_0 and spectral bandwidth of $\Delta\lambda$, the axial resolution of the imaging system is calculated using (2.3.

$$\Delta z = \frac{2ln(2)}{\pi}\frac{\lambda_0^2}{\Delta\lambda} \tag{2.3}$$

According to (2.3, the proper selection of imaging wavelengths is imperative in order to achieve high resolution depth sectioning. Utilizing the shortest possible center wavelength would supply ideally small axial resolution in the sample. However, in tissue, the selection of wavelength is more complex due to light penetration. Tissue is a highly complex medium containing molecular constituents that absorb and scatter photons differently as a function of wavelength. These tissue components include water, blood, and melanin among others. At visible wavelengths (400-700 nm), increased scattering and hemoglobin absorption limit the depth penetration of light (Fig. 2.9). At infrared wavelengths (>1100 nm), water absorption is the limiting factor for light propagation (Fig. 2.9). Therefore, to maximize the image penetration depth of OCT and achieve signal at depths greater than 1 mm (Fig. 2.7), center wavelengths between 800 and 1100 nm in the near infrared optical window are standard choices for OCT systems as well as 1310 nm where there is a decrease in water absorption [67, 70]. These considerations allow OCT to perform high resolution imaging of tissue morphology and structure at depths greater than microscopy, a spatial regime that is ideal for imaging heterogeneities in preclinical models of cancer [24].

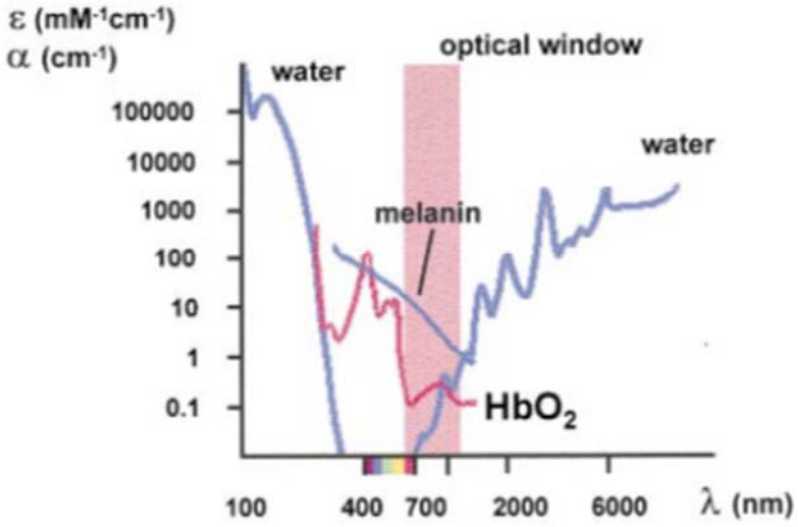

Fig. 2.9. Near infrared optical window. The extinction coefficient of oxygenated hemoglobin and melanin as well as the absorption coefficient of water reveal the range of near infrared wavelengths (the optical window) that penetrate well into tissue. Reprinted with permission from [71]. Copyright 2000 John Wiley and Sons.

Imaging Vessel Morphology and Flow with OCT

In addition to high resolution tissue morphology, OCT can supply microvessel morphology and blood flow information [34, 58, 60, 61] without the need for contrast agents. Doppler OCT is a method for quantitative cross-sectional imaging of microvessel blood flow *in vivo* [72-76]. Doppler shifts arise from motion in the sample (such as flowing erythrocytes in blood vessels), and Doppler OCT identifies this motion through phase-sensitive detection. Phase changes are calculated from multiple A-scans collected at the same position in image space, and phase changes are then related to flow velocity by the angle between the vessel and the incident light source. In addition to quantifying phase changes due to the Doppler shift phenomenon, movement of flowing cells within blood vessels result in fluctuations in the OCT magnitude data. These signal dynamics can be quantified using OCT to identify the locations of the vessels from within tissue. This method, termed speckle variance OCT (SVOCT) [34], can be used to generate high resolution maps of blood vessels in a wide variety of tissues, as demonstrated in the example of imaging a dorsal window (Fig. 2.10). SVOCT is especially advantageous for vessel morphology mapping because it is independent of the

angle between the blood flow and the incident beam, unlike Doppler OCT [34]. Identification of blood vessels using SVOCT is achieved by taking *N* repeated OCT scans at the same position and solving for the variance of the OCT signal at each spatial location ($I(x,y,z)$) over time as in (2.4 [34, 57].

$$SVOCT(x,y,z) = \frac{1}{N}\sum_{i=1}^{N}(I(x,y,z)_i - \overline{I(x,y,z)})^2 \tag{2.4}$$

Both tissue and vessel morphology provide essential insights into disease formation, progression, and treatment response in conditions such as cancer. Unlike high resolution optical microscopy that is depth-limited and requires intravenous contrast agents, OCT can supply repeated label-free images of tissue and vessel morphology over multiple millimeters in the lateral dimension and at depths greater than microscopy. Imaging both of these features at high resolution in preclinical models over a wide field of view has made OCT a valuable tool for understanding cancer [24].

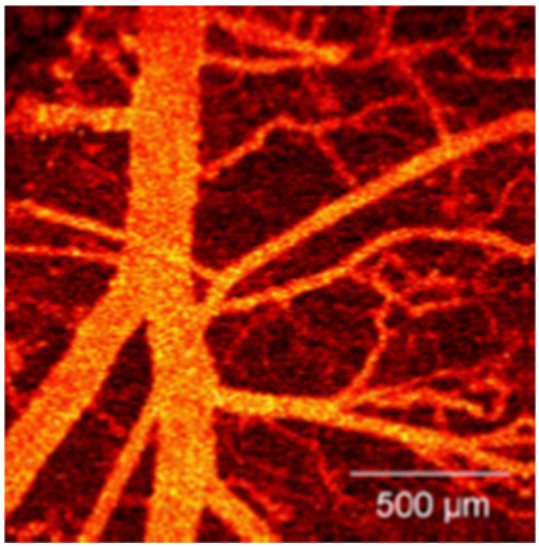

Fig. 2.10. OCT imaging of blood vessels. Speckle variance OCT can be used to create high resolution maps of blood vessels in a dorsal skinfold window. Reprinted with permission from [34]. Copyright 2008 Optical Society of America.

2.4 Enhanced Image Contrast in OCT

OCT is a powerful imaging tool capable of creating label-free high resolution maps of tissue and vessel morphology. However, contrast in standard OCT images is caused by differences in scattering cross section and refractive index, which is minimal and non-specific amongst many endogenous molecular species and exogenous contrast agents. Thus, augmenting standard OCT images with sensitive and specific contrast using exogenous contrast agents represents an area of significant interest in order to take full advantage of OCT's unique spatial imaging regime. There are a number of functional extensions of OCT developed for enhanced imaging contrast and identifying contrast agents from within tissue. Examples include enhanced backscattering OCT [77, 78], spectroscopic OCT [79-81], magneto-motive OCT [64, 82], and photothermal OCT (PTOCT) [65, 66, 70, 83-90]. These functional imaging methods can be separated into passive and active detection techniques (Fig. 2.11) based on their method of contrast enhancement via unperturbed OCT images or imaging of actively perturbed samples, respectively.

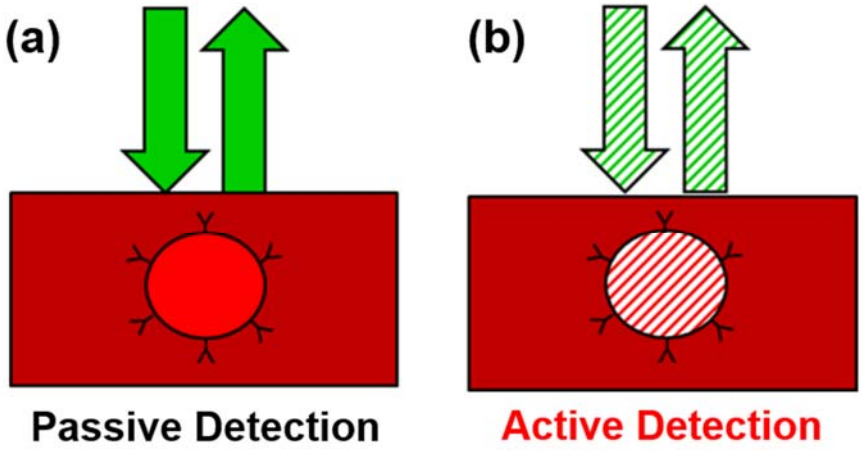

Fig. 2.11. Passive versus active detection of contrast agents. (a) In passive detection methods, the scattering or absorption properties of a source of contrast are identified from within standard OCT images. (b) To enhance sensitivity and specificity, the source of contrast can actively perturb the sample, and those perturbations can be imaged with OCT.

In enhanced backscattering and spectroscopic OCT, standard OCT images are used to passively detect the presence of a molecule of interest (Fig. 2.11a). With enhanced backscattering, contrast

agents with scattering cross sections greater than endogenous tissue molecules increase the brightness in the sample, allowing for an overall verification of the presence of the contrast agent in the image [77]. However, because the tissue also scatters strongly, it is difficult to separate the contrast agent signal from the background signal, giving enhanced backscattering OCT relatively poor specificity. Additionally, if the source of contrast is highly concentrated, this also results in attenuation of the imaging signal [78]. In spectroscopic OCT, the spatial location of varying tissue components, including contrast agents, are calculated from the attenuation of the broadband OCT spectrum using mathematical models (Fig. 2.12a). However, separating absorption from scattering in spectroscopic OCT is difficult to accurately perform, requiring previous knowledge of the tissue constituents. In addition, because the source of contrast must overlap with the imaging beam, the imaging beam is attenuated.

Active detection techniques for increasing contrast in OCT including magnetomotive OCT and PTOCT actively perturb the sample during imaging in order to isolate the source of contrast from within the sample at both high sensitivity and specificity (Fig. 2.11b). In magnetomotive OCT, magnetic field gradients are co-aligned with the OCT imaging beam, and iron oxide contrast agents susceptible to magnetic fields are physically oscillated in the sample during imaging (Fig. 2.12b) [64]. However, the signal strength of the magnetomotive signal is coupled to the viscoelastic properties of the tissue. The elastic resonance frequency at which the signal is strongest is determined by the mechanical properties of the tissue, and is approximately 50-100 Hz, limiting the imaging speed of magnetomotive OCT [64]. The number of available contrast agents is also limited and potential multiplexing of signals would be a challenge.

PTOCT seeks to maximize the potential of molecular and functional imaging with OCT by addressing some of the challenges present in other functional OCT techniques (Fig. 2.12c). First, using all optical instrumentation upgrades, PTOCT is able to identify and separate photon-absorbing

targets from a scattering background with high sensitivity and specificity through active detection of photothermal heating. So long as the imaging contrast does not overlap with the imaging beam wavelengths, PTOCT can perform without compromising OCT imaging depth. Also, in the near infrared optical window (Fig. 2.9), the background photothermal signal is low allowing for exquisite contrast of photothermal absorbers and high sensitivity. PTOCT can also exploit the rapid recent advancements in nanotechnology to develop efficient, molecularly-targeted contrast agents and can be used to track nanoparticle-mediated delivery strategies *in vivo*. For example, gold nanoparticles with near infrared (NIR) plasmon resonance peaks have been investigated for imaging and photothermal therapy and are particularly attractive contrast agents for PTOCT. These nanoparticles include gold nanoshells [91], gold nanorods [92], gold nanocages [93], gold nanostars [94] among others. Finally, photothermal heating is a broadly applicable source of contrast and can be used to image a range of endogenous and exogenous sources of contrast, three of which (gold nanoparticles, near infrared fluorophores, and carbon nanotubes) will be discussed throughout this dissertation. It is these advantages that make PTOCT an especially appealing method to enhance imaging contrast to molecular and functional targets *in vivo*, and the basis for a bulk of the work in this dissertation.

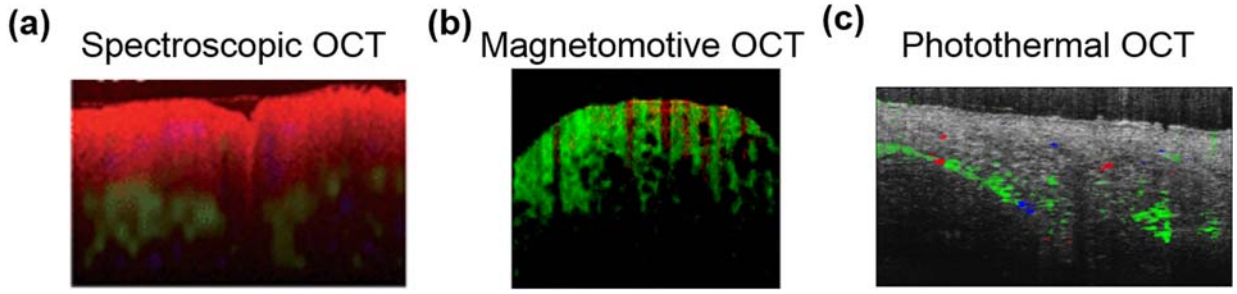

Fig. 2.12. Methods to identify contrast agents using OCT. (a) In spectroscopic OCT, attenuation of the OCT imaging beam by endogenous and exogenous forms of contrast allows for their identification from within tissue. Reprinted with permission from [81]. Copyright 2009 Royal Society of Chemistry. (b) With magnetomotive OCT, fluctuating magnetic fields cause iron oxide nanoparticles to vibrate spatially, movements which OCT can identify. Reprinted with permission from [64]. Copyright 2010 National Academy of Sciences. (c) In PTOCT, photothermal heating of endogenous and exogenous sources of contrasts allows for their identification *in vivo*. Reprinted with permission from [95]. Copyright 2012 Optical Society of America.

2.5 Photothermal OCT

PTOCT images the photothermal effect, the conversion of photon energy to heat by a photon-absorbing molecule. Photon energy can be absorbed by a molecule through the excitation of electrons from a ground state to a higher energy state. Photon absorption is often subsequently followed by non-radiative decay of the photon energy and heat release. The accumulation of photon absorption events causes heating of the microenvironment surrounding the molecule of interest. Water, the major constituent of tissue, has an index of refraction (n) that changes with temperature, while heating also causes thermoelastic expansion and thus alterations to the geometric path length (d) of the sample [96-98]. These heat-induced fluctuations in geometric path length and index of refraction alter the optical path length (OPL) in the sample due to the relationship in (2.5.

$$OPL = \int_0^d n(s)ds \tag{2.5}$$

As discussed in previous sections, OCT measures the interference of low-coherence light between an unknown sample and known reference. In SD-OCT, the interference pattern is directly measured, and, after proper pre-processing steps, a Fourier transform converts the A-scan data to the depth dimension. The magnitude of this Fourier transform operation identifies the location and relative intensity of scattering events in the sample versus depth. However, the phase (Φ) of the OCT data supplies additional sub-resolution information of the sample, and changes (Δ) in the OCT phase over time are directly related to changes in OPL by (2.6 [48],

$$\Delta OPL(t) = \frac{\lambda_0}{4\pi}\Delta\Phi(t) \tag{2.6}$$

where λ_0 is the center wavelength of the OCT imaging beam. Therefore, OCT can directly measure temporal OPL changes in the sample by its phase information. While amplitude modulating a light source incident on the sample, time-modulated photon absorption and subsequent photothermal heat release by a molecule of interest will result in OPL oscillations. These small (typically nanometer

scale) local optical path length changes can be resolved by phase oscillations in the OCT interference data (Fig. 2.13). This physical principle is the underlying source of enhanced contrast in PTOCT, which will be explained thoroughly and demonstrated in the following Chapters. Even with the incredible potential of PTOCT for molecular and functional imaging, no groups prior to this work demonstrated the ability of PTOCT to image contrast agent distributions *in vivo*, which requires proper system optimization and characterization. The work in this dissertation aims to translate the strengths of PTOCT to *in vivo* imaging, fill the gaps in the PTOCT literature, and provide the first demonstrations of *in vivo* PTOCT imaging of multiple contrast agents.

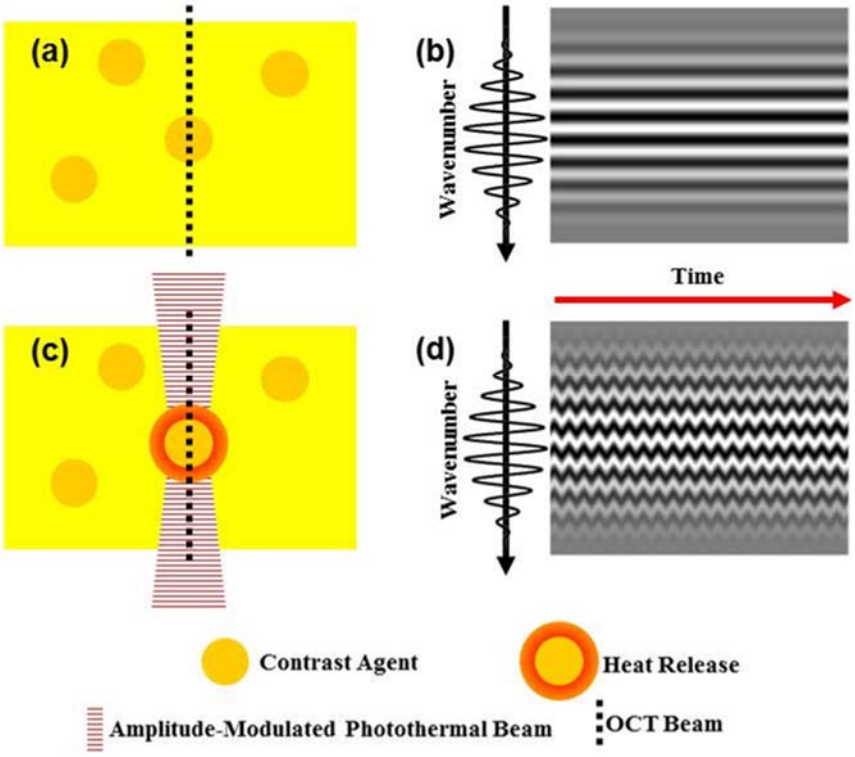

Fig. 2.13. Photothermal heating and its effect on OCT data. (a) Within a sample, the presence of a contrast agent (dark yellow) with a refractive index unequal to the sample will result in (b) a temporally invariant interference pattern detected by OCT. (c) If the contrast agent undergoes temporally modulated photon absorption and thus photothermal heating, (d) the modulations in OPL will cause phase oscillations in the interference pattern.

2.6 References

1. M. de Jong, J. Essers, and W. M. van Weerden, "Imaging preclinical tumour models: improving translational power," Nat Rev Cancer **14**, 481-493 (2014).

2. M. Rudin and R. Weissleder, "Molecular imaging in drug discovery and development," Nat Rev Drug Discov **2**, 123-131 (2003).

3. R. K. Jain, L. L. Munn, and D. Fukumura, "Dissecting tumour pathophysiology using intravital microscopy," Nat Rev Cancer **2**, 266-276 (2002).

4. J. K. Willmann, N. van Bruggen, L. M. Dinkelborg, and S. S. Gambhir, "Molecular imaging in drug development," Nat Rev Drug Discov **7**, 591-607 (2008).

5. A. Ocana, A. Pandiella, L. L. Siu, and I. F. Tannock, "Preclinical development of molecular-targeted agents for cancer," Nature reviews. Clinical oncology **8**, 200-209 (2011).

6. J. Stingl and C. Caldas, "Molecular heterogeneity of breast carcinomas and the cancer stem cell hypothesis," Nat Rev Cancer **7**, 791-799 (2007).

7. A. Marusyk, V. Almendro, and K. Polyak, "Intra-tumour heterogeneity: a looking glass for cancer?," Nat Rev Cancer **12**, 323-334 (2012).

8. American Cancer Society., "Breast cancer facts & figures," (The Society, Atlanta, Ga., 2010).

9. National Breast Cancer Coalition., *Ending breast cancer: A baseline status report* (2011), p. 78 p.

10. D. J. Slamon, W. Godolphin, L. A. Jones, J. A. Holt, S. G. Wong, D. E. Keith, W. J. Levin, S. G. Stuart, J. Udove, A. Ullrich, and et al., "Studies of the HER-2/neu proto-oncogene in human breast and ovarian cancer," Science **244**, 707-712 (1989).

11. D. J. Slamon, B. Leyland-Jones, S. Shak, H. Fuchs, V. Paton, A. Bajamonde, T. Fleming, W. Eiermann, J. Wolter, M. Pegram, J. Baselga, and L. Norton, "Use of chemotherapy plus a monoclonal antibody against HER2 for metastatic breast cancer that overexpresses HER2," N Engl J Med **344**, 783-792 (2001).

12. C. L. Vogel, M. A. Cobleigh, D. Tripathy, J. C. Gutheil, L. N. Harris, L. Fehrenbacher, D. J. Slamon, M. Murphy, W. F. Novotny, M. Burchmore, S. Shak, S. J. Stewart, and M. Press, "Efficacy and safety of trastuzumab as a single agent in first-line treatment of HER2-overexpressing metastatic breast cancer," J Clin Oncol **20**, 719-726 (2002).

13. A. Calabrich, S. Fernandes Gdos, and A. Katz, "Trastuzumab: mechanisms of resistance and therapeutic opportunities," Oncology (Williston Park) **22**, 1250-1258; discussion 1259, 1263 (2008).

14. J. M. du Manoir, G. Francia, S. Man, M. Mossoba, J. A. Medin, A. Viloria-Petit, D. J. Hicklin, U. Emmenegger, and R. S. Kerbel, "Strategies for delaying or treating in vivo acquired resistance to trastuzumab in human breast cancer xenografts," Clinical cancer research : an official journal of the American Association for Cancer Research **12**, 904-916 (2006).

15. H. J. Lee, A. N. Seo, E. J. Kim, M. H. Jang, K. J. Suh, H. S. Ryu, Y. J. Kim, J. H. Kim, S. A. Im, G. Gong, K. H. Jung, I. A. Park, and S. Y. Park, "HER2 heterogeneity affects trastuzumab responses and survival in patients with HER2-positive metastatic breast cancer," American journal of clinical pathology **142**, 755-766 (2014).

16. J. R. Conway, N. O. Carragher, and P. Timpson, "Developments in preclinical cancer imaging: innovating the discovery of therapeutics," Nat Rev Cancer **14**, 314-328 (2014).

17. M. R. Junttila and F. J. de Sauvage, "Influence of tumour micro-environment heterogeneity on therapeutic response," Nature **501**, 346-354 (2013).

18. R. K. Jain, "Taming vessels to treat cancer," Scientific American **298**, 56-63 (2008).

19. M. Paez-Ribes, E. Allen, J. Hudock, T. Takeda, H. Okuyama, F. Vinals, M. Inoue, G. Bergers, D. Hanahan, and O. Casanovas, "Antiangiogenic therapy elicits malignant progression of tumors to increased local invasion and distant metastasis," Cancer cell **15**, 220-231 (2009).

20. S. K. Hobbs, W. L. Monsky, F. Yuan, W. G. Roberts, L. Griffith, V. P. Torchilin, and R. K. Jain, "Regulation of transport pathways in tumor vessels: Role of tumor type and microenvironment," Proc Natl Acad Sci U S A **95**, 4607-4612 (1998).

21. M. R. Dreher, W. G. Liu, C. R. Michelich, M. W. Dewhirst, F. Yuan, and A. Chilkoti, "Tumor vascular permeability, accumulation, and penetration of macromolecular drug carriers," J Natl Cancer I **98**, 335-344 (2006).

22. J. Fang, H. Nakamura, and H. Maeda, "The EPR effect: Unique features of tumor blood vessels for drug delivery, factors involved, and limitations and augmentation of the effect," Advanced drug delivery reviews **63**, 136-151 (2011).

23. B. J. Vakoc, R. M. Lanning, J. A. Tyrrell, T. P. Padera, L. A. Bartlett, T. Stylianopoulos, L. L. Munn, G. J. Tearney, D. Fukumura, R. K. Jain, and B. E. Bouma, "Three-dimensional microscopy of the tumor microenvironment in vivo using optical frequency domain imaging," Nat Med **15**, 1219-U1151 (2009).

24. B. J. Vakoc, D. Fukumura, R. K. Jain, and B. E. Bouma, "Cancer imaging by optical coherence tomography: preclinical progress and clinical potential," Nat Rev Cancer **12**, 363-368 (2012).

25. "Cancer nanotechnology: small, but heading for the big time," Nat Rev Drug Discov **6**, 174-175 (2007).

26. A. Z. Wang, R. Langer, and O. C. Farokhzad, "Nanoparticle delivery of cancer drugs," Annual review of medicine **63**, 185-198 (2012).

27. H. Maeda, "The enhanced permeability and retention (EPR) effect in tumor vasculature: the key role of tumor-selective macromolecular drug targeting," Advances in enzyme regulation **41**, 189-207 (2001).

28. A. K. Iyer, G. Khaled, J. Fang, and H. Maeda, "Exploiting the enhanced permeability and retention effect for tumor targeting," Drug Discov Today **11**, 812-818 (2006).

29. D. Peer, J. M. Karp, S. Hong, O. C. Farokhzad, R. Margalit, and R. Langer, "Nanocarriers as an emerging platform for cancer therapy," Nat Nanotechnol **2**, 751-760 (2007).

30. S. K. Libutti, G. F. Paciotti, A. A. Byrnes, H. R. Alexander, Jr., W. E. Gannon, M. Walker, G. D. Seidel, N. Yuldasheva, and L. Tamarkin, "Phase I and pharmacokinetic studies of CYT-6091, a novel PEGylated colloidal gold-rhTNF nanomedicine," Clinical cancer research : an official journal of the American Association for Cancer Research **16**, 6139-6149 (2010).

31. J. A. Schwartz, A. M. Shetty, R. E. Price, R. J. Stafford, J. C. Wang, R. K. Uthamanthil, K. Pham, R. J. McNichols, C. L. Coleman, and J. D. Payne, "Feasibility Study of Particle-Assisted Laser Ablation of Brain Tumors in Orthotopic Canine Model," Cancer Res **69**, 1659-1667 (2009).

32. L. Tang, T. M. Fan, L. B. Borst, and J. J. Cheng, "Synthesis and Biological Response of Size-Specific, Monodisperse Drug-Silica Nanoconjugates," ACS Nano **6**, 3954-3966 (2012).

33. G. M. Palmer, A. N. Fontanella, S. Shan, G. Hanna, G. Zhang, C. L. Fraser, and M. W. Dewhirst, "In vivo optical molecular imaging and analysis in mice using dorsal window chamber models applied to hypoxia, vasculature and fluorescent reporters," Nat Protoc **6**, 1355-1366 (2011).

34. A. Mariampillai, B. A. Standish, E. H. Moriyama, M. Khurana, N. R. Munce, M. K. Leung, J. Jiang, A. Cable, B. C. Wilson, I. A. Vitkin, and V. X. Yang, "Speckle variance detection of microvasculature using swept-source optical coherence tomography," Opt Lett **33**, 1530-1532 (2008).

35. M. L. James and S. S. Gambhir, "A molecular imaging primer: modalities, imaging agents, and applications," Physiological reviews **92**, 897-965 (2012).

36. J. B. Pawley, *Handbook of biological confocal microscopy,* 3rd ed. (Springer, New York, NY, 2006), pp. xxviii, 985 p.

37. J. Condeelis and R. Weissleder, "In vivo imaging in cancer," Cold Spring Harbor perspectives in biology **2**, a003848 (2010).

38. L. V. Wang, "Multiscale photoacoustic microscopy and computed tomography," Nature

photonics **3**, 503-509 (2009).

39. B. R. Smith, Z. Cheng, A. De, A. L. Koh, R. Sinclair, and S. S. Gambhir, "Real-time intravital imaging of RGD-quantum dot binding to luminal endothelium in mouse tumor neovasculature," Nano Lett **8**, 2599-2606 (2008).

40. M. E. Phelps, "PET: the merging of biology and imaging into molecular imaging," J Nucl Med **41**, 661-681 (2000).

41. F. A. Jaffer and R. Weissleder, "Molecular imaging in the clinical arena," Jama **293**, 855-862 (2005).

42. J. C. Gore, H. C. Manning, C. C. Quarles, K. W. Waddell, and T. E. Yankeelov, "Magnetic resonance in the era of molecular imaging of cancer," Magn Reson Imaging **29**, 587-600 (2011).

43. T. Hyeon and H. B. Na, "Nanostructured T1 MRI contrast agents," J Mater Chem **19**, 6267-6273 (2009).

44. J. W. Bulte and D. L. Kraitchman, "Iron oxide MR contrast agents for molecular and cellular imaging," NMR Biomed **17**, 484-499 (2004).

45. C. Corot, P. Robert, J. M. Idee, and M. Port, "Recent advances in iron oxide nanocrystal technology for medical imaging," Advanced drug delivery reviews **58**, 1471-1504 (2006).

46. H. J. K. Ananias, Z. L. Yu, R. A. Dierckx, C. van der Wiele, W. Helfrich, F. Wang, Y. J. Tan, X. Y. Chen, I. J. de Jong, and P. H. Elsinga, "(99m)Technetium-HYNIC(tricine/TPPTS)-Aca-Bombesin(7-14) as a Targeted Imaging Agent with MicroSPECT in a PC-3 Prostate Cancer Xenograft Model," Mol Pharmaceut **8**, 1165-1173 (2011).

47. C. Sun, O. Veiseh, J. Gunn, C. Fang, S. Hansen, D. Lee, R. Sze, R. G. Ellenbogen, J. Olson, and M. Zhang, "In vivo MRI detection of gliomas by chlorotoxin-conjugated superparamagnetic nanoprobes," Small **4**, 372-379 (2008).

48. W. Drexler and J. G. Fujimoto, *Optical Coherence Tomography: Technology and Applications* (Springer, 2008).

49. M. L. Gabriele, G. Wollstein, H. Ishikawa, L. Kagemann, J. Xu, L. S. Folio, and J. S. Schuman, "Optical coherence tomography: history, current status, and laboratory work," Invest Ophthalmol Vis Sci **52**, 2425-2436 (2011).

50. M. J. Suter, S. K. Nadkarni, G. Weisz, A. Tanaka, F. A. Jaffer, B. E. Bouma, and G. J. Tearney, "Intravascular optical imaging technology for investigating the coronary artery," JACC. Cardiovascular imaging **4**, 1022-1039 (2011).

51. B. W. Colston, Jr., M. J. Everett, L. B. Da Silva, L. L. Otis, P. Stroeve, and H. Nathel, "Imaging of hard- and soft-tissue structure in the oral cavity by optical coherence

tomography," Appl Opt **37**, 3582-3585 (1998).

52. P. A. Testoni, B. Mangiavillano, L. Albarello, A. Mariani, P. G. Arcidiacono, E. Masci, and C. Doglioni, "Optical coherence tomography compared with histology of the main pancreatic duct structure in normal and pathological conditions: an 'ex vivo study'," Dig Liver Dis **38**, 688-695 (2006).

53. A. Popp, M. Wendel, L. Knels, T. Koch, and E. Koch, "Imaging of the three-dimensional alveolar structure and the alveolar mechanics of a ventilated and perfused isolated rabbit lung with Fourier domain optical coherence tomography," J Biomed Opt **11**, 014015 (2006).

54. M. D. Fischer, G. Huber, S. C. Beck, N. Tanimoto, R. Muehlfriedel, E. Fahl, C. Grimm, A. Wenzel, C. E. Reme, S. A. van de Pavert, J. Wijnholds, M. Pacal, R. Bremner, and M. W. Seeliger, "Noninvasive, in vivo assessment of mouse retinal structure using optical coherence tomography," Plos One **4**, e7507 (2009).

55. L. An, T. T. Shen, and R. K. Wang, "Using ultrahigh sensitive optical microangiography to achieve comprehensive depth resolved microvasculature mapping for human retina," J Biomed Opt **16**, 106013 (2011).

56. Y. Jung, Z. Zhi, and R. K. Wang, "Three-dimensional optical imaging of microvascular networks within intact lymph node in vivo," J Biomed Opt **15**, 050501 (2010).

57. A. Mariampillai, M. K. Leung, M. Jarvi, B. A. Standish, K. Lee, B. C. Wilson, A. Vitkin, and V. X. Yang, "Optimized speckle variance OCT imaging of microvasculature," Opt Lett **35**, 1257-1259 (2010).

58. S. Yazdanfar, A. M. Rollins, and J. A. Izatt, "In vivo imaging of human retinal flow dynamics by color Doppler optical coherence tomography," Arch Ophthalmol **121**, 235-239 (2003).

59. R. K. Wang and L. An, "Doppler optical micro-angiography for volumetric imaging of vascular perfusion in vivo," Opt Express **17**, 8926-8940 (2009).

60. Y. Wang, B. A. Bower, J. A. Izatt, O. Tan, and D. Huang, "Retinal blood flow measurement by circumpapillary Fourier domain Doppler optical coherence tomography," J Biomed Opt **13**, 064003 (2008).

61. Y. Wang, A. Lu, J. Gil-Flamer, O. Tan, J. A. Izatt, and D. Huang, "Measurement of total blood flow in the normal human retina using Doppler Fourier-domain optical coherence tomography," Br J Ophthalmol **93**, 634-637 (2009).

62. S. K. Nadkarni, M. C. Pierce, B. H. Park, J. F. de Boer, P. Whittaker, B. E. Bouma, J. E. Bressner, E. Halpern, S. L. Houser, and G. J. Tearney, "Measurement of collagen and smooth muscle cell content in atherosclerotic plaques using polarization-sensitive optical coherence tomography," J Am Coll Cardiol **49**, 1474-1481 (2007).

63. D. Levitz, M. T. Hinds, A. Ardeshiri, S. R. Hanson, and S. L. Jacques, "Non-destructive label-free monitoring of collagen gel remodeling using optical coherence tomography," Biomaterials **31**, 8210-8217 (2010).

64. R. John, R. Rezaeipoor, S. G. Adie, E. J. Chaney, A. L. Oldenburg, M. Marjanovic, J. P. Haldar, B. P. Sutton, and S. A. Boppart, "In vivo magnetomotive optical molecular imaging using targeted magnetic nanoprobes," Proc Natl Acad Sci U S A **107**, 8085-8090 (2010).

65. C. Zhou, T. H. Tsai, D. C. Adler, H. C. Lee, D. W. Cohen, A. Mondelblatt, Y. Wang, J. L. Connolly, and J. G. Fujimoto, "Photothermal optical coherence tomography in ex vivo human breast tissues using gold nanoshells," Opt Lett **35**, 700-702 (2010).

66. M. C. Skala, M. J. Crow, A. Wax, and J. A. Izatt, "Photothermal optical coherence tomography of epidermal growth factor receptor in live cells using immunotargeted gold nanospheres," Nano Lett **8**, 3461-3467 (2008).

67. J. G. Fujimoto, "Optical coherence tomography for ultrahigh resolution in vivo imaging," Nat Biotechnol **21**, 1361-1367 (2003).

68. J. A. Izatt, M. R. Hee, G. M. Owen, E. A. Swanson, and J. G. Fujimoto, "Optical coherence microscopy in scattering media," Opt Lett **19**, 590-592 (1994).

69. J. G. Fujimoto, C. Pitris, S. A. Boppart, and M. E. Brezinski, "Optical coherence tomography: an emerging technology for biomedical imaging and optical biopsy," Neoplasia **2**, 9-25 (2000).

70. D. C. Adler, S. W. Huang, R. Huber, and J. G. Fujimoto, "Photothermal detection of gold nanoparticles using phase-sensitive optical coherence tomography," Opt Express **16**, 4376-4393 (2008).

71. K. Konig, "Multiphoton microscopy in life sciences," Journal of microscopy **200**, 83-104 (2000).

72. J. A. Izatt, M. D. Kulkarni, S. Yazdanfar, J. K. Barton, and A. J. Welch, "In vivo bidirectional color Doppler flow imaging of picoliter blood volumes using optical coherence tomography," Opt Let **22**, 1439-1441 (1997).

73. S. Yazdanfar, M. D. Kulkarni, and J. A. Izatt, "High resolution imaging of in vivo cardiac dynamics using color Doppler optical coherence tomography," Opt Exp **1**, 424-431 (1997).

74. M. C. Skala, A. Fontanella, H. Hendargo, M. W. Dewhirst, and J. A. Izatt, "Combined hyperspectral and spectral domain optical coherence tomography microscope for noninvasive hemodynamic imaging," Opt. Lett. **34**, 289-291 (2009).

75. S. Yazdanfar, A. M. Rollins, and J. A. Izatt, "Imaging and velocimetry of the human retinal circulation with color Doppler optical coherence tomography," Opt Lett **25**, 1448-1450 (2000).

76. S. Yazdanfar, A. M. Rollins, and J. A. Izatt, "In vivo imaging of human retinal flow dynamics by color Doppler optical coherence tomography," Arch Ophthalmol **121**, 235-239 (2003).

77. A. Agrawal, S. Huang, A. Wei Haw Lin, M. H. Lee, J. K. Barton, R. A. Drezek, and T. J. Pfefer, "Quantitative evaluation of optical coherence tomography signal enhancement with gold nanoshells," J Biomed Opt **11**, 041121 (2006).

78. J. C. Kah, M. Olivo, T. H. Chow, K. S. Song, K. Z. Koh, S. Mhaisalkar, and C. J. Sheppard, "Control of optical contrast using gold nanoshells for optical coherence tomography imaging of mouse xenograft tumor model in vivo," J Biomed Opt **14**, 054015 (2009).

79. D. J. Faber, E. G. Mik, M. C. G. Aalders, and T. G. van Leeuwen, "Toward assessment of blood oxygen saturation by spectroscopic optical coherence tomography," Opt Lett **30**, 1015-1017 (2005).

80. R. N. Graf, F. E. Robles, X. X. Chen, and A. Wax, "Detecting precancerous lesions in the hamster cheek pouch using spectroscopic white-light optical coherence tomography to assess nuclear morphology via spectral oscillations," J Biomed Opt **14**(2009).

81. A. L. Oldenburg, M. N. Hansen, T. S. Ralston, A. Wei, and S. A. Boppart, "Imaging gold nanorods in excised human breast carcinoma by spectroscopic optical coherence tomography," J Mater Chem **19**, 6407-6411 (2009).

82. A. L. Oldenburg, V. Crecea, S. A. Rinne, and S. A. Boppart, "Phase-resolved magnetomotive OCT for imaging nanomolar concentrations of magnetic nanoparticles in tissues," Opt Express **16**, 11525-11539 (2008).

83. A. S. Paranjape, R. Kuranov, S. Baranov, L. L. Ma, J. W. Villard, T. Wang, K. V. Sokolov, M. D. Feldman, K. P. Johnston, and T. E. Milner, "Depth resolved photothermal OCT detection of macrophages in tissue using nanorose," Biomed Opt Express **1**, 2-16 (2010).

84. Y. Jung, R. Reif, Y. Zeng, and R. K. Wang, "Three-dimensional high-resolution imaging of gold nanorods uptake in sentinel lymph nodes," Nano Lett **11**, 2938-2943 (2011).

85. R. V. Kuranov, S. Kazmi, A. B. McElroy, J. W. Kiel, A. K. Dunn, T. E. Milner, and T. Q. Duong, "In vivo depth-resolved oxygen saturation by Dual-Wavelength Photothermal (DWP) OCT," Opt Express **19**, 23831-23844 (2011).

86. R. V. Kuranov, J. Qiu, A. B. McElroy, A. Estrada, A. Salvaggio, J. Kiel, A. K. Dunn, T. Q. Duong, and T. E. Milner, "Depth-resolved blood oxygen saturation measurement by dual-wavelength photothermal (DWP) optical coherence tomography," Biomed Opt Express **2**, 491-504 (2011).

87. G. Y. Guan, R. Reif, Z. H. Huang, and R. K. K. Wang, "Depth profiling of photothermal compound concentrations using phase sensitive optical coherence tomography," J Biomed Opt **16**(2011).

88. H. M. Subhash, H. Xie, J. W. Smith, and O. J. McCarty, "Optical detection of indocyanine green encapsulated biocompatible poly (lactic-co-glycolic) acid nanoparticles with photothermal optical coherence tomography," Opt Lett **37**, 981-983 (2012).

89. J. M. Tucker-Schwartz, T. Hong, D. C. Colvin, Y. Xu, and M. C. Skala, "Dual-modality photothermal optical coherence tomography and magnetic-resonance imaging of carbon nanotubes," Opt Lett **37**, 872-874 (2012).

90. J. M. Tucker-Schwartz, T. A. Meyer, C. A. Patil, C. L. Duvall, and M. C. Skala, "In vivo photothermal optical coherence tomography of gold nanorod contrast agents," Biomedical optics express **3**, 2881-2895 (2012).

91. C. Loo, A. Lowery, N. Halas, J. West, and R. Drezek, "Immunotargeted nanoshells for integrated cancer imaging and therapy," Nano Lett **5**, 709-711 (2005).

92. L. Tong, Q. Wei, A. Wei, and J. X. Cheng, "Gold nanorods as contrast agents for biological imaging: optical properties, surface conjugation and photothermal effects," Photochem Photobiol **85**, 21-32 (2009).

93. J. Chen, F. Saeki, B. J. Wiley, H. Cang, M. J. Cobb, Z. Y. Li, L. Au, H. Zhang, M. B. Kimmey, X. Li, and Y. Xia, "Gold nanocages: bioconjugation and their potential use as optical imaging contrast agents," Nano Lett **5**, 473-477 (2005).

94. S. Barbosa, A. Agrawal, L. Rodriguez-Lorenzo, I. Pastoriza-Santos, R. A. Alvarez-Puebla, A. Kornowski, H. Weller, and L. M. Liz-Marzan, "Tuning size and sensing properties in colloidal gold nanostars," Langmuir **26**, 14943-14950 (2010).

95. J. M. Tucker-Schwartz, T. A. Meyer, C. A. Patil, C. L. Duvall, and M. C. Skala, "In vivo photothermal optical coherence tomography of gold nanorod contrast agents," Biomed Opt Express **3**, 2881-2895 (2012).

96. D. Boyer, P. Tamarat, A. Maali, B. Lounis, and M. Orrit, "Photothermal imaging of nanometer-sized metal particles among scatterers," Science **297**, 1160-1163 (2002).

97. L. Cognet, C. Tardin, D. Boyer, D. Choquet, P. Tamarat, and B. Lounis, "Single metallic nanoparticle imaging for protein detection in cells," Proc Natl Acad Sci U S A **100**, 11350-11355 (2003).

98. J. Kim, J. Oh, and T. E. Milner, "Measurement of optical path length change following pulsed laser irradiation using differential phase optical coherence tomography," J Biomed Opt **11**(2006).

CHAPTER 3

Characterize and Optimize PTOCT for In Vivo Imaging Using Gold Nanorods

Tucker-Schwartz JM, Meyer TA, Patil CA, Duvall CL, Skala MC, "*In vivo* photothermal optical coherence tomography of gold nanorod contrast agents," *Biomedical Optics Express,* 2012; 3(11):2881-2895.

3.1 Abstract

Photothermal optical coherence tomography (PTOCT) is a potentially powerful tool for molecular imaging. Here, we characterize PTOCT imaging of gold nanorod (AuNR) contrast agents in phantoms, and we apply these techniques for *in vivo* AuNR imaging. The PTOCT signal was compared to the bio-heat equation in phantoms, and *in vivo* PTOCT images were acquired from subcutaneous 400 pM AuNR matrigel injections into mice. Experiments revealed that PTOCT signals varied as predicted by the bio-heat equation, with significant PTOCT signal increases at 7.5 pM AuNR compared to a scattering control ($p<0.01$) while imaging in common path configuration. *In vivo* PTOCT images demonstrated an appreciable increase in signal in the presence of AuNRs compared to controls. Additionally, *in vivo* PTOCT AuNR signals were spatially distinct from blood vessels imaged with Doppler OCT. We anticipate that the demonstrated *in vivo* PTOCT sensitivity to AuNR contrast agents is sufficient to image molecular expression *in vivo*. Therefore, this work demonstrates the translation of PTOCT to *in vivo* imaging and represents the next step towards its use as an *in vivo* molecular imaging tool.

3.2 Introduction

In vivo molecular imaging is widely used in pre-clinical studies of the diseases that cause the greatest burdens of morbidity and mortality in the developed world (e.g. cancer, cardiovascular disease, diabetes, etc.) [1]. When performed at high resolution, *in vivo* molecular imaging can provide insight into the mechanisms of disease progression and drug resistance on a cellular level, thereby unraveling heterogeneities in pathological expression and drug response that are critical

for understanding and combatting these diseases [2]. Microscopy, including confocal and multiphoton microscopy, has been the standard for high resolution molecular imaging in live cells and tissues. However, these microscopy techniques suffer from relatively shallow imaging depths. Magnetic resonance imaging (MRI) and positron emission tomography (PET) have been the standard for functional imaging deep within the body, but these methods lack cellular-level resolution.

Optical coherence tomography (OCT) fills a niche between high resolution microscopy and whole body imaging techniques with cellular-level resolution and penetration depths in tissue that exceed the imaging depths of microscopy. This three-dimensional, non-invasive imaging technique provides an especially attractive scale for monitoring mouse models of disease. However, contrast in standard OCT images is based largely on differences in scattering cross section, which can be minimal amongst certain molecular species. Thus, augmenting standard OCT images with sensitive and specific molecular contrast represents an area of significant interest.

Functional extensions of OCT, including magneto-motive (MMOCT) [3, 4], spectroscopic [5-7], pump-probe [8, 9], and photothermal OCT (PTOCT), have demonstrated molecular contrast. Specifically, PTOCT has recently received much attention [10-19] for a number of reasons. First, PTOCT is able to identify and separate absorbing targets from the scattering background through active detection of photothermal heating [20] (which is also independent of tissue mechanical properties, unlike MMOCT). Second, PTOCT is highly sensitive to absorbing targets in the sample due to active detection and low background. Finally, PTOCT can exploit the rapid recent advancements in nanotechnology to develop efficient, molecularly-targeted contrast agents. For example, gold nanoparticles with near infrared (NIR) plasmon resonance peaks have been investigated for imaging and photothermal therapy [21-24] and are particularly attractive contrast

agents for PTOCT.

PTOCT leverages the photothermal heating phenomenon, where photon absorption by an imaging target of interest (e.g. an absorbing nanoparticle) leads to a temperature change in the environment surrounding the target [25]. These local temperature changes cause thermoelastic expansion of the sample and shifts in the local index of refraction [26]. The photothermal-induced shifts in the local index of refraction and geometric path length alter the local optical path length (OPL, the product of index of refraction and geometric path length). OPL changes due to photothermal heating can be directly imaged via the phase information in an OCT interferogram. The PTOCT signal has been shown to increase with increasing pump beam power and absorber concentration, and the PTOCT signal to noise ratio increases with the number of repeated photothermal cycles [10, 11].

PTOCT has previously been characterized and demonstrated *in vitro* and *ex vivo* with targeted gold nanospheres [10], non-targeted gold nanoshells [11, 12], gold nanorods [14], gold nanorose [13], and carbon nanotubes [18]. However, to date, no contrast agents have been imaged with PTOCT *in vivo*. Two studies have demonstrated *in vivo* PTOCT of hemoglobin (for quantifying blood oxygenation) [15, 16], although only point scans (not images) were collected over multiple second long acquisition times. The primary goal of this study is to demonstrate the ability of PTOCT to image contrast agents *in vivo*.

Gold nanorods (AuNRs) are especially appealing contrast agents for *in vivo* PTOCT because of their resonance in the NIR tissue optical window (~650-900 nm), tunable optical absorption properties (based on their physical dimensions) [27], and efficient absorption (compared to gold nanoshells and nanospheres) [28]. AuNRs are also on a more advantageous size scale for *in vivo* molecular imaging (tens of nanometers in size) compared to nanoshells (hundreds of nanometers in size). Finally, the full width half max (FWHM) of the AuNR absorption peak is much smaller

than that of nanoshells [29, 30], which is desirable to avoid attenuation of the imaging beam by the contrast agent.

The idealized pairing of PTOCT with AuNR contrast agents could allow for three-dimensional *in vivo* molecular imaging in a currently unexploited regime of resolution and penetration depth. However, prior to *in vivo* molecular imaging, the PTOCT signal must be characterized, optimized, and tested in simpler *in vivo* systems without the added complexity of targeted molecular imaging. In this paper, AuNRs are demonstrated as robust PTOCT contrast agents, achieving pM-scale concentration sensitivity. The PTOCT signal is also characterized with respect to imaging speed, photothermal beam power, and OCT magnitude signal. In addition, experimental PTOCT signals are directly compared to photothermal heating models. Finally, we demonstrate PTOCT imaging of AuNRs in phantoms as well as the first documented *in vivo* images of contrast agents using PTOCT.

3.3 Methods

3.3.1 AuNR Synthesis

AuNRs were synthesized using a common seed-mediated growth method employing the surfactant hexadecyltrimethyl ammonium bromide (CTAB) [31]. Briefly, a gold nanoparticle seed solution was prepared by adding 600µl of 10mM ice cold sodium borohydride to a 10ml 250µM gold chloride solution in 100mM CTAB, under vigorous stirring. The growth solution was prepared by adding 800µl of 10mM silver nitrate and 550 µl of 100mM to 100 ml of a 500µM gold chloride solution in 100mM CTAB. Following complete reduction of the gold ions (change in color from yellow to clear), 120 µl of the seed solution was added, and the AuNRs were left undisturbed overnight. Synthesized AuNRs were purified by two rounds of centrifugation at 10,000xg for 20 minutes, followed by re-suspension in fresh deionized (DI) water. CTAB surface molecules were then exchanged for 5000 dalton polyethylene glycol (PEG) chains to improve biocompatibility,

stability in salt solutions and serum, and extend circulation times [28, 32]. Briefly, 10μl of 1mM mPEG-SH and 100 μl of 2mM potassium carbonate were added to 1 ml of 4nM CTAB-coated AuNRs and stirred overnight. PEG-AuNRs were then purified by two rounds of centrifugation/resuspension. The peak absorption wavelength of the AuNRs was approximately 725 nm both before and after PEG exchange (Fig. 3.1(a)), with minor blue shifts (<10 nm) in peak wavelength a month after fabrication (data not shown). The average size of the AuNRs was determined to be 45.2±5.7 nm long by 13.2±1.8 nm wide (n=20) by transmission electron microscopy (TEM), shown in Fig. 3.1(b) and 1(c). The presence of the PEG coating on the surface of the AuNRs was confirmed by a small increase in hydrodynamic diameter measured with dynamic light scattering (DLS) using a Zetasizer Nano ZS (Malvern Instruments, Ltd.) (Fig. 3.1(d)). The stability of the PEG coating was confirmed by unaltered spectrophotometry spectra after suspension in 10X PBS, a high salt solution, and 15% FBS, both of which cause aggregation (and spectral shifts) in CTAB coated AuNRs. The AuNR concentration was calculated using spectrophotometry curves [33].

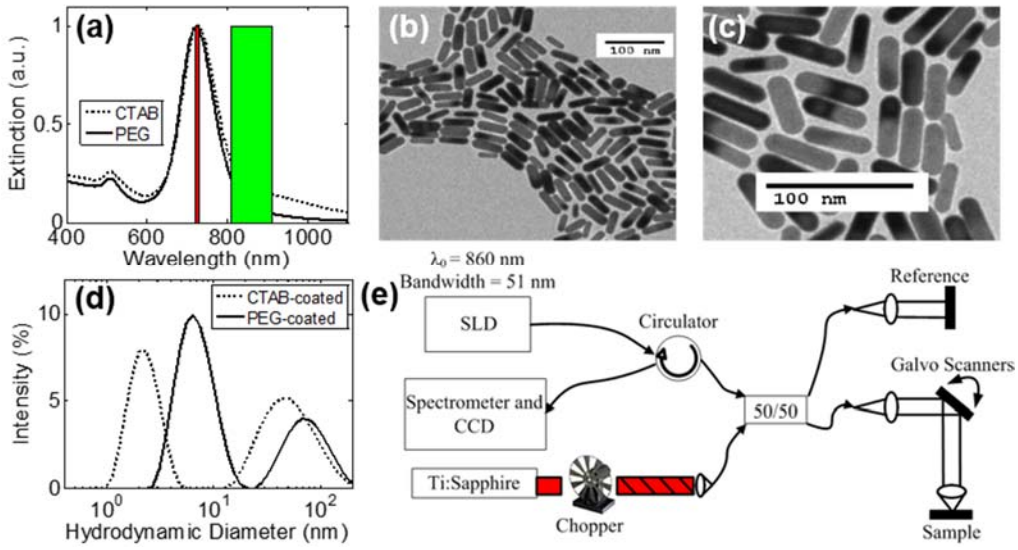

Fig. 3.1. AuNR characterization and imaging instrumentation. (a) Spectrophotometry curves of AuNRs before (dashed) and after (solid) PEG coating, showing peak extinction at 725 nm. (b-c) TEM images of AuNR sample at two scales. AuNR size was 45.2±5.7 nm long by 13.2±1.8 nm (n=20). (d) DLS curve before (dashed) and after (solid) addition of PEG coating, showing rightwards shift and increase in overall size. (e) PTOCT imaging instrumentation. SLD: super luminescent diode; CCD: charge coupled device; 50/50: 50/50 fiber splitter.

3.3.2 Imaging Instrumentation

A commercial spectral domain OCT system (Bioptigen, Inc.) was altered for photothermal imaging (Fig. 3.1(e)). The OCT system contains an 860 nm center wavelength 51 nm FWHM super luminescent diode (SLD) with 6.4 μm axial resolution in air, and 900 μW of power on the sample (95.6 dB signal to noise ratio at 176 μm in depth). The SLD light is fiber coupled and split between a reference mirror and sample arm using a 50/50 fiber coupler while X-Y galvos in the sample arm perform lateral scanning. Returning interference light is sent through an 860 nm center wavelength circulator to a spectrometer with a 2048 pixel CCD. A-line integration time for all experiments was 100 μs (10 kHz line sampling rate). A femtosecond pulse (<140 fs), 80 MHz repetition rate, Titanium:Sapphire laser (Coherent, Inc.) tuned to 725 nm serves as a quasi-CW photothermal laser source, which is fiber coupled with the OCT system via the 50/50 fiber coupler. A standard continuous wave laser can be used in its place, and the PTOCT signal dynamics over the temporal

and spatial scales used here remain unchanged between the two laser options (data not shown). For all experiments with the exception of the *in vivo* studies, a higher resolution lens (16.5 μm $1/e^2$ spot at the focus for the OCT imaging beam) was used to focus both the OCT and photothermal light onto the sample, with 10 mW average photothermal laser power on the sample. For *in vivo* experiments, a lower resolution lens (40 μm $1/e^2$ spot at the focus for the OCT imaging beam) was used for an increased depth of focus and less divergent photothermal beam. The increased spot size of the low resolution lens was accounted for by increasing the average photothermal power on the sample to 40 mW, maintaining similar irradiance for all experiments. Prior to fiber-coupling, the pump beam is attenuated with a half wave plate and polarizer, while a mechanical chopper (Newport, Inc.) modulates the amplitude of the free space beam at a predetermined frequency (200 Hz 50% duty cycle square wave unless otherwise noted). For each A-scan, 1000 repeated axial depth scans (M-mode scans) are performed at the same lateral point while the pump beam is amplitude modulated.

3.3.3 Signal Processing

Temporal oscillations in phase have been previously quantified using OCT [34]. Following resampling to wavenumber, dispersion correction [35], and DC reference spectrum and fixed pattern noise removal [36], the OCT interference spectrum (I) as a function of wavenumber (k), and depth (z), at a given scan time (t_0), can be described by

$$I(k,t_0) = 2\left|E_R E_S\right|\cos(2kz+\varphi) \qquad (3.1)$$

where E_R is the electric field from the reference arm, E_S is the electric field from the sample, and φ is a random phase noise term. The magnitude and phase information as a function of depth at time t_0 is calculated using a Chirp Z Transform (CZT) along the dimension of k [12]. The CZT operation allows for control over the frequency resolution as well as the locations of magnitude and phase analysis in image space [37].

$$I(z,t_0) = CZT[I(k,t_0)]\big|_k = \left|M(z,t_0)\right|\exp[i\Phi(z,t_0)] \tag{3.2}$$

In Eq. 3.2, $|M(z,t_0)|$ is the magnitude spectrum, and $\Phi(z,t_0)$ is the phase spectrum as a function of depth at time t_0. Using the photothermal laser and mechanical chopper, cyclical amplitude modulations in OPL are achieved over time in the M-mode scan. Eq. 3.2 is repeated for all temporal lines in the M-mode scan to create a 2-D magnitude ($|M(z,t_0)|$, Fig. 3.2(a)) and phase spectrum ($\Phi(z,t_0)$, Fig. 3.2(b)). Photothermal oscillations approximated as a sinusoid at the chopping frequency f_0 can be extracted from the phase signal of the OCT image over time at a specific depth, z_0 (Fig. 3.2(c)).

$$\Phi(z_0,t) = \frac{4\pi}{\lambda}A(z_0)\sin(2\pi f_0 t) + \varphi \tag{3.3}$$

In Eq. 3.3, λ is the center wavelength of the imaging beam (860 nm) and $A(z_0)$ is the magnitude of the induced OPL changes due to photothermal heating at depth z_0. In order to remove the random phase term (φ), center the signal around zero, and avoid phase wrapping, the derivative of the phase signal is computed similar to Doppler OCT algorithms [34, 38],

$$\Delta\Phi(z_0,t) = \frac{8\pi^2}{\lambda}A(z_0)f_0\cos(2\pi f_0 t)\Delta t + \xi(t) = \tan^{-1}\left\{\frac{\mathrm{Im}[I(z_0,t)I^*(z_0,t-1)]}{\mathrm{Re}[I(z_0,t)I^*(z_0,t-1)]}\right\} \tag{3.4}$$

where Δt is the sampling period (100 μs) and $\xi(t)$ is a phase noise term due to the photon, thermal, and electronic noise of the system [34]. A subsequent Fourier transform in the temporal direction allows for the magnitude of OPL changes at the laser amplitude modulation frequency (f_0 = 200 Hz) to be calculated with high SNR (Fig. 3.2(d)).

$$FT[\Delta\Phi(z_0,t)]\big|_t = \left|p(z_0,f)\right|\exp[i\theta(z_0,f)] = \frac{8\pi^2}{\lambda}A(z_0)f_0\Delta t\{\frac{1}{2}[\delta(f-f_0)+\delta(f+f_0)]\} \tag{3.5}$$

This operation is repeated at all depths to find the photothermal-induced optical path length changes as a function of depth (z).

$$OPL(z) = A(z) = \frac{|p(z, f_0)|\lambda}{4\pi^2 f_0 \Delta t} \tag{3.6}$$

In Eq. 3.5 and 3.6, *FT* is the Fourier transform operation in the temporal dimension, $|p(z,f)|$ is the magnitude of the Fourier transform of the temporal phase signal at line z as a function of temporal frequency (f), $\theta(z,f)$ is the phase spectrum of the same signal, and δ is a delta function. As shown by Eq. 3.6, the PTOCT signal ($OPL(z)$) is calculated from the magnitude of the Fourier transform of the processed phase data at the chopping frequency ($|p(z,f_0)|$). The 1000 repeated temporal scans were then separated to 20 overlapping 512 point scans, and Fourier transforms over these shorter temporal windows were averaged. Frequency averaging over small, overlapping windows within a discretely sampled signal allows for less variability in the estimate of the true spectrum, and more accurate estimation of signal and noise [39, 40]. The final PTOCT signal included the subtraction of photothermal noise, defined as the mean magnitude of nearby frequencies (270-370 Hz) in the FT of the phase signal (Eq. 3.5). This noise subtraction accounted for the baseline spectral intensity of the FT. The final PTOCT signal was filtered in the axial direction using a trimmed inner mean filter to reduce noise, thresholded using the intensity image to remove noise dominated PTOCT pixels, and median filtered with a 4 pixel square kernel to reduce speckle noise. PTOCT images were processed offline after image acquisition using a custom Matlab script.

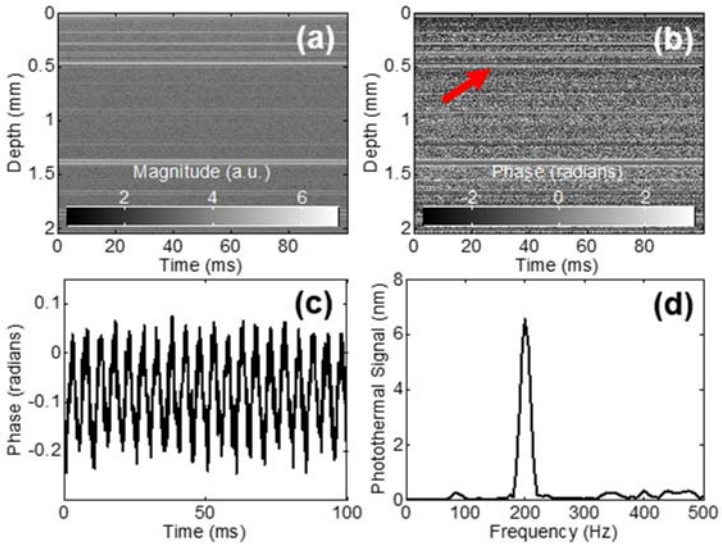

Fig. 3.2. PTOCT signal processing basics. (a) M-mode OCT magnitude scan as a function of time and depth. (b) Accompanying M-mode OCT phase scan as a function of depth and time. (c) Representative temporal phase information at one point in depth (red arrow in 1b), showing amplitude modulated fluctuations of phase due to photothermal heating. (d) Fourier transform of temporal phase data, showing distinct peak at the photothermal modulation frequency (200Hz) in units of nm displacement in OPL. Data taken in common path configuration.

3.3.4 Modeling the Photothermal Signal

To understand the effects of parameter changes on the PTOCT signal, experiments were performed on AuNR samples in 1X PBS and compared to previously tested theoretical models of photothermal heating dynamics [11, 41]. The photothermal-induced temperature dynamics (and thus the PTOCT signal) in space and time due to the absorption of the photothermal beam can be modeled using the bio-heat conduction equation with a heat source term,

$$\frac{\partial T}{\partial t} = \frac{\phi \mu_a}{\rho c} + \alpha \nabla^2 T \qquad (3.7)$$

where T is temperature, t is time in seconds, ρ is the density of the medium (1000 kg/m^3 for water), c is the specific heat of the medium (4186 J/kg K for water), φ is the photothermal laser fluence rate at the sample, μ_a is the absorption coefficient of the AuNR sample (~1200 m^{-1} for a homogenous 800 pM nanorod sample), and α is the thermal diffusivity of the medium, defined as $\alpha=k/\rho c$, where k is thermal conductivity of the medium (0.6 W/ K for water). For small spot sizes relative to the

absorption depth, the heat conduction equation is dominated by radial heat transfer, and can be represented by a closed form solution in cylindrical coordinates. Over one modulation period of the chopper ($2t_L$), the change in temperature at the heat source over time can be modeled according to previous work [11, 41].

$$\Delta T(t, r=0) = \frac{P\mu_a}{4\alpha\pi\rho c}\ln\left(1+\frac{t\alpha}{\omega^2/8}\right), \omega \ll \frac{1}{\mu_a}, t < t_L \tag{3.8}$$

$$\Delta T(t-t_L, r=0) = \frac{P\mu_a}{4\alpha\pi\rho c}\ln\left(1+\frac{t_L\alpha}{\omega^2/8+\alpha(t-t_L)}\right), \omega \ll \frac{1}{\mu_a}, t \geq t_L \tag{3.9}$$

In Eq. 3.8 and 3.9, P is photothermal laser power, ω is the $1/e^2$ beam radius of the photothermal beam, and t_L is the dwell time of the laser on the sample before mechanical interference from the chopper transitions photothermal power to zero. Note that this model is applied to a continuous wave (CW) heating beam that is amplitude-modulated by the optical chopper at the frequency of interest. Although we use a femtosecond laser in our experiments, as stated above, we assume its behavior as quasi-CW due to the high repetition rate (80 MHz) among other considerations. The photothermal heating dynamics of the femtosecond source have been experimentally validated to be equivalent to a CW source over the spatial and temporal scales of these experiments (data not shown). Solutions over time for the model in Eq. 3.8 and 3.9 were compiled with a custom Matlab file.

3.3.5 Parameter Characterization and PTOCT Sensitivity

It is important to note that, although this model has been used to understand the photothermal phenomena as imaged with PTOCT [11], here we directly compared it's outputs to PTOCT signals during parameter perturbations. To do so, PTOCT signal from a AuNR solution was assessed with respect to pump beam laser power, chopping frequency, and OCT magnitude signal. To assess the effect of these parameters on the PTOCT signal, and to confirm that experimental PTOCT data mimics the physical photothermal heating model (Section 2.4), the following experiments were

conducted. PTOCT imaging was performed on the AuNR sample while altering the parameter of interest, leaving all remaining instrumentation and sample properties unchanged (n=10). A 5 µl 800 pM concentration sample of AuNRs in 1X PBS was placed on a microscope slide. The PTOCT signal at the bottom of the sample (~150 µm) was assessed. For chopping frequency and irradiance experiments, the sample was covered with a coverslip, positioned with the coverslip at the focal point of the OCT beam, and the reference arm was fully attenuated. The top coverslip reflection thus served as the reference reflection (i.e. common path imaging), in order to increase phase stability (common path imaging phase stability = 2.1 mrad, reference arm imaging phase stability = 119.9 mrad). Phase stability was measured as the standard deviation of the derivative phase signal (Eq. 3.4) at the bottom of a coverslip over 1000 repeated A-scans. The rate at which the photothermal beam was amplitude modulated [the chopping frequency f_0, where $f_0 = 1/(2t_L)$] was tested at a number of frequencies from 50 Hz to 700 Hz. The same sample was then imaged with varying levels of photothermal laser power from 3.5 mW to 15 mW peak power on the sample. The effect of OCT magnitude signal on the PTOCT signal was also determined. For OCT magnitude signal experiments, the reference arm was incorporated and repeatedly attenuated to alter the reflectivity of the OCT magnitude image between experiments. OCT magnitude signal was calculated as 20 times the common logarithm of the peak reflectivity signal in the image divided by the standard deviation of the background signal. OCT magnitude signal over a 25 dB range was tested.

Linearity and sensitivity of the PTOCT system to AuNR contrasts was determined by imaging varying concentrations of AuNRs using the imaging methods above with common path imaging geometry. Sensitivity was determined as the smallest concentration sample with a significantly different signal from a control scattering phantom (1% intralipid sample). Linearity was determined using least squares regression and statistical significance was assessed with unpaired t-tests

($p<0.01$).

3.3.6 Phantom Imaging

Phantoms were created to assess spatial specificity of the PTOCT signal. A 4% low gelling temperature agarose solution was prepared with 1X PBS. Agarose was heated above 85 degrees Celsius to dissolve it into solution. AuNRs were then added to the heated agarose to create a 2% agarose, 400 pM AuNR experimental sample. A control phantom was also made by diluting down the 4% agarose to 2% with 1X PBS. Samples were mixed well with a pipette, and then loaded into a capillary tube via capillary action to allow for solidification for 10 minutes at room temperature. After solidification, capillary tubes were imaged with the PTOCT system, incorporating the reference arm. Cross sectional images of one control and experimental capillary tube were each imaged at 5 different locations, and an approximately 1 mm by 0.75 mm square region of interest (ROI) within the capillary tube was chosen for each image for further analysis. The mean and standard deviation across OCT magnitude and PTOCT ROIs were compared between agarose/AuNR- (control) and agarose/AuNR+ (experimental) capillary tube images.

3.3.7 *In Vivo* Imaging

PTOCT imaging of contrast agents *in vivo* was performed in a nude mouse using a protocol approved by the Vanderbilt University IACUC. While the mice were maintained under 2% isoflurane anesthesia, matrigel was directly injected into the subcutaneous tissue of the left ear, and a 400 pM AuNR matrigel solution was injected into the right ear. The surface of the tissue was rinsed with PBS to remove any contrast agent that leaked onto the skin, and imaging was performed under isoflurane anesthesia 20 minutes after matrigel injections. OCT, Doppler OCT, and PTOCT scans were performed on each mouse ear to compare the measured PTOCT signal with and without AuNRs *in vivo*. Doppler OCT was assessed using the same repeated scans as the PTOCT data (Doppler number = 999), and processed using the mean derivative phase signal over the repeated

Doppler scans [38].

3.4 Results

3.4.1 Photothermal Model and Parameter Results

As shown in Fig. 3.3(a), experimental PTOCT data (solid line, taken from an 800 pM solution of AuNRs) over one chopping period (f_0 = 200 Hz) along with the local heating and cooling dynamics predicted by the photothermal model in Eq. 3.8 and 3.9 (dashed line) are in agreement. Over one chopping period, the temperature at the photon absorption point increases logarithmically when the photothermal pump beam is on. Once the photothermal pump beam is blocked, the temperature at the photon absorption point decreases logarithmically.

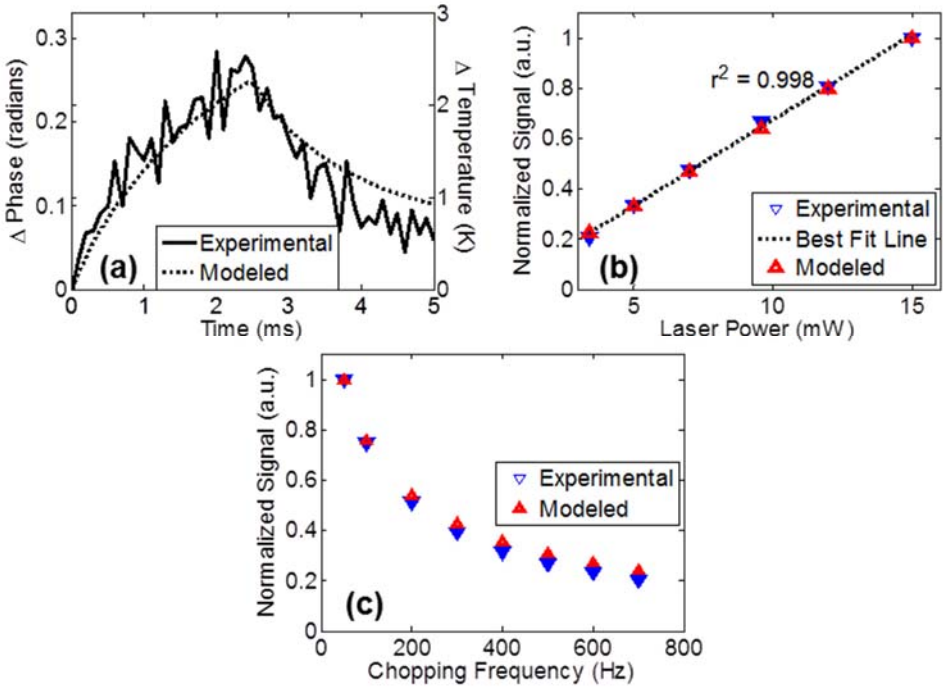

Fig. 3.3. Comparison of experimental PTOCT and theoretical photothermal heating signals. (a) Temporal plot of one photothermal heating cycle at f_0 = 200 Hz. The model (dashed, change in degrees K) predicts temperature dynamics similar to the experimentally measured (solid, change in radians) phase changes of an 800 pM AuNR sample imaged with PTOCT. (b) The photothermal pump laser power and the PTOCT signal are linearly related in both the model and experiments. (c) An increase in the chopping frequency of the photothermal pump laser causes a logarithmic decrease in the PTOCT signal in both the model and experiments. All experimental data collected in common-path mode. Experimental data in b,c plotted as signal ± s.d.

Changes in the PTOCT signal as a function of pump beam laser power and chopping frequency (f_0) also agree with theory (Fig. 3.3(b)-(c)). The modeled photothermal signal is defined as the peak temperature increase observed over one heating cycle, as shown in Eq. 3.10 below. The peak PTOCT signal occurs at $t=t_L$, the point at which the irradiance goes from maximum to zero due to the chopper's mechanical interference. At that point in time, the maximum photothermal modeled signal is given by:

$$\Delta T(t = t_L, r = 0) = \Delta T_{\max} = \frac{P\mu_a}{4\alpha\pi\rho c}\ln\left(1 + \frac{t_L\alpha}{\omega^2/8}\right) \tag{3.10}$$

For the purposes of comparison, the experimental PTOCT signal and modeled photothermal signal (Eq. 3.10) are normalized to the signal observed at either the highest laser power in the plot (15 mW, Fig. 3.3(b)), or the minimum chopping frequency in the plot (50 Hz, Fig. 3.3(c)). As predicted in Eq. 3.8 and 3.9, both the experimental PTOCT and modeled photothermal signal linearly increase ($r^2 = 0.998$) with photothermal pump laser power (P, Eq. 3.10) on the sample (Fig. 3.3(b)). However, increasing the chopping frequency causes a more complex change in the PTOCT signal. The chopping frequency (f_0) is directly related to the chopping period ($2t_L$) by $f_0 = 1/(2t_L)$. Therefore, the effect of the chopping frequency on the maximum photothermal temperature increase in one chopping period can be calculated from Eq. 3.10 and the relationship between t_L and f_0.

$$\Delta T_{\max} = \frac{P\mu_a}{4\alpha\pi\rho c}\ln\left(1 + \frac{\alpha/(2f_0)}{\omega^2/8}\right) \tag{3.11}$$

Eq. 3.11 shows that the maximum photothermal temperature change logarithmically decays with increased chopping frequency (f_0), which is evident in both the modeled and experimental results (Fig. 3.3(c)). Therefore, faster chopping frequencies degrades PTOCT signals. However, faster chopping frequencies are desirable for practical *in vivo* studies, because they allow for faster image acquisition speeds (note that the PTOCT SNR increases by capturing a greater number of

photothermal cycles per A-scan [11], which can be more quickly captured with a faster chop frequency). Consequently, the practical choice of chopping frequency is a trade-off between irradiance on the sample, imaging speed, and PTOCT SNR.

The OCT magnitude signal should not affect the PTOCT signal, since the OCT magnitude signal (the intensity of the OCT image) does not affect the thermodynamics which control photothermal heating (Eq. 3.8 and 3.9). Experimental results confirm that altering the OCT magnitude signal does not have an effect on the mean PTOCT signal (Fig. 3.4(a)). Conversely, decreasing the OCT magnitude signal does increase the noise in the PTOCT signal (Fig. 3.4(b)), which accounts for the increased variance in the PTOCT signal as OCT magnitude signal decreases (error bars, Fig. 3.4(a)). The increase in PTOCT noise due to decreased OCT magnitude signal is predicted by the power-law relationship between OCT phase stability and OCT SNR [42].

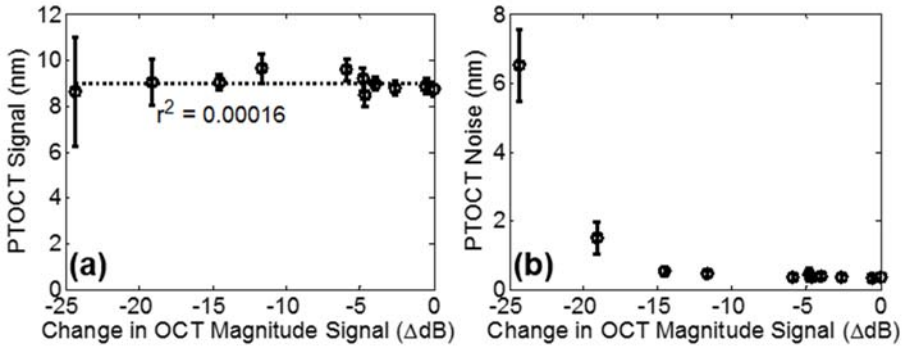

Fig. 3.4. The effect of OCT reflectivity on the photothermal signal. (a) Decreases in the OCT reflectivity cause no change in the mean PTOCT signal, as demonstrated by the low correlation coefficient and horizontal linear fit. (b) Decreasing the OCT reflectivity increases the noise in the PTOCT signal, due to decreased phase stability of low SNR image points as previously predicted [39,41]. All experimental data collected with a reference arm. Values are plotted as signal ± s.d.

3.4.2 Linearity and Sensitivity of the Photothermal Signal

According to the theoretical model in Eq. 3.8 and 3.9, increasing the concentration of the absorber (AuNRs) in the sample (and thus the absorption coefficient) linearly increases the photothermal signal. Accordingly, the PTOCT signal linearly increases with AuNR concentration

($r^2 = 0.997$, Fig. 3.5).

Notably, Fig. 3.5 demonstrates that the magnitude of the heating increase as measured by PTOCT scales linearly with the concentration of contrast agent, even though the heating process itself is dynamic and nonlinear (Fig. 3.3(a)). The PTOCT system described above (common-path mode) exhibits 7.5 pM (~ 0.54 mg/L) sensitivity to AuNRs when compared to a scattering control (1% intralipid, red in Fig. 3.5, $p<0.01$).

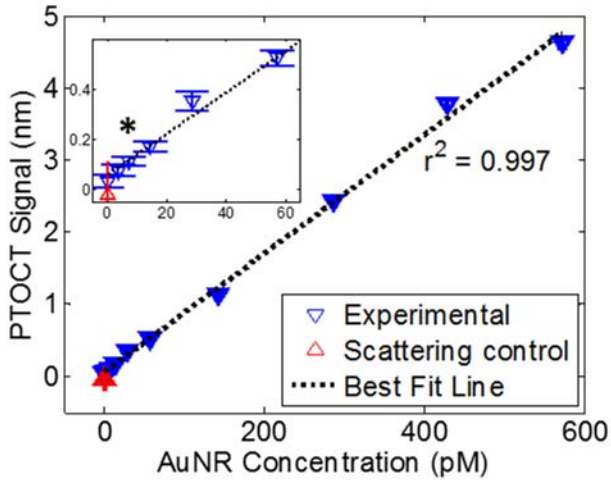

Fig. 3.5. PTOCT signal is linearly related to the concentration of AuNR. A AuNR sample with a concentration as low as 7.5 pM has a significantly higher ($p<0.01$) PTOCT signal than a scattering control (1% intralipid, red). Values are plotted as signal ± s.d. Data collected in common path configuration.

3.4.3 Phantom Imaging

Capillary tube imaging was performed using the reference arm in order to demonstrate the ability of PTOCT to spatially distinguish the presence of AuNRs at concentrations anticipated to be achievable *in vivo* and in an imaging environment with reduced phase stability. AuNR positive and negative capillary tubes display similar OCT magnitude signals, but significantly different PTOCT signals (Fig. 3.6). The OCT magnitude images measured from n=5 capillary tube images are similar between AuNR positive and negative regions (AuNR positive region = 4.07±0.003 a.u., AuNR negative region = 4.02±0.004 a.u.), while the AuNR positive capillary tube exhibits a 15 fold

enhanced PTOCT signal with respect to the agarose control (AuNR positive region = 3.81 ± 0.24 nm, AuNR negative region = 0.24 ± 0.05 nm). Small phase accumulations cause an apparent increase in PTOCT signal in the AuNR+ tube as depth increases.

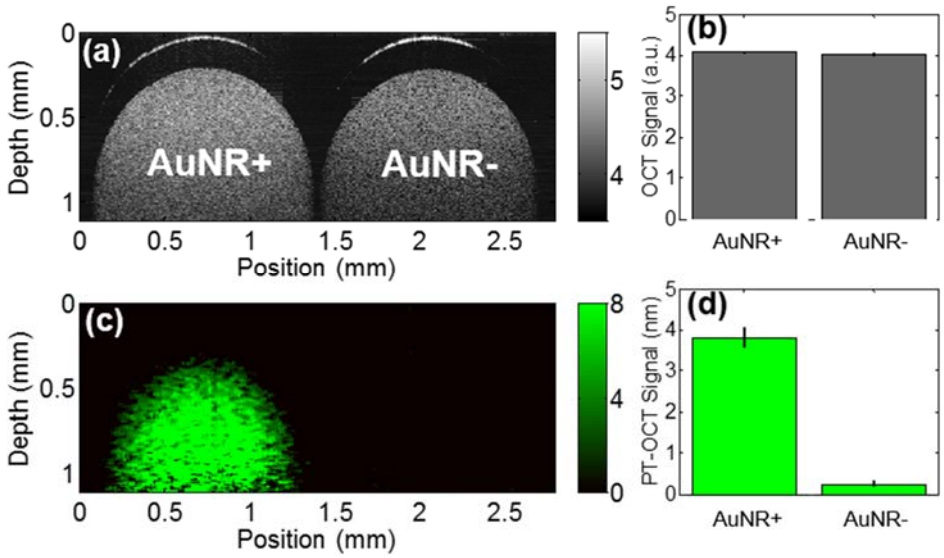

Fig. 3.6. PTOCT images of capillary tube phantoms. (a) Example OCT magnitude images of AuNR+ (left) and AuNR- (right) solid agarose capillary tube phantoms. (b) Mean ± standard deviation OCT signal from a series of n=5 capillary tube images. (c) Example PTOCT images of capillary tubes from 5a, displaying the ability of PTOCT to distinguish AuNR+ from AuNR- sample. (d) Mean ± standard deviation of PTOCT signal from a series of n=5 capillary tube images. Data collected with a reference arm in tact.

3.4.4 *In Vivo* PTOCT Imaging

Representative PTOCT images in the experimental and control ears of a mouse are shown in Fig. 3.7. Doppler OCT overlays in Fig. 3.7 (red and blue channels) illustrate the presence of small blood vessels crossing the B-scan. There is a dramatic increase in PTOCT signal in the experimental ear where AuNRs are present compared to control ears with matrigel only. Signal increases occur in discrete locations spatially separate from the vessels, indicating that there is PTOCT signal not due to blood absorption. The PTOCT signal gains in the AuNR+ mouse ear are similar to that from *ex vivo* AuNR injections into chicken breast using the same 400pM AuNR injection (data not shown). Additional B-scan images (not shown) demonstrate the same representative increases in

PTOCT signal in AuNR+ mouse ears compared to control injections.

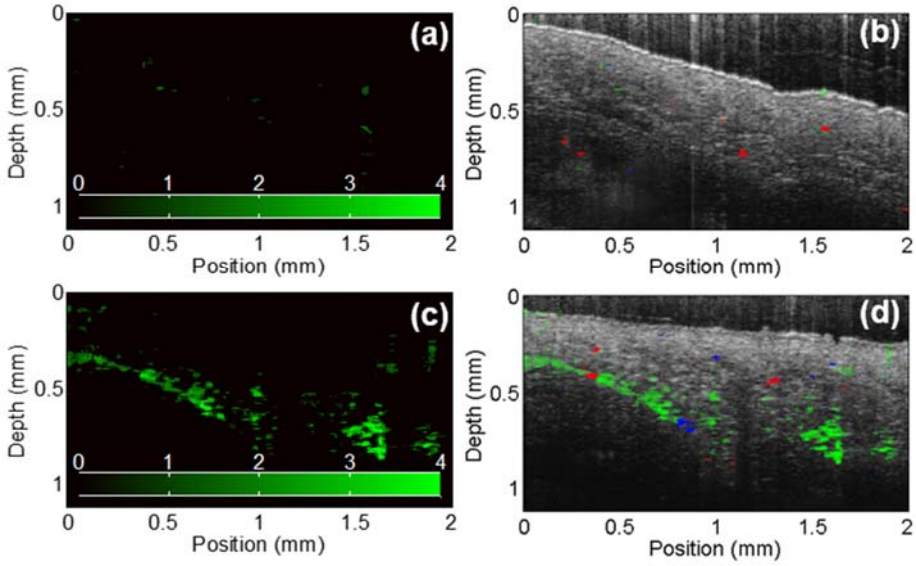

Fig. 3.7. *In vivo* PTOCT of AuNRs. (a) PTOCT signal in the control mouse ear injected with only matrigel. (b) The OCT image (grayscale channel) of the control ear, with Doppler (red and blue channels) and PTOCT (green channel) overlaid. (c) PTOCT signal in the experimental mouse ear injected with 400 pM AuNR in matrigel. (d) OCT image (grayscale channel) of experimental ear with Doppler (red and blue channels) and PTOCT (green channel) overlaid. Data collected with the reference arm in tact.

3.5 Discussion

We have demonstrated PTOCT of highly absorbing AuNR contrast agents in the near infrared wavelength region, including validation in phantoms and feasibility studies *in vivo*. We characterized the photothermal signal with the bio-heat equation, and directly compared modeled and experimental PTOCT data. The PTOCT system in common path configuration demonstrated high (pM-level) sensitivity to AuNR contrast agents (Fig. 3.5), with detection levels appropriate for *in vivo* imaging of AuNR uptake in mouse tumors [43]. The linear relationship between contrast agent concentration and PTOCT signal leaves open the possibility of quantitative molecular imaging with PTOCT. In addition, AuNR contrast agents were successfully imaged *in vivo*, demonstrating a first step towards *in vivo* molecular imaging with PTOCT.

Before pursuing imaging applications involving complex *in vivo* systems with PTOCT, it is

important to thoroughly characterize and optimize the imaging system in more controlled environments. Therefore, we performed experiments to assess the photothermal signal as a function of chopping frequency, laser power (and thus irradiance), and OCT magnitude signal. These experimental PTOCT results were compared to the results of a quantitative photothermal heating model. The physical basis of the PTOCT signal is a change in OPL. Since the transition from temperature change to OPL is essentially linear, but difficult to accurately solve [11], the modeled (maximum temperature change, Eq. 3.10) and experimental (maximum OPL change, Eq. 3.6) results were compared after normalization (Fig. 3.3). From Eq. 3.8 and 3.9, it is evident that the only controllable imaging parameters governing the photothermal temperature change are the chopping frequency (i.e. how rapidly the photothermal laser is amplitude modulated) and the laser irradiance (a function of spot size and laser power). Therefore, we tested the effects of these two variables on the photothermal signal, in comparison to the predictions of a well-established closed form solution for the heat conduction equation [11, 41]. Our results indicate that the heat conduction model accurately represents experimental PTOCT data. As expected, an increase in irradiance linearly increases the PTOCT signal (Fig. 3.3(b)), while increased chopping frequency logarithmically degrades the PTOCT signal (Fig. 3.3(c)).

The photothermal heating of a sample (Eq. 3.8 and 3.9) is not dependent upon a traditional OCT image, only on the sample and heating parameters. Therefore, the PTOCT peak signal should be independent of the OCT magnitude signal. It is essential to demonstrate independence between OCT magnitude signal and PTOCT signals because of the speckle and heterogeneities in OCT magnitude images. As predicted, the OCT magnitude signal did not affect the mean PTOCT signal (Fig. 3.4(a)). However, the OCT magnitude signal did impact the noise in the PTOCT signal (Fig. 3.4(b)), in agreement with the predicted power-law degradation of phase stability with decreased OCT SNR [42, 44].

This work demonstrates the first reported *in vivo* imaging of contrast agents with PTOCT and is an important step towards the use of PTOCT in molecular imaging studies in mice. However, there are some remaining considerations to address before robustly applying PTOCT toward *in vivo* molecular imaging. First, motion artifacts must be limited during PTOCT imaging. Motion artifact can be minimized by physically restraining the tissue, and by gating images between breathing cycles. In addition, the derivative operation in Eq. 3.4 and subsequent Fourier transform (Eq. 3.5) help to separate oscillations due to motion artifact from the OPL oscillations that form the PTOCT signal. The results shown here indicate the effects of motion artifacts can be minimized if the PTOCT chopping frequency does not overlap with frequencies due to motion artifacts. Common path imaging using a secured coverslip above the sample or by surface coating with a diffuse scattering compound [45] could also assist with motion artifact compensation. Algorithms and image registration methods for removing motion artifacts in OCT phase and magnitude signals also currently exist to help reduce the affects from sample motion [46-48]. Second, the divergence and scattering of the photothermal beam through tissue complicates calculations of irradiance as a function of depth. Phantom measurements of the photothermal beam size as a function of depth along with Monte Carlo simulations could address this problem, or ratiometric measurements could be acquired at different pump beam wavelengths [49]. Another obstacle to account for is integration of the photothermal signal with depth. Since phase images measure changes in OPL, and OPL is an integrated signal, photothermal signals accumulate in depth, as is evident in Fig. 3.6(c). Previous work has accounted for this integration by taking the local slope of the photothermal signal [17]. However, using local linear curve, highly concentrated samples cannot be accurately characterized with linear models. Finally, the imaging speed for photothermal optical coherence microscopy (OCM) has recently been improved with the use of optical lock-in methods [50]. It is expected that these methods can also be applied to PTOCT to improve imaging speeds, reduce motion artifacts,

and further translate these methods toward *in vivo* use. Regardless of these confounding factors, PTOCT has been proven to be a sensitive method to image both endogenous and exogenous absorptive targets at depths greater than any microscopy method, making it a molecular imaging tool with great potential in biomedical science applications. It is expected that further development of this relatively new technology will overcome these remaining obstacles.

In conclusion, PTOCT is a promising technology, with the potential to enable molecular imaging with an impressive combination of spatial resolution and imaging depth. We have characterized and translated this technology to *in vivo* use, illustrating the potential of PTOCT to address critical needs in pre-clinical molecular imaging. We have demonstrated that PTOCT can image a contrast agent at physiologically relevant concentrations [43] at depths approaching 1mm *in vivo*, exceeding the imaging depths of traditional microscopy (including two-photon) techniques. An additional strength of this method is that it provides images of the spatial distribution of contrast agent along with the complementary existing features of OCT (structural imaging and Doppler OCT of blood flow).

3.6 Acknowledgements

The authors would like to acknowledge the assistance of the following colleagues who contributed to this study: Wesley Sit assisted in animal handling and imaging, Devin McCormack assisted in imaging studies and system characterization, Dr. John Stone consulted on AuNR synthesis and PEG coating, and Dr. Dana Brantley-Sanders performed *in vivo* matrigel injections. This study was supported in part by NIH/NCI R00CA142888.

3.7 References

1. World Health Organization., *Global status report on noncommunicable diseases 2010* (World Health Organization, Geneva, Switzerland, 2011), pp. ix, 162 p.

2. A. Marusyk, V. Almendro, and K. Polyak, "Intra-tumour heterogeneity: a looking glass for cancer?," Nat Rev Cancer **12**, 323-334 (2012).

3. R. John, R. Rezaeipoor, S. G. Adie, E. J. Chaney, A. L. Oldenburg, M. Marjanovic, J. P. Haldar, B. P. Sutton, and S. A. Boppart, "In vivo magnetomotive optical molecular imaging using targeted magnetic nanoprobes," Proc Natl Acad Sci U S A **107**, 8085-8090 (2010).

4. A. L. Oldenburg, V. Crecea, S. A. Rinne, and S. A. Boppart, "Phase-resolved magnetomotive OCT for imaging nanomolar concentrations of magnetic nanoparticles in tissues," Opt Express **16**, 11525-11539 (2008).

5. D. J. Faber, E. G. Mik, M. C. G. Aalders, and T. G. van Leeuwen, "Toward assessment of blood oxygen saturation by spectroscopic optical coherence tomography," Opt Lett **30**, 1015-1017 (2005).

6. R. N. Graf, F. E. Robles, X. X. Chen, and A. Wax, "Detecting precancerous lesions in the hamster cheek pouch using spectroscopic white-light optical coherence tomography to assess nuclear morphology via spectral oscillations," J Biomed Opt **14**(2009).

7. A. L. Oldenburg, M. N. Hansen, T. S. Ralston, A. Wei, and S. A. Boppart, "Imaging gold nanorods in excised human breast carcinoma by spectroscopic optical coherence tomography," J Mater Chem **19**, 6407-6411 (2009).

8. K. D. Rao, M. A. Choma, S. Yazdanfar, A. M. Rollins, and J. A. Izatt, "Molecular contrast in optical coherence tomography by use of a pump-probe technique," Opt Lett **28**, 340-342 (2003).

9. D. Jacob, R. L. Shelton, and B. E. Applegate, "Fourier domain pump-probe optical coherence tomography imaging of Melanin," Opt Express **18**, 12399-12410 (2010).

10. M. C. Skala, M. J. Crow, A. Wax, and J. A. Izatt, "Photothermal optical coherence tomography of epidermal growth factor receptor in live cells using immunotargeted gold nanospheres," Nano Lett **8**, 3461-3467 (2008).

11. D. C. Adler, S. W. Huang, R. Huber, and J. G. Fujimoto, "Photothermal detection of gold nanoparticles using phase-sensitive optical coherence tomography," Opt Express **16**, 4376-4393 (2008).

12. C. Zhou, T. H. Tsai, D. C. Adler, H. C. Lee, D. W. Cohen, A. Mondelblatt, Y. Wang, J. L. Connolly, and J. G. Fujimoto, "Photothermal optical coherence tomography in ex vivo human breast tissues using gold nanoshells," Opt Lett **35**, 700-702 (2010).

13. A. S. Paranjape, R. Kuranov, S. Baranov, L. L. Ma, J. W. Villard, T. Wang, K. V. Sokolov, M. D. Feldman, K. P. Johnston, and T. E. Milner, "Depth resolved photothermal OCT detection of macrophages in tissue using nanorose," Biomed Opt Express **1**, 2-16 (2010).

14. Y. Jung, R. Reif, Y. Zeng, and R. K. Wang, "Three-dimensional high-resolution imaging of gold nanorods uptake in sentinel lymph nodes," Nano Lett **11**, 2938-2943 (2011).

15. R. V. Kuranov, S. Kazmi, A. B. McElroy, J. W. Kiel, A. K. Dunn, T. E. Milner, and T. Q. Duong, "In vivo depth-resolved oxygen saturation by Dual-Wavelength Photothermal

(DWP) OCT," Opt Express **19**, 23831-23844 (2011).

16. R. V. Kuranov, J. Qiu, A. B. McElroy, A. Estrada, A. Salvaggio, J. Kiel, A. K. Dunn, T. Q. Duong, and T. E. Milner, "Depth-resolved blood oxygen saturation measurement by dual-wavelength photothermal (DWP) optical coherence tomography," Biomed Opt Express **2**, 491-504 (2011).

17. G. Y. Guan, R. Reif, Z. H. Huang, and R. K. K. Wang, "Depth profiling of photothermal compound concentrations using phase sensitive optical coherence tomography," J Biomed Opt **16**(2011).

18. J. M. Tucker-Schwartz, T. Hong, D. C. Colvin, Y. Xu, and M. C. Skala, "Dual-modality photothermal optical coherence tomography and magnetic-resonance imaging of carbon nanotubes," Opt Lett **37**, 872-874 (2012).

19. H. M. Subhash, H. Xie, J. W. Smith, and O. J. McCarty, "Optical detection of indocyanine green encapsulated biocompatible poly (lactic-co-glycolic) acid nanoparticles with photothermal optical coherence tomography," Opt Lett **37**, 981-983 (2012).

20. D. Boyer, P. Tamarat, A. Maali, B. Lounis, and M. Orrit, "Photothermal imaging of nanometer-sized metal particles among scatterers," Science **297**, 1160-1163 (2002).

21. J. Chen, F. Saeki, B. J. Wiley, H. Cang, M. J. Cobb, Z. Y. Li, L. Au, H. Zhang, M. B. Kimmey, X. Li, and Y. Xia, "Gold nanocages: bioconjugation and their potential use as optical imaging contrast agents," Nano Lett **5**, 473-477 (2005).

22. C. Loo, A. Lowery, N. Halas, J. West, and R. Drezek, "Immunotargeted nanoshells for integrated cancer imaging and therapy," Nano Lett **5**, 709-711 (2005).

23. L. Tong, Q. Wei, A. Wei, and J. X. Cheng, "Gold nanorods as contrast agents for biological imaging: optical properties, surface conjugation and photothermal effects," Photochem Photobiol **85**, 21-32 (2009).

24. S. Barbosa, A. Agrawal, L. Rodriguez-Lorenzo, I. Pastoriza-Santos, R. A. Alvarez-Puebla, A. Kornowski, H. Weller, and L. M. Liz-Marzan, "Tuning size and sensing properties in colloidal gold nanostars," Langmuir **26**, 14943-14950 (2010).

25. D. Boyer, P. Tamarat, A. Maali, B. Lounis, and M. Orrit, "Photothermal imaging of nanometer-sized metal particles among scatterers," Science **297**, 1160-1163 (2002).

26. J. Kim, J. Oh, and T. E. Milner, "Measurement of optical path length change following pulsed laser irradiation using differential phase optical coherence tomography," J Biomed Opt **11**(2006).

27. X. H. Huang, S. Neretina, and M. A. El-Sayed, "Gold Nanorods: From Synthesis and Properties to Biological and Biomedical Applications," Adv Mater **21**, 4880-4910 (2009).

28. G. von Maltzahn, J. H. Park, A. Agrawal, N. K. Bandaru, S. K. Das, M. J. Sailor, and S. N.

Bhatia, "Computationally guided photothermal tumor therapy using long-circulating gold nanorod antennas," Cancer Res **69**, 3892-3900 (2009).

29. J. R. Cole, N. A. Mirin, M. W. Knight, G. P. Goodrich, and N. J. Halas, "Photothermal Efficiencies of Nanoshells and Nanorods for Clinical Therapeutic Applications," J Phys Chem C **113**, 12090-12094 (2009).

30. P. K. Jain, K. S. Lee, I. H. El-Sayed, and M. A. El-Sayed, "Calculated absorption and scattering properties of gold nanoparticles of different size, shape, and composition: applications in biological imaging and biomedicine," J Phys Chem B **110**, 7238-7248 (2006).

31. C. J. Murphy, T. K. San, A. M. Gole, C. J. Orendorff, J. X. Gao, L. Gou, S. E. Hunyadi, and T. Li, "Anisotropic metal nanoparticles: Synthesis, assembly, and optical applications," Journal of Physical Chemistry B **109**, 13857-13870 (2005).

32. H. W. Liao and J. H. Hafner, "Gold nanorod bioconjugates," Chem Mater **17**, 4636-4641 (2005).

33. C. J. Orendorff and C. J. Murphy, "Quantitation of metal content in the silver-assisted growth of gold nanorods," Journal of Physical Chemistry B **110**, 3990-3994 (2006).

34. R. K. Wang and A. L. Nuttall, "Phase-sensitive optical coherence tomography imaging of the tissue motion within the organ of Corti at a subnanometer scale: a preliminary study," J Biomed Opt **15**(2010).

35. M. Wojtkowski, V. J. Srinivasan, T. H. Ko, J. G. Fujimoto, A. Kowalczyk, and J. S. Duker, "Ultrahigh-resolution, high-speed, Fourier domain optical coherence tomography and methods for dispersion compensation," Optics express **12**, 2404-2422 (2004).

36. S. Moon, S. W. Lee, and Z. P. Chen, "Reference spectrum extraction and fixed-pattern noise removal in optical coherence tomography," Optics express **18**, 24395-24404 (2010).

37. L. R. Rabiner, R. W. Schafer, and C. M. Rader, "Chirp Z-Transform Algorithm," Ieee T Acoust Speech **Au17**, 86-& (1969).

38. R. K. Wang and L. An, "Doppler optical micro-angiography for volumetric imaging of vascular perfusion in vivo," Opt Express **17**, 8926-8940 (2009).

39. P. D. Welch, "Use of Fast Fourier Transform for Estimation of Power Spectra - a Method Based on Time Averaging over Short Modified Periodograms," Ieee T Acoust Speech **Au15**, 70-& (1967).

40. A. V. Oppenheim, R. W. Schafer, and J. R. Buck, *Discrete-time signal processing,* 2nd ed. (Prentice Hall, Upper Saddle River, N.J., 1999), pp. xxvi, 870 p.

41. M. J. C. vanGemert, G. W. Lucassen, and A. J. Welch, "Time constants in thermal laser medicine .2. Distributions of time constants and thermal relaxation of tissue," Phys Med

Biol **41**, 1381-1399 (1996).

42. M. A. Choma, A. K. Ellerbee, C. H. Yang, T. L. Creazzo, and J. A. Izatt, "Spectral-domain phase microscopy," Opt Lett **30**, 1162-1164 (2005).

43. A. Agrawal, S. Huang, A. Wei Haw Lin, M. H. Lee, J. K. Barton, R. A. Drezek, and T. J. Pfefer, "Quantitative evaluation of optical coherence tomography signal enhancement with gold nanoshells," J Biomed Opt **11**, 041121 (2006).

44. B. J. Vakoc, S. H. Yun, J. F. de Boer, G. J. Tearney, and B. E. Bouma, "Phase-resolved optical frequency domain imaging," Opt Express **13**, 5483-5493 (2005).

45. N. Krstajic, C. T. A. Brown, K. Dholakia, and M. E. Giardini, "Tissue surface as the reference arm in Fourier domain optical coherence tomography," J Biomed Opt **17**(2012).

46. V. X. D. Yang, M. L. Gordon, A. Mok, Y. H. Zhao, Z. P. Chen, R. S. C. Cobbold, B. C. Wilson, and I. A. Vitkin, "Improved phase-resolved optical Doppler tomography using the Kasai velocity estimator and histogram segmentation," Opt Commun **208**, 209-214 (2002).

47. S. Makita, Y. Hong, M. Yamanari, T. Yatagai, and Y. Yasuno, "Optical coherence angiography," Opt Express **14**, 7821-7840 (2006).

48. D. L. G. Hill, P. G. Batchelor, M. Holden, and D. J. Hawkes, "Medical image registration," Phys Med Biol **46**, R1-R45 (2001).

49. T. Jetzfellner, A. Rosenthal, A. Buehler, K. H. Englmeier, D. Razansky, and V. Ntziachristos, "Multispectral optoacoustic tomography by means of normalized spectral ratio," Opt Lett **36**, 4176-4178 (2011).

50. C. Pache, N. L. Bocchio, A. Bouwens, M. Villiger, C. Berclaz, J. Goulley, M. I. Gibson, C. Santschi, and T. Lasser, "Fast three-dimensional imaging of gold nanoparticles in living cells with photothermal optical lock-in Optical Coherence Microscopy," Opt Express **20**, 21385-21399 (2012).

CHAPTER 4

Image Spatial Heterogeneities of Intra-Tumor Gold Nanoparticle Delivery *In vivo* Using PTOCT

Tucker-Schwartz JM, Beavers KR, Sit WW, Shah AT, Duvall CL, Skala MC, "*In vivo* imaging of nanoparticle delivery and tumor microvasculature with multimodal optical coherence tomography," *Biomedical Optics Express,* 2014; 5(6):1731-1743.

4.1 Abstract

Current imaging techniques capable of tracking nanoparticles *in vivo* supply either a large field of view or cellular resolution, but not both. Here, we demonstrate a multimodality imaging platform of optical coherence tomography (OCT) techniques for high resolution, wide field of view *in vivo* imaging of nanoparticles. This platform includes the first *in vivo* images of nanoparticle pharmacokinetics acquired with photothermal OCT (PTOCT), along with overlaying images of microvascular and tissue morphology. Gold nanorods (51.8 ± 8.1 nm by 15.2 ± 3.3 nm) were intravenously injected into mice, and their accumulation into mammary tumors was non-invasively imaged *in vivo* in three dimensions over 24 hours using PTOCT. Spatial frequency analysis of PTOCT images indicated that gold nanorods reached peak distribution throughout the tumors by 16 hours, and remained well-dispersed up to 24 hours post-injection. In contrast, the overall accumulation of gold nanorods within the tumors peaked around 16 hours post-injection. The accumulation of gold nanorods within the tumors was validated post-mortem with multiphoton microscopy. This shows the utility of PTOCT as part of a powerful multimodality imaging platform for the development of nanomedicines and drug delivery technologies.

4.2 Introduction

Clinical trials are currently underway to test gold nanoparticles as cancer therapeutics [1-3] due to their attractive physical and biological properties [4]. Gold nanoparticles have also enabled significant advances in pre-clinical cancer research as drug delivery vectors [5] and imaging

contrast agents [6]. However, there is a need for improved technologies to image gold nanoparticle distributions *in vivo* in the context of microvessel morphology (the key delivery system for nanoparticles). Such an imaging platform could be used to optimize the size, shape, material composition, and surface chemistry of nanoparticles for improved clinical performance. High resolution, small field of view, and shallow imaging depth microscopy techniques including dark-field and multiphoton are most often used to image gold nanoparticles *in vitro* (and more rarely *in vivo*) [7-9]. For animal studies, postmortem and destructive mass spectrometry techniques [10-12] are often employed to investigate the general bio-distribution of nanoparticles. Emerging *in vivo* imaging modalities that can monitor gold nanoparticle delivery (e.g. computed tomography [2, 13], photoacoustic tomography [6, 14], surface enhanced Raman scattering [15], and microscopy techniques [16]) supply either a large field of view or high resolution, but not both. In addition, the majority of these existing tools cannot supply label-free contrast of the local microvasculature, an essential component for assessing drug delivery. Consequently, there is a significant gap in technologies that can provide non-destructive *in vivo* images of nanoparticle pharmacokinetics with high resolution at depths greater than microscopy. This spatial regime is important because heterogeneities in tumor microenvironment and microvessel morphology, for example, can drastically alter local therapeutic delivery and thus clinical efficacy [17].

We demonstrate photothermal optical coherence tomography (PTOCT), a functional extension of optical coherence tomography (OCT), to fill this spatial niche for *in vivo* imaging of nanoparticle delivery. OCT is a noninvasive, three-dimensional (3D) imaging tool that detects back-scattered near-infrared (NIR) photons from a sample to visualize tissue morphology [18]. OCT fills the spatial imaging niche between high resolution microscopy and whole body imaging techniques, supplying high resolution (1-30 μm) at depths greater than traditional and multiphoton microscopy (1-3 mm) [19]. In addition to tissue morphology, Doppler [20] as well as speckle [21] and phase

[22] variance imaging techniques allow OCT to image microvessel morphology and quantify blood flow without the addition of contrast agents. Although OCT provides images of tissue and microvessel morphology on a spatial scale that is relevant for imaging animal models of disease, the source of OCT contrast (index of refraction mismatches) weakly differs between molecular species. Therefore, functional versions of OCT have been developed to visualize endogenous and exogenous targets [23-28]. PTOCT is an especially sensitive functional extension of OCT that identifies photon absorbing targets with high specificity over background tissue scattering [26-28]. PTOCT has been demonstrated with nanoparticle contrast agents *in vitro* and *ex vivo* including gold nanospheres [26], gold nanoshells [28], gold nanorods [27, 29], carbon nanotubes [30], and gold nanoroses [31], and PTOCT was recently demonstrated for *in vivo* imaging of subcutaneous injections of gold nanorods into a mouse ear [27].

This study demonstrates a novel and powerful application of PTOCT for *in vivo* imaging of nanoparticle delivery to tumors, and provides unique insights into heterogeneities in nanoparticle uptake and microvascular function that can be used to optimize nanoparticle delivery. This work provides the first PTOCT image volumes *in vivo*, as well as the first co-registered images of tissue structure, microvessel morphology, and nanoparticle delivery in the OCT spatial imaging regime. PTOCT non-destructively images nanoparticle uptake in tumors in three dimensions with microscopic resolution and a wide enough field of view to capture a large region of the tumor (multiple millimeter scan range). Therefore, PTOCT can potentially provide a robust method to study the effects of size, shape, material composition, and surface chemistry of gold nanoparticles for improved *in vivo* delivery. Gold nanorods (AuNRs) were studied because they exhibit tunable and narrow NIR local surface plasmon resonance peaks, with photothermal efficiencies greater than gold nanoshells [2]. Here, PTOCT is used to image the accumulation of intravenously-injected AuNRs into mouse mammary tumors via the enhanced permeability and retention (EPR)

effect, a hallmark of cancer where newly formed and leaky vasculature allows extravasation of particles between 5 and 200 nm [32, 33] diameter into the tumor tissue space [17, 34].

4.3 Methods

4.3.1 Gold Nanorod (AuNR) Synthesis

Methoxy-terminated poly(ethylene glycol) (PEG) AuNRs were synthesized for *in vivo* injection using a well-established seed-mediated growth method using the surfactant hexadecyltrimethyl ammonium bromide (CTAB) [35]. Following synthesis, CTAB surface molecules were exchanged with 5 kDa PEG molecules to increase biocompatibility and circulation time *in vivo*. To do so, a 20 mM solution of 5 kDa mPEG-thiol (Layson Bio) in distilled water was reduced with immobilized TCEP resin (Thermo Scientific) for one hour at room temperature. One mL of CTAB-coated AuNRs was functionalized with PEG by the sequential addition of 275 μL of 1.1 mM K2CO3 and 250 μL of reduced 5 kDa mPEG-thiol. PEG-coated AuNRs were then purified by centrifugation at 15,300 x g for 10 minutes and resuspended in 1X PBS. Efficient surface PEGylation was verified by a lack of AuNR aggregation upon resuspension in 15% FBS and 10X PBS. A stock solution of PEG-coated AuNRs with an absorption peak at 740 nm was sterile filtered using 200 nm pore syringe filters and concentrated to 9 nM for *in vivo* injection. A representative transmission electron microscopy (TEM) image and spectrophotometry curve for the AuNRs are shown in Fig. 4.1(a). Quantitative analysis of TEM images revealed an average AuNR size of 51.8 ± 8.1 nm long by 15.2 ± 3.3 nm wide (n=20), and an average aspect ratio of 3.4.

4.3.2 Imaging Instrumentation

A commercial fiber-coupled spectral domain OCT system (Bioptigen) was altered for PTOCT imaging (Fig. 4.1(b)). An 860 nm central wavelength, superluminescent diode (SLD, Fig. 4.1(b)) served as the OCT imaging beam (6.4 μm resolution in air), with 750 μW of power on the sample.

SLD light was sent through a circulator and split between the imaging sample and a reference reflector using a 50/50 fiber coupler. Returning interference light was captured by a 2048 pixel CCD (Atmel) at a rate of 10 kHz. Incident light on the sample was scanned in the second and third spatial dimension using galvanometer mirrors, and focused to a lateral resolution of approximately 25 μm. Polarization states in the reference and sample arm were optimized using fiber-based polarization controllers (PC, Fig. 4.1(b)). A tunable Titanium:Sapphire NIR laser source (Coherent) served as the photothermal heating beam (note that continuous wave lasers are equally effective sources). This source was amplitude modulated with a 50% duty cycle square wave using a mechanical chopper and coupled into the sample arm fiber for co-alignment with the imaging beam. The photothermal beam was amplitude modulated at 500 Hz and tuned to 740 nm (the AuNR local surface plasmon peak wavelength), with 25 mW of average power on the sample over one modulation period.

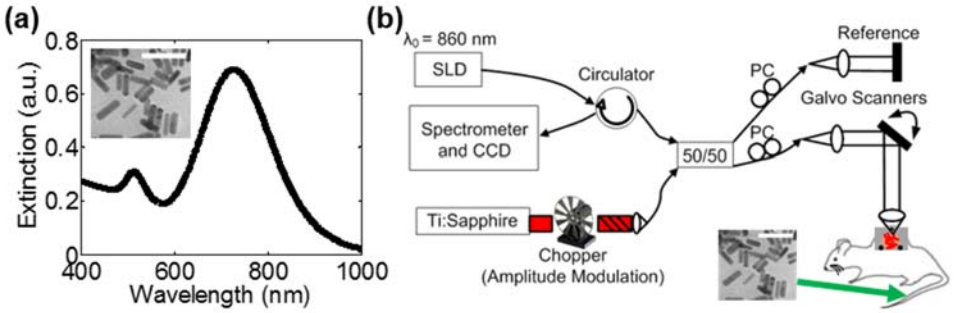

Fig. 4.1. Contrast agents and PTOCT imaging instrumentation. (a) Extinction spectrum of AuNR samples with an absorption peak of approximately 740 nm, with a representative TEM (inset, scale bar = 100 nm). (b) A fiber-based PTOCT system was constructed for imaging. The titanium sapphire laser was amplitude modulated and used as a photothermal heating source. Mice with dorsal skinfold window chambers containing mammary tumors were intravenously injected with AuNRs into the tail vein and imaged with PTOCT over time. SLD: Superluminescent diode; PC: Polarization controllers; 50/50: Fiber coupler

4.3.3 Image Acquisition and Signal Processing

PTOCT exploits the photothermal effect to produce changes in optical path length that can be detected with high sensitivity and specificity using phase-resolved OCT. In our experiments, the

photothermal heat release from AuNRs is modulated with an amplitude-modulated laser tuned to the resonance peak of the nanoparticles (Fig. 4.2(a), top). Upon heat release into the microenvironment, water in the tissue surrounding the nanoparticles undergoes thermoelastic expansion and index of refraction shifts, thus altering the optical path length over time. The phase-resolved OCT image is directly related to optical path length, allowing PTOCT to identify AuNRs within the tissue due to fluctuations in OCT phase (Fig. 4.2(a), bottom) [27].

Digital frequency analysis was used to isolate the photothermal oscillations within the phase-resolved OCT data. For each 1D depth-resolved PTOCT A-scan, 1000 repeated OCT A-scans were captured over time while amplitude modulating the photothermal laser at 500 Hz. Each OCT interferogram was resampled from linearity in wavelength to linearity in wavenumber, dispersion corrected [36], and background subtracted [37]. A Chirp-Z transform converted wavenumber data to depth-resolved image data, creating a three-dimensional complex-number dataset as a function of depth (z), time (t), and lateral position (x) for each B-scan (Fig. 4.2(b)). The phase (Φ, Fig. 4.2(b)) at each point was used for subsequent analysis. The phase in each A-scan was referenced to the first bright reflection to increase phase stability (i.e. self-referencing) [38]. Then, the temporal derivative of the phase at each point in depth was calculated [27], and the data was Fourier transformed in the temporal dimension. The PTOCT signal for each point in depth (z) and lateral position (x) was defined as the magnitude of its temporal Fourier transform at the amplitude modulation frequency of the photothermal beam (500 Hz, green circle Fig. 4.2(b)), minus the background (the mean of the adjacent 200 Hz frequency components). The Fourier transform magnitude data was transformed to optical path length units according to previous methods [27]. This analysis was completed at all points in space to reconstruct PTOCT images (Fig. 4.2(b)). This process was expanded to a third spatial dimension to create 3D volumes. Previous work provides details of the PTOCT system, signal characterization, and signal analysis [27].

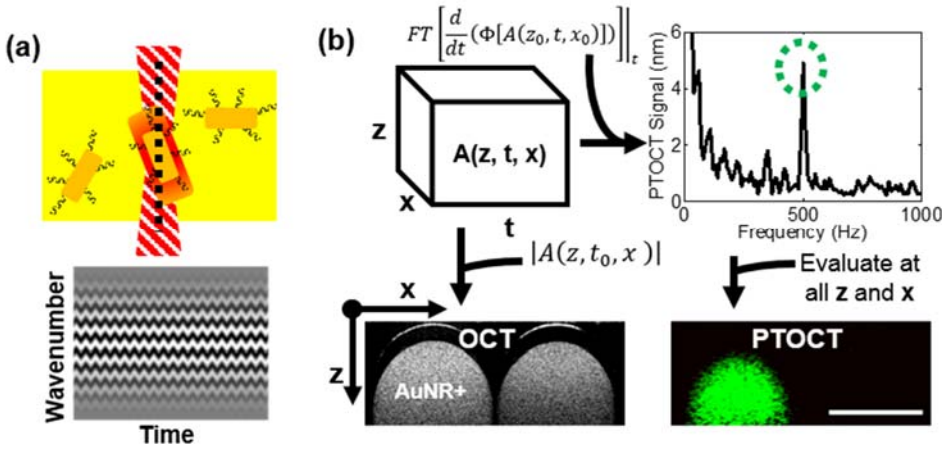

Fig. 4.2. ***In vivo*** **PTOCT signal analysis.** (a) AuNRs (dark yellow, top) in optically scattering tissue (bright yellow, top) are identified by the OCT imaging beam (black dashed line, top) by their photothermal heat release signature after absorption of an amplitude-modulated heating beam (red dashed structure, top). Oscillations in heat release from AuNRs cause oscillations in optical path length and thus the phase of the OCT interference pattern over time (bottom). (b) For each PTOCT B-scan, a complex-valued 3D dataset is constructed as a function of depth (z), space (x), and time (t) (top left). The temporal derivative of the phase (Φ) of this 3D data set is taken, followed by a temporal Fourier transform (top left). A peak in this Fourier-transformed data at 500 Hz (the amplitude-modulation frequency of the photothermal beam, green-dashed circle) reveals the presence of AuNRs (top right). This analysis is repeated at all spatial positions to reconstruct the 2D cross-sectional PTOCT image, which localizes AuNRs (green pixels, bottom right). The magnitude of the depth-resolved dataset provides the traditional OCT structural image (bottom left). Bottom panels show representative OCT and PTOCT images of a solid agarose phantom with AuNRs spatially confined to the left capillary tube (scale bar = 1 mm).

In addition to PTOCT, speckle variance OCT (SVOCT) maps of microvessel morphology (intensity-normalized variance of the magnitude image over 10 repeated A-scans) were collected over the same image volumes, and were then median filtered to reduce noise. Traditional OCT tissue morphology images were calculated as the log based ten values of the magnitude image. Three by two millimeter rectangular volume scans were acquired, with isotropic 10 μm lateral sampling for OCT and SVOCT image volumes, and 10 μm (fast scan dimension) by 100 μm (slow scan dimension) sampling for PTOCT image volumes. PTOCT cross-sectional images were filtered using a two-dimensional (2D) median filter and masked using the OCT magnitude data. The 3D image volumes where then reduced to two *en face* dimensions by averaging along the depth dimension (approximately 1 mm in depth). SVOCT projections were further filtered using a Gabor

filter to increase contrast to vessel-like features [39]. *En face* projections of OCT (tissue morphology, gray), SVOCT (vessel morphology, red), and PTOCT (AuNRs, green) were used for quantitative data analysis. OCT, SVOCT, and PTOCT images were processed and quantified offline using custom Matlab software.

A spatial frequency analysis of the PTOCT *en face* projections was performed to characterize the diffusion of the AuNRs throughout the tissue over time. Each PTOCT *en face* projection was first multiplied by a raised cosine window to remove edge artifacts in the Fourier transform. PTOCT images were then mean subtracted, and a two-dimensional Fourier transform was calculated so that low spatial frequency content of the image was radially centered, with high frequency content located at the edges. Fourier transformed images were then masked to include only low or high frequency components, and the image energy (the sum of the magnitude squared) of the low and high frequency masked images were calculated. This analysis quantifies the percent of image energy that is either low (diffuse) or high (sparse) spatial frequency, and can be expanded to include directionality and multiple frequency bands. The frequency cutoff was selected to enclose spatial frequencies less than or equal to 10% of the Nyquist sampling frequency.

4.3.4 *In Vivo* Imaging

All animal work was approved by the Vanderbilt IACUC committee, and all surgical procedures were performed using aseptic techniques. Six nude ($Foxn1^{nu}$/ $Foxn1^{nu}$, The Jackson Laboratory) female mice, 12 weeks of age, underwent dorsal skinfold window chamber surgery for direct visualization of 4T1 (mouse mammary) tumors. While under inhalant isoflurane anesthesia (1.5-2%), a custom made 10 mm diameter window was placed onto the back of the mouse and secured across a dorsal skinfold with the use of three bolts and sutures at the top and bottom of the window. The skin from one side of the skinfold within the window was removed, as well as the underlying fascia layer. A 4T1 (mouse mammary) solid tumor, which was grown for

16 days in the mammary fat pad of a separate mouse, was sliced to a thin section and placed on the exposed tissue layer in the dorsal window. The window was filled with sterile saline, and overlain with a coverslip to visualize the underlying tumor. 4T1 tumors were allowed to grow in the dorsal skinfold window for 10 days prior to imaging. Following baseline (pre-injection) OCT, SVOCT, and PTOCT imaging, sterile-filtered PEG-coated AuNRs in 1X PBS (200 ml volume, ~9 nM concentration) [2] were injected into the tail vein of four mice, while sterile 1X PBS was injected as a vehicle control into two mice. After injection, three more imaging time points were performed at approximately 2, 16, and 24 hours post-injection to image the accumulation of AuNRs into the tumor tissue via the EPR effect. During imaging, mice body temperature was regulated by a circulating heating pad while the mice were under inhalant isoflurane anesthesia (1.5% in air). Dorsal windows were tightly secured to the imaging stage using a custom apparatus.

4.3.5 *Ex Vivo* Multiphoton Microscopy

Upon completion of *in vivo* imaging time courses, the mice were sacrificed and tumors were harvested for further imaging. The tumor was maintained in standard cell culture media on ice and imaged *ex vivo* using multiphoton luminescence microscopy as an independent validation of AuNR accumulation into the tissue. A custom-built multiphoton epi-fluorescence imaging system (Prairie Technologies) was used for *ex vivo* tissue imaging. A Titanium:Sapphire laser was tuned to the excitation peak of the AuNRs (740 nm) with less than 1 mW of power incident on the sample. An emission filter at 607 nm with a 45 nm bandwidth was used to capture AuNR luminescence signal and reject any autofluorescence. *Ex vivo* images were captured with a 20X objective (NA = 0.75), and were processed offline using a custom Matlab routine. For quantitative analysis, two images for each of the six animals were analyzed (n=12 total). All images were collected in the same imaging session, ensuring constant imaging parameters (laser power, detector settings, etc.) between samples.

4.4 Results

4.4.1 *In Vivo* Imaging of AuNR Accumulation Into Tumors

Mice with mammary tumors in dorsal window chambers were intravenously injected with either AuNRs or 1X PBS (vehicle control), and imaged at multiple time points before and after injection. Examples of the PTOCT image volumes collected with OCT, SVOCT, and PTOCT are shown in Fig. 4.3. Tissue morphology (gray channel, OCT), vessel morphology (red channel, SVOCT), and AuNR distribution (green channel, PTOCT) are inherently co-registered (Fig. 4.3(a)). The distribution of AuNRs at each time point is noninvasively imaged with respect to the tissue structure as well as vessel morphology. An angled slice through the depth dimension yields better visualization of all three image channels as a function of depth (Fig. 4.3(b)). The tissue structure (gray channel, OCT) can also be removed (Fig. 4.3(c)) to better visualize the structure of the AuNR distribution with respect to the vessel morphology. For quantitative comparisons between imaging datasets, image volumes were reduced to two lateral *en face* dimensions via averaging over the depth dimension (Fig. 4.3(d)).

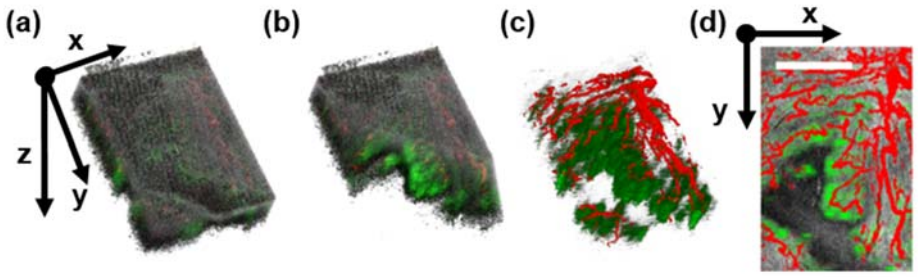

Fig. 4.3. Representative *in vivo* PTOCT image volumes. (a) 3D rendering of mouse 4T1 tumor 16 hours after AuNR injection via the tail vein, with OCT of tissue structure (gray channel), SVOCT of vessel morphology (red channel), and PTOCT of AuNRs (green channel). (b) An angled slice through the 3D volume reveals depth-resolved anatomy, vessel morphology, and AuNR distribution. (c) Removing the structural information reveals the underlying vessels (red) and AuNR distribution (green) in three dimensions. (d) After averaging over the depth dimension, co-registered 2D *en face* projections of tissue morphology, vessel morphology, and AuNR distribution are visible in the tumor tissue (scale bar = 1 mm).

Example *en face* projections of overlapping tissue morphology (gray channel, OCT), vessel morphology (red channel, SVOCT), and AuNR distribution (green channel, PTOCT) for control (1X PBS injected, n=2) and experimental (AuNR injected, n=4) animals are shown in Fig. 4.4. Vessels within the tumor tissue are clearly visible in both control mice injected with 1X PBS (Fig. 4.4, top) as well as experimental mice with systemically injected AuNRs (Fig. 4.4, bottom). In addition, distinct morphological features are present from within the tumor tissue. However, the PTOCT signal is only visible in mice after systemic injection of AuNRs, indicating the ability of PTOCT to specifically image AuNRs *in vivo* at the tumor site, even in the presence of tissue scattering. Due to the size of the AuNRs, the particles are found mainly within close proximity of terminal microvessels over the time points imaged (Fig. 4.4). These findings agree with previous work using histology [40] and microscopy of superficial depths [41] that established a relationship between particle size and diffusion distance from microvessels in tumors. However, these previous studies required destructive techniques or contrast-aided visualization of vasculature.

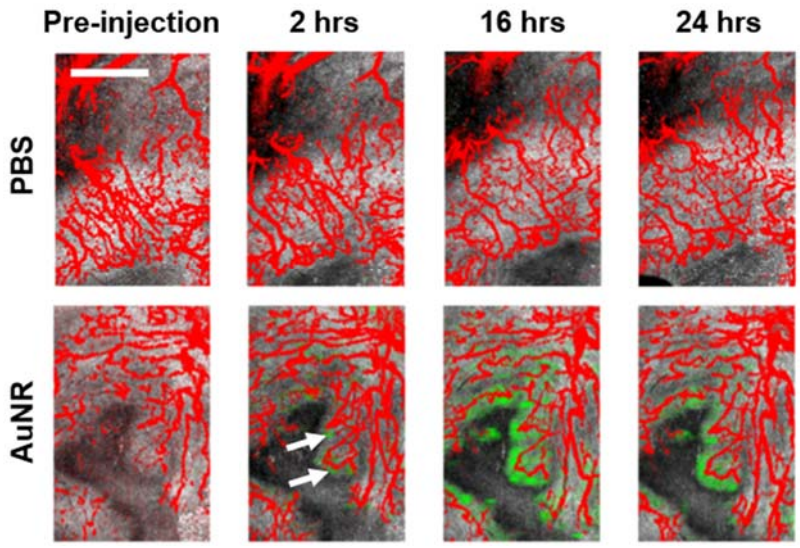

Fig. 4.4. PTOCT signals increase *in vivo* after AuNR injection. *En face* projection images of tissue morphology (OCT, gray), vessel morphology (SVOCT, red), and AuNR distribution (PTOCT, green) in a mouse tumor pre-injection , and 2 hours, 16 hours, and 24 hours after injection of either 1X PBS (top) or AuNRs (bottom) in 1X PBS (scale bar = 1 mm). The PTOCT signal appears only after injection of AuNRs. White arrows point to regions of positive PTOCT signal 2 hours after injection.

Specific imaging of AuNR uptake in tumors is apparent from the *en face* PTOCT projections from mice injected with 1X PBS control (Fig. 4.5(a)) versus AuNRs (Fig. 4.5(b)) 16 hours post-injection. The time-course of AuNR accumulation and retention within the tumors was similar across all animals (Fig. 4.5(c)), and mice injected with AuNRs exhibited significantly increased PTOCT signal compared to pre-injection values ($p<0.05$, Wilcoxon rank sum test, Fig. 4.5(d)). The PTOCT signal peaked at 16 hours after AuNR injections, with a peak PTOCT signal of 145 ± 46 picometers across all experimental animals (Fig. 4.5(d)). Although low resolution imaging modalities can provide information on the bulk accumulation of nanoparticles in tumors, the high resolution and wide field of view of PTOCT allows for visualization of spatially distinct nanoparticle uptake over large regions of the tumor volume. The bulk accumulation of AuNRs in tumors is similar across mice (Fig. 4.5(c)), however there are spatial heterogeneities in uptake within individual tumors and these spatial patterns vary between tumors (Fig. 4.5(b)). One

important attribute of PTOCT is its ability to capture these spatial heterogeneities over a wide field of view, which is difficult to accomplish with microscopy or whole body imaging techniques. Additionally, PTOCT can acquire images at depths greater than confocal and two-photon microscopy.

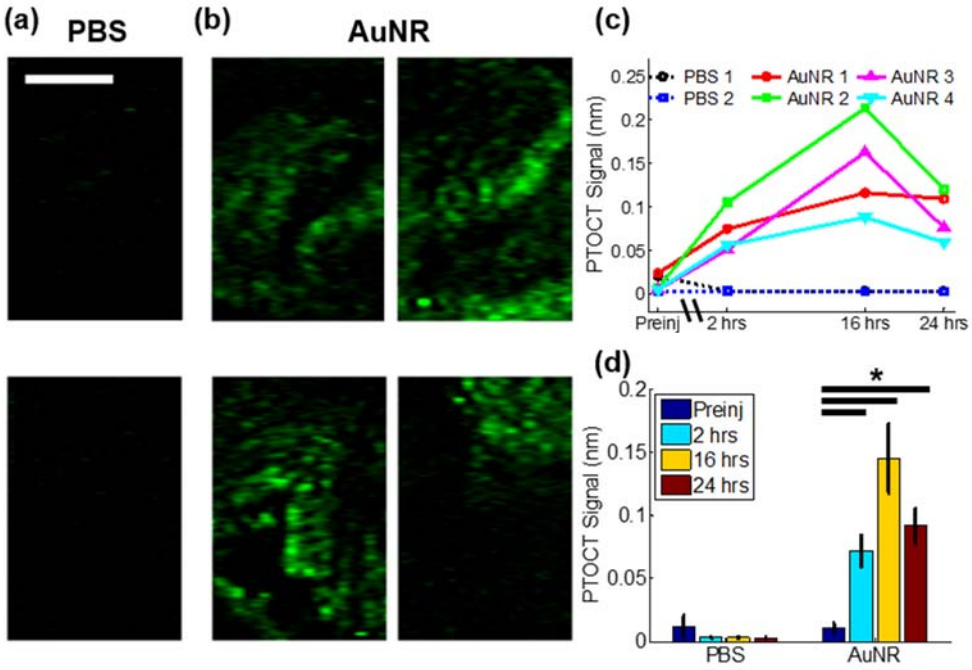

Fig. 4.5. *In vivo* temporal and spatial tracking of AuNR uptake in tumors using PTOCT. *En face* PTOCT projection images from all mice 16 hours after injection of either (a) PBS (n=2) or (b) AuNRs (n=4) (scale bar = 1 mm). (c) Mean PTOCT signal at each imaging time-point for the two mice injected with PBS and the four mice injected with AuNRs ("preinj" = pre-injection). (d) Mean ± standard error PTOCT signal for all mice injected with either PBS (n=2) or AuNRs (n=4). *$p<0.05$.

The high resolution of PTOCT can be exploited for more advanced image analysis to quantify AuNR spatial distribution over time. This analysis can be applied to optimize nanoparticle delivery, and to determine the time-points at which photothermal or other therapeutic interventions would be most effective. Specifically, the sparsity of the AuNR distribution within the tumor at each time point was quantified from the spatial frequency content of each 2D PTOCT projection image. The low and high spatial frequency components correspond to AuNR distributions in the

tumor that are diffuse (more dispersed throughout the tissue) and sparse (spatially confined to distinct locations), respectively.

PTOCT *en face* images for one mouse at the three time points after AuNR injection are shown in Fig. 4.6(a), as well as the accompanying two dimensional Fourier transforms (Fig. 4.6(a), bottom). The red circle in each Fourier transform image (Fig. 4.6(a), bottom) represents the cutoff between low and high frequency content calculations. The image energy due to low frequencies is shown in Fig. 4.6(b) for each mouse injected with AuNRs, and the average for all four mice is plotted in Fig. 4.6(c). Low frequency components are at a minimum at the earliest time point, due to the sparsity of the AuNR accumulation early after injection. At later time points, the low frequency component increases (and the high frequency contribution decreases an equal amount) due to the increased accumulation and diffusion of the AuNRs throughout the tissue ($p<0.05$, Wilcoxon rank sum test). Between the 2 hour and 16 hour time-points, the energy of the low spatial frequencies increases by approximately 15%, then remains fairly constant, indicating that the diffusion of the AuNRs throughout the tissue peaks between those time-points. As shown previously, the mean PTOCT signal (Fig. 4.5(d)) due to AuNR accumulation is similar at 2 and 24 hours. However, the distribution of AuNRs is quite different between those time points (Fig. 4.6(c)). These distribution dynamics are helpful for understanding the pharmacokinetics of AuNRs into and out of the tumor, and for properly optimizing nanoparticles for clinical therapeutic and imaging strategies. Lower resolution imaging tools (computed tomography, photoacoustic tomography, etc.) as well as destructive techniques (e.g. ICPMS) can measure bulk accumulation of AuNRs over a large tumor section. However, the high-resolution distribution analysis provided by PTOCT is critical for understanding AuNR accumulation throughout different spatial locations in the tumor, and highlights the enabling abilities of high resolution, wide field of view, and deeply penetrating PTOCT imaging. For example, nanoparticles that are too large to diffuse away from

nearby vessels can only deliver drug to perivascular tumor regions. PTOCT can resolve these intratumoral heterogeneities in nanoparticle delivery with respect to nearby vasculature, and could therefore serve as a robust tool for tracking the efficacy of nanoparticle-based drug delivery platforms that seek to homogeneously disperse throughout a tumor.

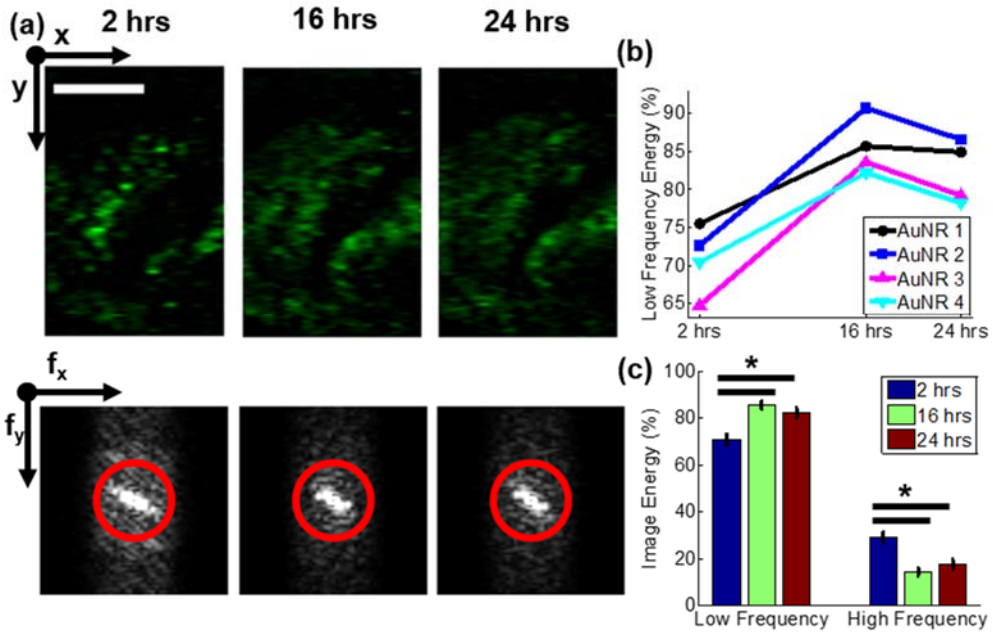

Fig. 4.6. Spatial frequency content analysis of *in vivo* PTOCT images reveals an increase in low spatial frequencies over time. (a) PTOCT *en face* images (top) and accompanying 2D spatial Fourier transforms (bottom) from a representative mouse tumor 2 hours, 16 hours, and 24 hours after injection of AuNRs (scale bar = 1 mm). The red circle highlights the cutoff between high (outside the ring) and low (inside the ring) spatial frequencies. (b) Percent of image energy due to low spatial frequencies over time for four mice injected with AuNRs. (c) Mean ± standard error of the image energy due to low and high spatial frequencies for mice injected with AuNRs (n = 4) over time. *$p < 0.05$.

4.4.2 *Ex Vivo* Validation Using Multiphoton Microscopy

Following the completion of the PTOCT imaging studies, the mice were sacrificed and tumors were harvested for further imaging. Gold nanoparticles possess a strong multiphoton luminescence signal that is spectrally separate from common autofluorescent proteins native to cells, so multiphoton imaging serves as a reliable validation tool for imaging AuNRs [8, 42]. Representative *ex vivo* multiphoton images of tumors from mice intravenously injected with PBS (Fig. 4.7(a)) or

AuNRs (Fig. 4.7(b)) after completion of the PTOCT imaging study are shown, as well as the mean signal for tissues from mice intravenously injected with AuNRs or PBS (Fig. 4.7(c)). All *ex vivo* multiphoton imaging occurred in unaltered tissue samples freshly harvested from the same mice imaged in the PTOCT study. There is a significant increase in the multiphoton signal measured in tumors from mice injected with AuNRs compared to tumors from mice injected with PBS ($p<0.05$, Wilcoxon rank sum test). The average value from the negative control mice indicates the noise floor of the system, since no appreciable structure or signal was visible in any PBS-injected mouse tumor. After *ex vivo* imaging, tumors were formalin fixed, paraffin embedded, sliced, stained with hematoxylin and eosin, and histologically verified as malignant mammary tumors (data not shown). These *ex vivo* analyses confirm the observed increase in PTOCT signal is due to accumulation of AuNRs in the tumor tissue.

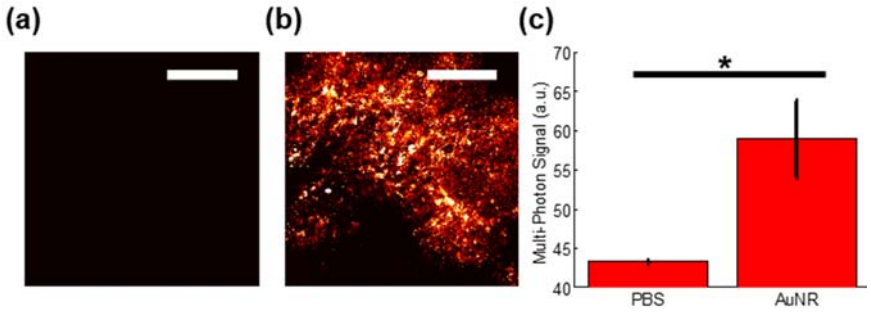

Fig. 4.7. Validation of AuNR uptake into tumor tissue using multiphoton imaging. Representative 20X multiphoton image of tumor tissue 24 hours after tail vein injection of (a) 1X PBS or (b) AuNRs, imaged *ex vivo* (scale bar = 100 μm). (b) Mean ± standard error of the multiphoton signal across all *ex vivo* images from mice injected with either PBS (n=4 images) or AuNRs (n=8 images). *$p < 0.05$

4.5 Discussion

We have shown that PTOCT can temporally track the 3D accumulation of AuNRs into tumor tissue. PTOCT identified peak AuNR accumulation in tumors around 16 hours, which agrees with temporal trends found in previous studies that employed invasive methods to quantify nanoparticle biodistribution [43]. Co-registered images of tissue structure (OCT), vessel morphology (SVOCT),

and nanoparticle distribution (PTOCT) with the same imaging system could allow for comprehensive analyses of nanoparticle delivery kinetics. For example, this platform of multimodal OCT can be applied to analyze *in vivo* drug diffusion distances from vessels over time, or to validate *in vivo* drug release over a greater tumor volume than previous studies, without the need for vascular contrast agents [41, 44]. PTOCT has the potential to track not only gold nanoparticles *in vivo*, but any molecule with a strong NIR absorption cross section (e.g. near infrared fluorophores [45], carbon nanotubes [30]), with large fields of view, at high resolution, and at depths greater than confocal and multiphoton microscopy. This could allow for *in vivo* imaging of the delivery of clinically relevant agents of different size, shape, and surface chemistry in the context of the microvasculature (i.e. the drug delivery system). For example, PTOCT could track dye-tagged drugs or nanoparticles over time and over multiple doses to quantify the *in vivo* spatial distribution and pharmacokinetics of these agents at the target site. PTOCT could also be used to refine delivery strategies to overcome clearance by the immune system [46]. Additionally, other orthotopic tumor models including brain and mammary windows [22] can be imaged with PTOCT, further supporting widespread adoption.

Remaining optimizations including phase accumulation [47] and imaging speed [48] can also be incorporated for more streamlined acquisition and analysis. In its current implementation, PTOCT contains axial image artifacts due to phase accumulation. Published models address this issue in layered homogeneous phantoms [47], and models for heterogeneous *in vivo* images are currently under development. In addition, the current PTOCT implementation uses digital sampling and frequency analysis, which required a 14-minute scan time per volume. However, with the development of optical lock-in techniques for low coherence interferometry [48], PTOCT can potentially be performed with significantly reduced acquisition times. Long *in vivo* scan times can also cause image artifacts due to respiratory and cardiac motion. However, a few key data

acquisition and signal processing considerations were used in this study to minimize the impact of motion artifact on PTOCT images. First, the photothermal heating laser was modulated at 500 Hz, which lies outside of the frequency range of motion artifact (<500 Hz). Second, the phase at all points in depth was digitally referenced to the most shallow reflection in the image (i.e. the dorsal window coverslip), thus improving phase stability [38]. Last, any remaining motion artifact was background subtracted using the average of the frequency components adjacent to the photothermal frequency.

In conclusion, PTOCT is a promising imaging platform for the study of gold nanoparticles and other photon-absorbing molecules *in vivo*. PTOCT provides non-invasive images of 3D drug delivery dynamics, along with corresponding tissue and vessel morphology images. As the technology continues to develop, PTOCT could have broad applications to assess *in vivo* delivery of nanomedicines and imaging contrast agents, greatly impacting drug discovery and molecular imaging.

4.6 Acknowledgments

This work was supported by grants from the National Institutes of Health under award numbers R00CA142888 and R25CA136440-05. In addition, the authors wish to acknowledge Victoria Youngblood and Dr. Jin Chen for assistance with *in vivo* tumor systems, Spencer Crowder for supplying 4T1 tumor cells, and Tianwei Shen and Travis Meyer for assistance in gold nanorod synthesis.

4.7 References

1. J. A. Schwartz, A. M. Shetty, R. E. Price, R. J. Stafford, J. C. Wang, R. K. Uthamanthil, K. Pham, R. J. McNichols, C. L. Coleman, and J. D. Payne, "Feasibility Study of Particle-Assisted Laser Ablation of Brain Tumors in Orthotopic Canine Model," Cancer Res 69, 1659-1667 (2009).

2. G. von Maltzahn, J. H. Park, A. Agrawal, N. K. Bandaru, S. K. Das, M. J. Sailor, and S. N. Bhatia, "Computationally Guided Photothermal Tumor Therapy Using Long-Circulating Gold Nanorod Antennas," Cancer Res 69, 3892-3900 (2009).

3. A. M. Gobin, M. H. Lee, N. J. Halas, W. D. James, R. A. Drezek, and J. L. West, "Near-infrared resonant nanoshells for combined optical imaging and photothermal cancer therapy," Nano Lett 7, 1929-1934 (2007).

4. A. S. Thakor, J. Jokerst, C. Zavaleta, T. F. Massoud, and S. S. Gambhir, "Gold Nanoparticles: A Revival in Precious Metal Administration to Patients," Nano Lett 11, 4029-4036 (2011).

5. S. K. Libutti, G. F. Paciotti, A. A. Byrnes, H. R. Alexander, Jr., W. E. Gannon, M. Walker, G. D. Seidel, N. Yuldasheva, and L. Tamarkin, "Phase I and pharmacokinetic studies of CYT-6091, a novel PEGylated colloidal gold-rhTNF nanomedicine," Clinical cancer research : an official journal of the American Association for Cancer Research 16, 6139-6149 (2010).

6. A. Agarwal, S. W. Huang, M. O'Donnell, K. C. Day, M. Day, N. Kotov, and S. Ashkenazi, "Targeted gold nanorod contrast agent for prostate cancer detection by photoacoustic imaging," J Appl Phys 102(2007).

7. A. K. Oyelere, P. C. Chen, X. H. Huang, I. H. El-Sayed, and M. A. El-Sayed, "Peptide-conjugated gold nanorods for nuclear targeting," Bioconjugate Chem 18, 1490-1497 (2007).

8. N. J. Durr, T. Larson, D. K. Smith, B. A. Korgel, K. Sokolov, and A. Ben-Yakar, "Two-photon luminescence imaging of cancer cells using molecularly targeted gold nanorods," Nano Lett 7, 941-945 (2007).

9. J. Park, A. Estrada, J. A. Schwartz, P. Diagaradjane, S. Krishnan, A. K. Dunn, and J. W. Tunnell, "Intra-Organ Biodistribution of Gold Nanoparticles Using Intrinsic Two-Photon-Induced Photoluminescence," Laser Surg Med 42, 630-639 (2010).

10. X. M. Qian, X. H. Peng, D. O. Ansari, Q. Yin-Goen, G. Z. Chen, D. M. Shin, L. Yang, A. N. Young, M. D. Wang, and S. M. Nie, "In vivo tumor targeting and spectroscopic detection with surface-enhanced Raman nanoparticle tags," Nat Biotechnol 26, 83-90 (2008).

11. W. H. De Jong, W. I. Hagens, P. Krystek, M. C. Burger, A. J. A. M. Sips, and R. E. Geertsma, "Particle size-dependent organ distribution of gold nanoparticles after intravenous administration," Biomaterials 29, 1912-1919 (2008).

12. Y. Akiyama, T. Mori, Y. Katayama, and T. Niidome, "The effects of PEG grafting level and injection dose on gold nanorod biodistribution in the tumor-bearing mice," J Control Release 139, 81-84 (2009).

13. J. F. Hainfeld, D. N. Slatkin, T. M. Focella, and H. M. Smilowitz, "Gold nanoparticles: a new X-ray contrast agent," The British journal of radiology 79, 248-253 (2006).

14. Y. S. Chen, W. Frey, S. Kim, P. Kruizinga, K. Homan, and S. Emelianov, "Silica-Coated Gold Nanorods as Photoacoustic Signal Nanoamplifiers," Nano Lett 11, 348-354 (2011).

15. C. L. Zavaleta, B. R. Smith, I. Walton, W. Doering, G. Davis, B. Shojaei, M. J. Natan, and S. S. Gambhir, "Multiplexed imaging of surface enhanced Raman scattering nanotags in

living mice using noninvasive Raman spectroscopy," P Natl Acad Sci USA 106, 13511-13516 (2009).

16. L. Tong, Q. S. Wei, A. Wei, and J. X. Cheng, "Gold Nanorods as Contrast Agents for Biological Imaging: Optical Properties, Surface Conjugation and Photothermal Effects," Photochem Photobiol 85, 21-32 (2009).

17. J. Fang, H. Nakamura, and H. Maeda, "The EPR effect: Unique features of tumor blood vessels for drug delivery, factors involved, and limitations and augmentation of the effect," Advanced drug delivery reviews 63, 136-151 (2011).

18. D. Huang, E. A. Swanson, C. P. Lin, J. S. Schuman, W. G. Stinson, W. Chang, M. R. Hee, T. Flotte, K. Gregory, C. A. Puliafito, and J. G. Fujimoto, "Optical Coherence Tomography," Science 254, 1178-1181 (1991).

19. J. G. Fujimoto, "Optical coherence tomography for ultrahigh resolution in vivo imaging," Nat Biotechnol 21, 1361-1367 (2003).

20. G. J. Liu, A. J. Lin, B. J. Tromberg, and Z. P. Chen, "A comparison of Doppler optical coherence tomography methods," Biomedical optics express 3, 2669-2680 (2012).

21. A. Mariampillai, B. A. Standish, E. H. Moriyama, M. Khurana, N. R. Munce, M. K. K. Leung, J. Jiang, A. Cable, B. C. Wilson, I. A. Vitkin, and V. X. D. Yang, "Speckle variance detection of microvasculature using swept-source optical coherence tomography," Optics letters 33, 1530-1532 (2008).

22. B. J. Vakoc, R. M. Lanning, J. A. Tyrrell, T. P. Padera, L. A. Bartlett, T. Stylianopoulos, L. L. Munn, G. J. Tearney, D. Fukumura, R. K. Jain, and B. E. Bouma, "Three-dimensional microscopy of the tumor microenvironment in vivo using optical frequency domain imaging," Nat Med 15, 1219-U1151 (2009).

23. R. John, R. Rezaeipoor, S. G. Adie, E. J. Chaney, A. L. Oldenburg, M. Marjanovic, J. P. Haldar, B. P. Sutton, and S. A. Boppart, "In vivo magnetomotive optical molecular imaging using targeted magnetic nanoprobes," P Natl Acad Sci USA 107, 8085-8090 (2010).

24. D. Jacob, R. L. Shelton, and B. E. Applegate, "Fourier domain pump-probe optical coherence tomography imaging of Melanin," Opt Express 18, 12399-12410 (2010).

25. A. L. Oldenburg, M. N. Hansen, T. S. Ralston, A. Wei, and S. A. Boppart, "Imaging gold nanorods in excised human breast carcinoma by spectroscopic optical coherence tomography," J Mater Chem 19, 6407-6411 (2009).

26. M. C. Skala, M. J. Crow, A. Wax, and J. A. Izatt, "Photothermal Optical Coherence Tomography of Epidermal Growth Factor Receptor in Live Cells Using Immunotargeted Gold Nanospheres," Nano Lett 8, 3461-3467 (2008).

27. J. M. Tucker-Schwartz, T. A. Meyer, C. A. Patil, C. L. Duvall, and M. C. Skala, "In vivo photothermal optical coherence tomography of gold nanorod contrast agents," Biomed Opt

Express 3, 2881-2895 (2012).

28. D. C. Adler, S. W. Huang, R. Huber, and J. G. Fujimoto, "Photothermal detection of gold nanoparticles using phase-sensitive optical coherence tomography," Opt Express 16, 4376-4393 (2008).

29. Y. Jung, R. Reif, Y. G. Zeng, and R. K. Wang, "Three-Dimensional High-Resolution Imaging of Gold Nanorods Uptake in Sentinel Lymph Nodes," Nano Lett 11, 2938-2943 (2011).

30. J. M. Tucker-Schwartz, T. Hong, D. C. Colvin, Y. Q. Xu, and M. C. Skala, "Dual-modality photothermal optical coherence tomography and magnetic-resonance imaging of carbon nanotubes," Opt Lett 37, 872-874 (2012).

31. A. S. Paranjape, R. Kuranov, S. Baranov, L. L. Ma, J. W. Villard, T. Y. Wang, K. V. Sokolov, M. D. Feldman, K. P. Johnston, and T. E. Milner, "Depth resolved photothermal OCT detection of macrophages in tissue using nanorose," Biomed Opt Express 1, 2-16 (2010).

32. S. K. Hobbs, W. L. Monsky, F. Yuan, W. G. Roberts, L. Griffith, V. P. Torchilin, and R. K. Jain, "Regulation of transport pathways in tumor vessels: Role of tumor type and microenvironment," P Natl Acad Sci USA 95, 4607-4612 (1998).

33. H. S. Choi, W. Liu, P. Misra, E. Tanaka, J. P. Zimmer, B. I. Ipe, M. G. Bawendi, and J. V. Frangioni, "Renal clearance of quantum dots," Nat Biotechnol 25, 1165-1170 (2007).

34. A. K. Iyer, G. Khaled, J. Fang, and H. Maeda, "Exploiting the enhanced permeability and retention effect for tumor targeting," Drug Discov Today 11, 812-818 (2006).

35. C. J. Murphy, T. K. San, A. M. Gole, C. J. Orendorff, J. X. Gao, L. Gou, S. E. Hunyadi, and T. Li, "Anisotropic metal nanoparticles: Synthesis, assembly, and optical applications," J Phys Chem B 109, 13857-13870 (2005).

36. M. D. Wojtkowski, T. H. Ko, J. G. Fujimoto, T. Bajraszewski, I. Gorczynska, P. Targowski, A. Kowalczyk, J. S. Schuman, and J. S. Duker, "Ultrahigh speed, ultrahigh resolution optical coherence tomography using spectral domain detection," Invest Ophth Vis Sci 45, U50-U50 (2004).

37. S. Moon, S. W. Lee, and Z. P. Chen, "Reference spectrum extraction and fixed-pattern noise removal in optical coherence tomography," Optics express 18, 24395-24404 (2010).

38. T. Akkin, C. Joo, and J. F. de Boer, "Depth-resolved measurement of transient structural changes during action potential propagation," Biophysical journal 93, 1347-1353 (2007).

39. H. C. Hendargo, R. Estrada, S. J. Chiu, C. Tomasi, S. Farsiu, and J. A. Izatt, "Automated non-rigid registration and mosaicing for robust imaging of distinct retinal capillary beds using speckle variance optical coherence tomography," Biomed Opt Express 4, 803-821 (2013).

40. S. D. Perrault, C. Walkey, T. Jennings, H. C. Fischer, and W. C. W. Chan, "Mediating Tumor Targeting Efficiency of Nanoparticles Through Design," Nano letters 9, 1909-1915 (2009).

41. M. R. Dreher, W. G. Liu, C. R. Michelich, M. W. Dewhirst, F. Yuan, and A. Chilkoti, "Tumor vascular permeability, accumulation, and penetration of macromolecular drug carriers," J Natl Cancer I 98, 335-344 (2006).

42. T. Y. Wang, D. Halaney, D. Ho, M. D. Feldman, and T. E. Milner, "Two-photon luminescence properties of gold nanorods," Biomed Opt Express 4, 584-595 (2013).

43. Arnida, M. M. Janat-Amsbury, A. Ray, C. M. Peterson, and H. Ghandehari, "Geometry and surface characteristics of gold nanoparticles influence their biodistribution and uptake by macrophages," European journal of pharmaceutics and biopharmaceutics : official journal of Arbeitsgemeinschaft fur Pharmazeutische Verfahrenstechnik e.V 77, 417-423 (2011).

44. A. A. Manzoor, L. H. Lindner, C. D. Landon, J. Y. Park, A. J. Simnick, M. R. Dreher, S. Das, G. Hanna, W. Park, A. Chilkoti, G. A. Koning, T. L. M. ten Hagen, D. Needham, and M. W. Dewhirst, "Overcoming Limitations in Nanoparticle Drug Delivery: Triggered, Intravascular Release to Improve Drug Penetration into Tumors," Cancer Res 72, 5566-5575 (2012).

45. H. M. Subhash, H. Xie, J. W. Smith, and O. J. T. McCarty, "Optical detection of indocyanine green encapsulated biocompatible poly (lactic-co-glycolic) acid nanoparticles with photothermal optical coherence tomography," Opt Lett 37, 981-983 (2012).

46. S. W. Jones, R. A. Roberts, G. R. Robbins, J. L. Perry, M. P. Kai, K. Chen, T. Bo, M. E. Napier, J. P. Y. Ting, J. M. DeSimone, and J. E. Bear, "Nanoparticle clearance is governed by Th1/Th2 immunity and strain background," J Clin Invest 123, 3061-3073 (2013).

47. G. Y. Guan, R. Reif, Z. H. Huang, and R. K. K. Wang, "Depth profiling of photothermal compound concentrations using phase sensitive optical coherence tomography," J Biomed Opt 16(2011).

48. C. Pache, N. L. Bocchio, A. Bouwens, M. Villiger, C. Berclaz, J. Goulley, M. I. Gibson, C. Santschi, and T. Lasser, "Fast three-dimensional imaging of gold nanoparticles in living cells with photothermal optical lock-in Optical Coherence Microscopy," Opt Express 20, 21385-21399 (2012).

CHAPTER 5

Apply Optical Lock-in Techniques to Increase Throughput and Allow for Real Time *In Vivo* Imaging of Multiple Contrast Agents

Tucker-Schwartz JM, Lapierre-Landry M, Patil CA, Skala MC, "Photothermal optical lock-in optical coherence tomography for *in vivo* imaging," *Biomedical Optics Express,* 2015; 6(6):2268-2282.

5.1 Abstract

Photothermal OCT (PTOCT) provides high sensitivity to molecular targets in tissue, and occupies a spatial imaging regime that is attractive for small animal imaging. However, current implementations of PTOCT require extensive temporal sampling, resulting in slow frame rates and a large data burden that limit its *in vivo* utility. To address these limitations, we have implemented optical lock-in techniques for photothermal optical lock-in OCT (poli-OCT), and demonstrated the *in vivo* imaging capabilities of this approach. The poli-OCT signal was assessed in tissue-mimicking phantoms containing indocyanine green (ICG), an FDA approved small molecule that has not been previously imaged *in vivo* with PTOCT. Then, the effects of *in vivo* blood flow and motion artifact were assessed and attenuated, and *in vivo* poli-OCT was demonstrated with both ICG and gold nanorods as contrast agents. Experiments revealed that poli-OCT signals agreed with optical lock-in theory and the bio-heat equation, and the system exhibited shot noise limited performance. In phantoms containing biologically relevant concentrations of ICG (1 μg/ml), the poli-OCT signal was significantly greater than control phantoms ($p<0.05$), demonstrating sensitivity to small molecules. Finally, *in vivo* poli-OCT of ICG identified the lymphatic vessels in a mouse ear, and also identified low concentrations (200 pM) of gold nanorods in subcutaneous injections at frame rates ten times faster than previously reported. This work illustrates that future *in vivo* molecular imaging studies could benefit from the improved acquisition and analysis times enabled by poli-OCT.

5.2 Introduction

In vivo molecular imaging in animal models serves a vital role in medical research, providing fundamental insights into mechanisms of disease formation and progression [1], as well as drug discovery [2]. Unfortunately, current small animal molecular imaging tools supply either high resolution or a wide field of view, but not both. For example, fluorescence microscopy can image molecular contrast *in vivo* [3, 4] at subcellular (<1 μm) resolution, but only over a small, depth-limited field of view of a few hundred micrometers. Unlike microscopy, whole body imaging (e.g. bioluminescence imaging, positron emission tomography, magnetic resonance imaging) of contrast agents provide molecular images without practical limitations to imaging depth. However, whole body imaging approaches suffer from limited spatial resolution (mm-cm) [2]. Optical coherence tomography (OCT) fills the niche of high resolution (1-30 μm), wide field of view (5-10 mm), and deep (1-3 mm) three-dimensional optical imaging [5]. OCT is a cost-effective noncontact imaging tool, capable of MHz line rates [6]. Using low coherence interferometry of near infrared (NIR) photons, OCT provides depth-resolved images of tissue structure, vessel morphology [7], and blood flow [8]. Yet, OCT is not especially sensitive to molecular targets, since the index of refraction varies weakly amongst most molecular species in tissue.

Photothermal OCT (PTOCT), a functional extension of OCT, enhances the sensitivity and specificity of OCT to molecular sources of contrast [9, 10]. Similar to photoacoustic imaging, another emerging molecular imaging technique, PTOCT images the effects of photon absorption. Unlike photoacoustic imaging, PTOCT is a contact-free tool that images heat release after photon absorption, rather than the release of acoustic waves from thermally confined laser pulses. After photon absorption by a chromophore, heat released into the microenvironment causes thermoelastic expansion and slight changes in local refractive index, which in turn alter

the observed optical path length. PTOCT quantifies these photothermal-induced optical path length variations using phase-sensitive OCT measurements and post-acquisition frequency analysis. PTOCT has been used to image a range of exogenous and endogenous forms of contrast *in vitro* and *ex vivo* including gold nanospheres [9], gold nanorods [11, 12], gold nanoshells [10, 13, 14], carbon nanotubes [15], and blood [16]. Recently, PTOCT was expanded to *in vivo* applications, and used to track *in vivo* heterogeneities in intratumoral nanoparticle distributions [17]. Even with its recent success, PTOCT still suffers from impracticalities that limit its widespread use for *in vivo* molecular imaging. In the traditional PTOCT implementation for imaging trace concentrations of contrast agents, one A-scan position is temporally sampled hundreds to thousands of times, and heating dynamics are identified from the phase of the depth-resolved OCT signal using post-acquisition frequency analysis. This post-acquisition frequency analysis scheme requires time consuming data acquisition, excessive data collection, and lengthy offline signal analysis. These limitations make traditional PTOCT impractical and lengthy for multi-animal *in vivo* time-course studies, and have therefore restricted its use in research.

Optical lock-in detection, a real-time alternative to post-acquisition frequency analysis, has been previously implemented for photothermal microscopy of cell monolayers [18]. This approach was recently expanded to depth-resolved photothermal optical coherence microscopy [19] and two-dimensional wide field photothermal microscopy [20] of gold nanospheres in cell monolayers. Specifically, a photothermal optical lock-in optical coherence microscopy (poli-OCM) technique was developed, allowing for kHz line rate photothermal imaging with OCM systems [19]. By imposing a frequency shift on the reference arm light, this optical lock-in technique removes the temporal sampling constraints of photothermal OCM, thus reducing its data burden and effectively transforming the OCM signal to a real time image of photothermal heating. However, optical lock-in acquisition has yet to be demonstrated in optically thick

samples or *in vivo*, where confounding factors such as motion and blood flow introduce artifacts into the image.

Here, optical lock-in techniques are implemented for real time imaging of NIR absorbing contrast agents *in vivo* using photothermal optical lock-in optical coherence tomography (poli-OCT). An *in vivo* poli-OCT system was built and tested using tissue-mimicking phantoms. In addition, motion artifact and blood flow, which are confounding factors unique to *in vivo* imaging, were characterized and attenuated. Finally, contrast agents were imaged *in vivo* using frame rates at least 10 fold faster than previous *in vivo* publications [11, 17]. Two contrast agents were imaged *in vivo* in order to demonstrate the versatility of poli-OCT to a range of contrast agents, including an FDA approved small molecule (indocyanine green: ICG) that has not been previously measured *in vivo* with PTOCT, as well as gold nanorods. Overall, the development of poli-OCT for *in vivo* use provides improved *in vivo* molecular imaging in the unique spatial niche of OCT.

5.3 Methods

5.3.1 poli-OCT Imaging

The theory for poli-OCT has previously been published [19]. In an interferometric imaging system, a carrier frequency is introduced by imposing a temporal frequency shift (Ω_R) onto the reference arm. In the presence of photon-absorbing molecules and frequency matched photothermal-induced phase oscillations (Ω_P), the resulting interference pattern is demodulated. Low pass filtering then distinguishes the demodulated signal from background. Temporal integration by the CCD serves as the low pass filter, attenuating the signal due to static scatterers to zero, and maintaining the demodulated signal due to absorption (Fig. 5.1a). To attenuate the signal due to scatterers, the integration time (τ) of the CCD must be set to a multiple (n) of the frequency shift period (T_0, where $\tau = n/\Omega_R = nT_0$). This optical lock-in technique transforms the

OCT signal as a function of depth (z), defined as the amplitude of the tomogram (|S(z)|) after Fourier transform of the interference signal, to a real time image of photothermal heating (i.e. poli-OCT). The poli-OCT signal at a given depth (|S(z)|) where an absorber such as ICG is present is described by

$$|S(z)| \propto \alpha\tau r(z) r_r \sqrt{P_s P_r} \qquad (5.1)$$

where α describes the magnitude of the photothermal heating signal, $r(z)$ and r_r are the reflectivities at depth z in the sample and at the reference arm, respectively and P_s and P_r are the power to the sample and reference arm, respectively [19].

For *in vivo* imaging, a custom poli-OCT system was constructed with an 860 nm center wavelength, 40 nm bandwidth (Fig. 5.1b, yellow, inset), superluminescent diode imaging laser (SLD, Fig. 5.1b). Light from the SLD was split between the sample and reference arms using a 50:50 fiber coupler (50:50, Fig. 5.1b). A programmable frequency shift (Ω_R) was applied to the reference arm using the beat frequency of two acousto-optic modulators (AOMs) in serial configuration. The first AOM (AOM 1, Fig. 5.1b) performed a frequency downshift at the AOM central carrier frequency (ω_c, where ω_c = 100 MHz), while the second AOM (AOM 2, Fig. 5.1b) performed a slightly offset frequency upshift ($\omega_c + \Omega_R$). AOMs operate on the MHz time scale, therefore the beat frequency (Ω_R) of AOM 1 and AOM 2 was used to shift the operational range to the Hz and kHz regime, where photothermal effects are large enough to image with our focused spot size (24 μm). A custom phase-locked AOM driver (Brimrose) controlled the frequency shifts and power throughput of both AOMs, with an operational range of 80-120 MHz and 1 Hz resolution. Knife edges removed zeroth-order output beams from the AOMs, and the reference arm light was focused into a fiber coupler for interferometry. In the sample arm, polarization optics were used to control power to the sample and minimize autocorrelation artifacts. Light output from the 50:50 fiber coupler was collimated and the polarization angle was tuned using a half wave plate

(HWP, Fig. 5.1b). A linear polarizer (LP, Fig. 5.1b) then rejected any light off axis from the reflective mode of the polarization beam splitter (PBS, Fig. 5.1b). After reflection towards the sample by the PBS, a quarter wave plate (QWP, Fig. 5.1b) controlled the polarization shape of the sample arm light, from circular (45 degrees) to linear (0 degrees). A 3X scan lens (Thorlabs) then focused the light onto the sample (depth of field = 1.15 mm, $1/e^2$ spot size = 24 μm). Any light backreflected from the sample that matched the transmission state of the PBS was collected into a fiber coupler for interferometry. The output interference signal from the fiber coupler was dispersed by a spectrometer and captured by a CCD with tunable integration time from 50 to 10,000 μs. To achieve optical lock-in detection, the integration time (τ) of the CCD was set to a multiple (n) of the frequency shift period (T_0, where $\tau = n/\Omega_R = nT_0$). The spectrometer, galvo drive electronics, and software from a commercial OCT system (Bioptigen) were used for the poli-OCT system.

Photothermal heating was achieved with a wavelength tunable Titanium:Sapphire (Fig. 5.1b) photothermal laser (PT laser). The wavelength of the PT laser (Fig. 5.1b, green, inset) was tuned to match the absorption of the selected contrast agent, as shown for ICG (Fig 1b, inset). To induce photothermal phase oscillations, the PT laser was intensity modulated at the same frequency as the reference arm (Ω_P, where $\Omega_P = \Omega_R$) using a third AOM (AOM 3, Fig. 5.1b), and then fiber coupled into the imaging system. Commercial software (Brimrose) controlled the frequency shifts in all three AOMs, while analog inputs (0-1 V) drove the intensity of the output RF signal. The RF signals sent to AOM 1 and AOM 2 were attenuated, mixed, and then low pass filtered using inline RF electronics to isolate the beat waveform. The beat waveform from AOM 1 and AOM 2 was digitally acquired, conditioned in LabVIEW to a square wave frequency matched to the beat of AOMs 1 and 2 (Ω_P=Ω_R), and output as an analog waveform to intensity modulate AOM 3.

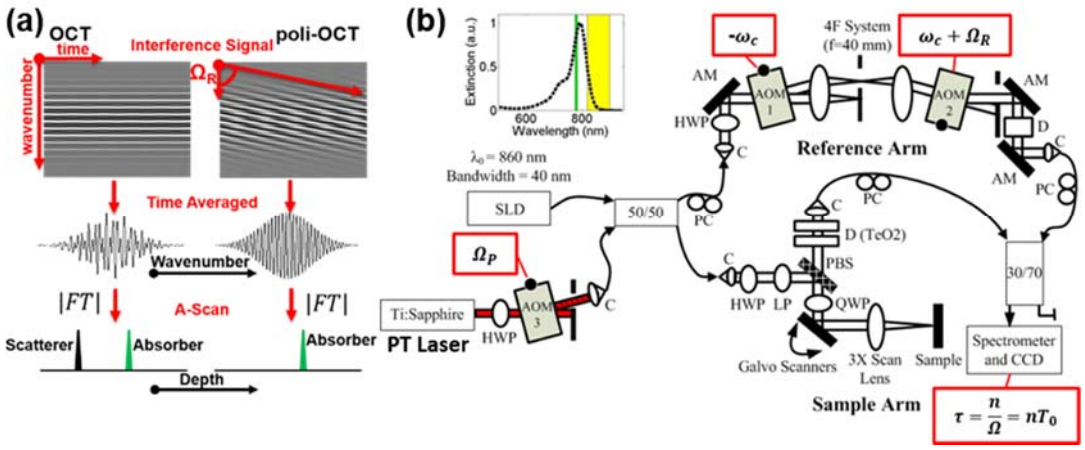

Fig. 5.1. Photothermal optical lock-in OCT. (a) In poli-OCT, a frequency shift (Ω_R) is imposed on the reference arm, which attenuates time-averaged interference signals from static non-absorbing samples. (b) A custom poli-OCT system was constructed for *in vivo* imaging. ICG (extinction spectrum, inset) was heated using 770 nm light (green, inset) from the Ti:Sapphire photothermal laser (PT laser). An 860 nm wavelength, 40 nm bandwidth, superluminscent diode (SLD) was used for imaging (yellow, inset). D (TeO2): Dispersion matching of AOM crystals; D: Dispersion compensation; HWP: Half wave plate; LP: Linear polarizer; QWP: Quarter wave plate; PBS: Polarization sensitive beam splitter; AOM: Acousto-optic modulator; SLD: Superluminescent diode; C: Fiber collimation/coupling; AM: Alignment mirror; PC: Polarization controller.

5.3.2 Image Processing

Unlike traditional PTOCT which requires Fourier analysis of the digitally sampled temporal phase data [11], poli-OCT images require the same image processing as standard OCT images. If the instrumentation and signal requirements are met, either an OCT ($\Omega_R = 0$ Hz) or poli-OCT ($\Omega_R \neq 0$ Hz and $\Omega_R = n/\tau$) image are acquired. To process images, data was first resampled from linearity in wavelength to linearity in wavenumber. The interference spectrum was then numerically dispersion corrected [21], followed by a Fourier transform along the wavenumber dimension to create the depth-resolved image. Fixed pattern noise removal was performed on the complex signal [22], and the poli-OCT signal was calculated as the non-log compressed magnitude of the depth-resolved data.

5.3.3 poli-OCT Imaging of Phantoms

To quantify system performance and optimize the system for *in vivo* imaging, scattering phantoms were imaged with poli-OCT under varying parameters. Tissue mimicking phantoms containing ICG for photothermal absorption were created from clear silicone (Quantum Silicones) consisting of two parts (A and B) mixed at a 10:1 weight ratio. Rutile titanium dioxide (TiO_2, Sigma Aldrich) was added to a final concentration of 4.1 mg/g to mimic human skin scattering [23]. The TiO_2 was added to silicone component A, mixed for two minutes, and then degassed for two minutes using a planetary centrifugal mixer (Thinky USA). ICG diluted into a small volume of 70% ethanol was added to component B of the silicone mixture to a final concentration of 8 μg/ml, then mixed and degassed. Components A and B were then mixed and degassed. The final mixture was placed in a petri dish under vacuum at 29 inches of Hg for five minutes with brief returns to standard pressure every minute, and left to cure for 12 hours at 70 degree Celsius. Phantoms were imaged using a 2 mm B-scan (400 A-scans/B-scan) and data was averaged across each B-scan including the first 400 μm in depth in the phantom. Baseline acquisition parameters for phantom studies were 500 μW of SLD sample arm power, 25 mW average PT laser power to the sample, 6 ms CCD integration time, and 500 Hz frequency shift ($\Omega_P = \Omega_R$). In addition, reference arm power was adjusted to fill approximately 80% of the CCD dynamic range. Measurements were acquired with the PT laser on (true poli-OCT signal), PT laser off (background poli-OCT signal), and with the sample arm blocked (noise floor). The poli-OCT signal was calculated as the non-log compressed OCT magnitude signal. Similar to previous work [19, 24], the signal to noise ratio (SNR) was defined as the squared magnitude of the poli-OCT signal with the PT laser on divided by the variance of the image signal with the sample arm blocked. Means and standard deviations were assessed over 10 repeated scans, and statistical significance was calculated using a non-parametric Wilcoxon Rank Sum test ($p<0.05$).

The integration time of the CCD and the sample arm power were altered individually, and the poli-OCT signal and SNR were calculated and compared to photothermal optical lock-in theory [19] to assess for shot-noise limited performance at millisecond integration times. First, while maintaining the system frequency shift at 500 Hz, the integration time of the CCD ($\tau = nT_0$, where $T_0 = 2$ ms) was increased by integer multiples of the frequency shift period (T_0) between 2 ms and 8 ms. For each integration time, the reference arm power was adjusted to fill 80% of the CCD dynamic range. In addition, while maintaining a constant integration time and frequency shift, the SLD power to the sample was increased from 350 to 900 μW.

Next, imaging parameters that directly affect the magnitude of the photothermal heating oscillations were altered and trends were compared to approximations of the bio-heat conduction equation [25] as previously reported using traditional PTOCT [11]. The PT laser frequency ($\Omega_P = \Omega_R$) was varied from 200 Hz to 800 Hz while maintaining the integration time of the CCD at 10 ms. Then, the average PT laser power on the sample was varied between 10 and 30 mW. Last, the concentration of ICG in the phantom was varied between 0 and 17 μg/ml and imaged with 10 ms CCD integration time, 300 Hz frequency shift, and 30 mW average PT laser power.

Finally, theoretical assumptions of poli-OCT were experimentally validated. According to theory [19], the presence of the photothermal signal in the poli-OCT image requires that the intensity modulation of the PT laser (Ω_P) occurs at the same frequency as the reference arm frequency shift (Ω_R). Therefore, Ω_P was varied between 250 Hz and 750 Hz in 50 Hz increments, while maintaining Ω_R at 500 Hz. In addition, in order to reject background scattering, the integration time of the CCD (τ) must be set to a multiple of the frequency shift period (T_0). To experimentally validate this assumption, while maintaining a constant frequency shift of 500 Hz ($T_0 = 2$ ms), the integration time was altered from 4 ms ($\tau = 2T_0$) to 8 ms ($\tau = 4T_0$) in 500 μs ($T_0/4$) increments.

5.3.4 Effect of Motion and Blood Flow

All animal studies were approved by the Vanderbilt University Animal Care and Use Committee and meet the NIH guidelines for animal welfare. Transitioning the imaging system to *in vivo* applications requires an understanding of the effects of motion and blood flow on the poli-OCT signal, specifically on the rejection of the background scattering signal (i.e. PT laser off). Therefore, a 4 by 4 mm (400 A-scans/B-scan, 400 B-scans/C-scan) rectangular volume was acquired of a mouse ear (The Jackson Laboratory, Foxn1^{nu}/ Foxn1^{nu}) using 10 ms CCD integration time, 500 Hz frequency shift, and without the PT laser. A 1 by 1 mm (100 A-scans/B-scan, 100 B-scans/C-scan) rectangular volume was then acquired while varying the reference arm frequency shift (Ω_R) from 100 to 2500 Hz. During imaging, the mouse was anesthetized using inhalant isoflurane (1.5-1.75%) while a closed-loop heating blanket maintained body temperature at 37 degrees Celsius.

5.3.5 *In Vivo* Imaging with poli-OCT

Photothermal imaging was performed *in vivo* in female nude mice (The Jackson Laboratory, Foxn1^{nu}/ Foxn1^{nu}) using poli-OCT. Mice were anesthetized during imaging using inhalant isoflurane (1.5-1.75%), and a closed-loop heating blanket maintained body temperature at 37 degrees Celsius. Contrast agents were imaged from within intradermal locations of the mouse ear, an optically accessible biological site for preclinical studies of cancer [26], immune response [27, 28], and lymphatics [29-31]. The mouse ear was firmly attached to a 10 ml scintillation vial using double sided tape which was in turn taped to the imaging stage. *En face* projections were created by taking the average signal across the depth dimension (~1 mm depth).

In the first demonstration of *in vivo* poli-OCT imaging to date, the lymphatic vessels of a healthy mouse ear were imaged with injected ICG in real time. Using a micromanipulator under OCT image guidance, a 31 gauge needle (Hamilton) was placed intradermally in the outer rim of

the mouse ear. Approximately 5 μl of 500 μg/ml ICG [31, 32] was injected, and removal of ICG from the interstitial space via lymphatic vessel drainage was imaged with a 3 by 3 mm (300 A-scans/B-scan, 300 B-scans/C-scan) rectangular volume medial to the injection site. An integration time of 6 ms was used, with 500 Hz frequency shift ($\Omega_P = \Omega_R$), and 30 mW of average PT laser power (770 nm) on the sample. Image volumes were acquired with the PT laser on, the PT laser off, and the frequency shift (Ω_R) set to 0 Hz (i.e. OCT). An accompanying speckle variance scan was acquired to identify native blood vessels over the 3 mm by 3 mm scan window. Speckle variance was calculated as the variance of the OCT magnitude signal over 10 repeated A-scans, acquired at a 10 kHz line rate [17].

Last, similar to previous publications [11], subcutaneous injections of gold nanorods were imaged with poli-OCT. Gold nanorods were manufactured and coated in poly(ethylene glycol) (PEG) according to previous methods [17], diluted to 400 pM concentration in water, then mixed 1:1 with Matrigel (Corning) to a final concentration of 200 pM. The Matrigel-gold nanorod solution was manually injected into the base of a mouse ear using a 28 gauge needle and allowed to solidify for 10 minutes. A 2.5 by 2.5 mm rectangular volume (250 A-scans/B-scan, 250 B-scans/C-scan) was imaged at the periphery of the injection site using 10 ms integration time, 500 Hz frequency shift ($\Omega_P = \Omega_R$), and 35 mW average PT laser power (740 nm) at the sample. Image volumes were captured with the PT laser on and off, and then again with a frequency shift (Ω_R) of 0 Hz. In a separate mouse, a control injection using Matrigel diluted 1:1 in water was imaged using identical image parameters. In addition, an overlapping speckle variance scan was acquired to identify native blood vessels. For *in vivo* imaging, output poli-OCT image volumes were median filtered in the *en face* dimension to reduce the effects of motion artifact and then average filtered. The poli-OCT image contrast was also adjusted to exclude signals near the noise floor, and contrast adjustments were kept consistent across each set of images.

5.4 Results

5.4.1 Imaging Scattering Phantoms

Tissue-mimicking phantoms containing ICG (8 μg/ml) and TiO_2 were imaged under variable system parameters to quantify poli-OCT performance and to optimize the system for *in vivo* imaging. ICG phantoms did not exhibit significant photobleaching after repeated measurements in the same phantom location, and the phantoms maintained their integrity over multiple months. Results were acquired for the poli-OCT signal with the PT laser on (PT laser (+)), the background signal with the PT laser off (PT laser (-)), and the noise floor with the sample arm blocked. Both the poli-OCT signal (black, $r^2 = 0.97$, Fig. 5.2a) and SNR ($r^2 = 0.97$, Fig. 5.2b) scaled linearly with the integration time of the CCD while the integration time was set to a multiple of the frequency shift period. The poli-OCT signal scaled with the square root of the sample arm power (black, $r^2 = 0.98$, Fig. 5.2c), while the SNR of the poli-OCT signal increased linearly with the sample arm power ($r^2 = 0.98$, Fig. 5.2d). The trends observed in Fig. 5.2 agree with the theory established for photothermal optical lock-in [19], while the trends in SNR agree with the theory for shot noise limited performance, the optimal operation mode for OCT systems [19, 24].

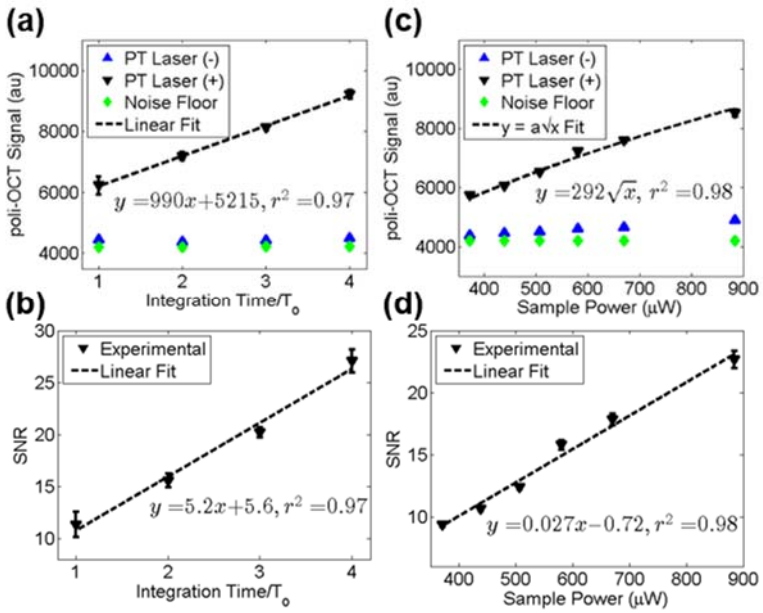

Fig. 5.2. Poli-OCT signal characterization in phantoms containing ICG (absorber) and TiO_2 (scatterer) while altering image system parameters. Solid phantoms were imaged with the PT laser on (black, top), the PT laser off (blue, top), and the sample arm blocked (green, top). (a) The poli-OCT signal (black) increased linearly with integration time (τ) set to multiples (n) of the frequency shift period (T_0). (b) The SNR of the poli-OCT signal increased linearly as well. (c) The poli-OCT signal (black) increased with the square root of the sample arm power, while (d) the SNR increased linearly. The poli-OCT signal agrees with theory [19], and SNR results are consistent with shot noise limited performance [19, 24].

Parameters that affect the magnitude of the photothermal oscillations were also examined. Increasing the PT laser frequency ($\Omega_P = \Omega_R$) from 200 to 800 Hz caused a nonlinear decay in the poli-OCT signal (Fig. 5.3a), while increasing the PT laser power resulted in a linear increase in poli-OCT signal (Fig. 5.3b, $r^2 = 0.99$). Scattering phantoms with varying ICG concentrations from 0 to 17 μg/ml displayed a linear increase in poli-OCT signal (Fig. 5.3c, $r^2 = 0.99$). Results in Fig. 5.3c include the removal of background signal (PT laser (-)) from the poli-OCT signal (PT laser (+)). Concentrations of ICG as low as 1 μg/ml displayed significantly increased ($p<0.05$, Fig. 5.3c inset) poli-OCT signal compared with scattering controls (red). ICG concentrations greater than 1 μg/ml can be reached at a tumor site when ICG is tagged to a systemically injected antibody, indicating that ICG and poli-OCT could potentially be used for *in vivo* molecular imaging studies in cancer, or to track delivery of antibody therapies (e.g. trastuzumab in breast cancer) [33]. The

effects seen from increased PT laser frequency, PT laser power, and absorber concentration all agree with previous traditional PTOCT data and a model of the bio-heat conduction equation [11, 25].

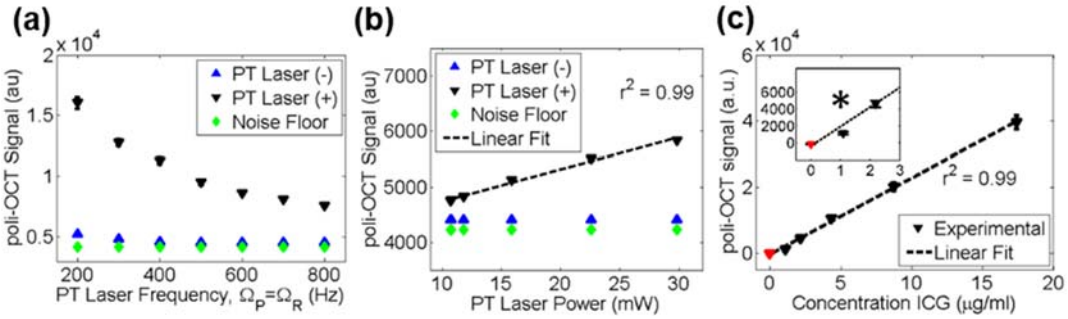

Fig. 5.3. Poli-OCT signal characterization in phantoms containing ICG (absorber) and TiO_2 (scatterer) while altering photothermal signal magnitudes. (a) As the PT laser frequency (Ω_P, where $\Omega_P = \Omega_R$) is increased, the poli-OCT signal (black) decreases nonlinearly. (b) Increasing PT laser power caused a linear increase in poli-OCT signal. (c) Increasing the concentration of the ICG resulted in a linear increase in the poli-OCT signal. The average signal from n=10 repeated scans showed a significant increase (*$p<0.05$, figure inset) with 1 μg/ml concentration of ICG compared to the control (red).

Theoretical assumptions for photothermal optical lock-in were experimentally validated as well. Mismatch between the PT laser modulation frequency (Ω_P, Fig. 5.4a x-axis) and the reference arm frequency shift (Ω_R, Fig. 5.4a red vertical line) caused a large falloff in poli-OCT signal (Fig. 5.4a). There is however, a broad range of frequencies over which the poli-OCT signal remains high (FWHM ~150 Hz), indicating that Ω_P and Ω_R do not need to be precisely frequency locked to measure photothermal absorption. It should be noted that mismatching Ω_P and Ω_R resulted in temporal oscillations in the image signal (data not shown). Additionally, altering the integration time from 4 ms to 8 ms while maintaining a frequency shift of 500 Hz (T_0 = 2 ms) altered both the poli-OCT signal (PT laser (+), black, Fig. 5.4b) and background scattering signal (PT laser (-), blue, Fig. 5.4b). The poli-OCT background signal (PT laser (-), blue, Fig. 5.4b) approached the noise floor (Noise Floor, green, Fig. 5.4b) only when CCD integration times (τ) were integer multiples (n) of the frequency shift period (T_0) (Fig. 5.4b, red vertical lines). Therefore, any source

of alteration to the programmed frequency shift (Ω_R) in the signal could result in incomplete removal of static background scatterers from the poli-OCT image. Slight differences between background and noise floor were due to the autocorrelation signal.

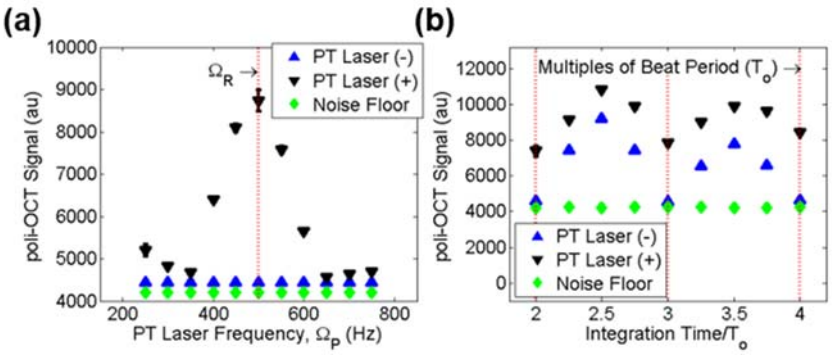

Fig. 5.4. Poli-OCT signal characterization in phantoms containing ICG (absorber) and TiO_2 (scatterer), validating theoretical assumptions. (a) When the PT laser modulation frequency (Ω_P, x-axis) is mismatched from the reference arm frequency shift (Ω_R, red vertical line), the poli-OCT signal (black) is attenuated. (b) The poli-OCT signal with the PT laser on (black) and off (blue) are both minimized at CCD integration times (τ) that are integer multiples (n) of the frequency shift period (T_0) (red vertical lines). The scattering signal (blue) is effectively removed only when the integration time is equal to a multiple of the frequency shift period.

5.4.2 Effect of Motion and Blood Flow

As demonstrated by phantom experiments (blue, Fig. 5.4b), a false positive background signal emerges when the CCD integration time is not divisible by the frequency shift period. Motion artifact and blood flow expected during *in vivo* imaging impose their own frequency shifts on the image signal, causing the interference pattern to carry a frequency shift different from the programmed one (Ω_R). Therefore, it was hypothesized that motion artifact and blood flow would cause incomplete rejection of a non-absorbing sample. As predicted, motion artifacts due to breathing and cardiac cycles of the mouse as well as blood flow within vessels result in incomplete rejection of the background scattering signal (Fig. 5.5a). Although the background signal due to blood flow and motion seem indistinguishable in one B-scan (Fig. 5.5a), the *en face* average intensity projection from the complete image volume (Fig. 5.5b) reveals the transient and streaking features of the motion artifact (red arrows, Fig. 5.5a-b), and the more structured nature of the flow

signal (green arrows, Fig. 5.5a-b). Motion artifact-induced streaking was reduced with a median filter in the *en face* dimension over a 4X4 pixel neighborhood. The filter maintains the structure of the flow found in the vessels, while attenuating streaking artifacts in the image (Fig. 5.5c). The overall background signal (i.e. average image signal with the PT laser off) including movement and blood flow from *in vivo* imaging can be further attenuated by increasing the frequency shift in the reference arm (Ω_R, Fig. 5.5d). Increased photothermal frequency (Ω_R) results in both reduced background signal and reduced photothermal signal strength (Fig. 5.3a). Therefore, the photothermal frequency must be carefully selected for each *in vivo* application.

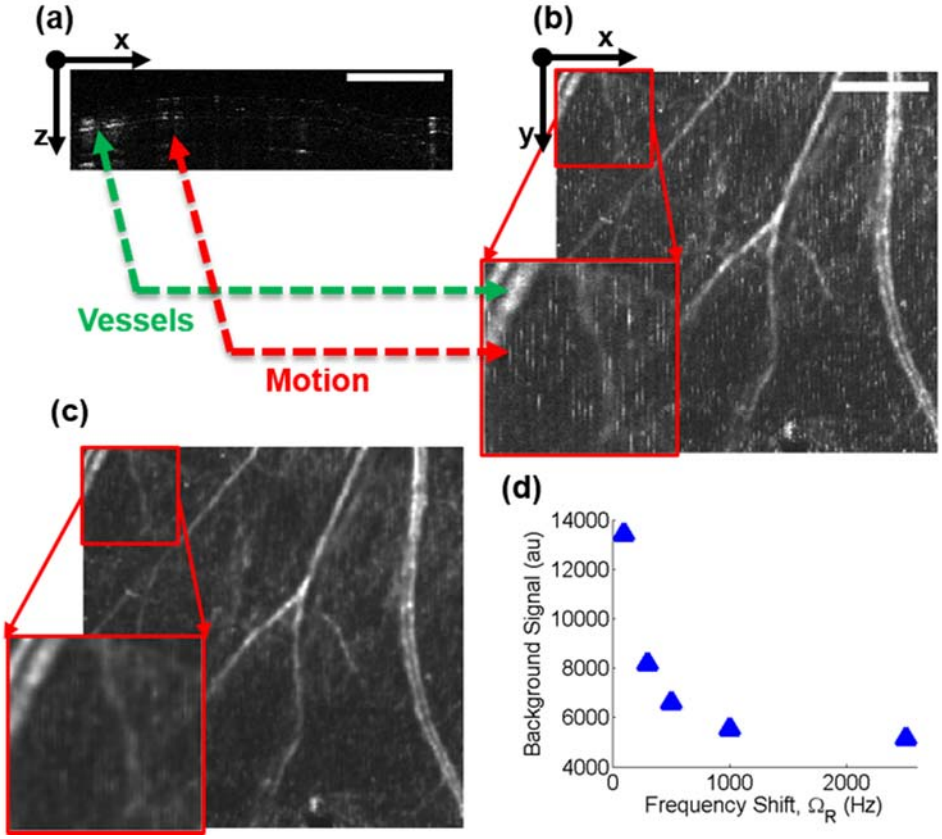

Fig. 5.5. Motion and blood flow affects *in vivo* poli-OCT signal. A 3D image volume of a mouse ear with the PT laser off shows motion artifact and flow manifested as poli-OCT background signal. (a) A representative B-scan shows false positive background signal due to blood flow in vessels (green arrow) and motion artifact (red arrow). (b) The same image volume represented as an *en face* projection shows the signals due to motion artifact and flow. (c) Median filtering the 3D image volume attenuates artifacts due to motion. (d) The average background signal in the image volume is attenuated with increasing frequency shifts in the reference arm (Ω_R, x-axis). Red boxes show 2X zoomed image regions. Scale bar = 1 mm.

5.4.3 *In Vivo* Imaging with poli-OCT

Recently, ICG has been used as a lymphatic imaging contrast agent due to its bright NIR fluorescence and efficient lymphatic removal [31, 32]. Therefore, as a demonstration of *in vivo* poli-OCT, ICG was imaged from within the lymphatics during its removal from the mouse ear. B-scans through the mouse ear include OCT (gray) and poli-OCT (green) data (Fig. 5.6a, 6b). Morphological features are resolved through the full thickness of the ear in the OCT magnitude data (Fig. 5.6a, 6b), and the lymphatics that drain the interstitial ICG are resolved in the poli-OCT data with the PT laser on (Fig. 5.6b). The high concentration of injected ICG (500 μg/ml) is similar to previous fluorescence based studies [31, 32] making the poli-OCT signal extremely bright. The network structure of the lymphatics is more evident when visualizing the *en face* average intensity projection of the image volume (Fig. 5.6c, 6d). With the PT laser off, the background signal (green, Fig. 5.6c) overlaps only with the location of blood vessels identified by speckle variance OCT (red, Fig. 5.6c), as predicted by results found in Fig. 5.5. With the PT laser on, the poli-OCT signal identifies the lymphatic vascular networks removing ICG from the intradermal injection site towards the base of the ear (green, Fig. 5.6d). The green circular feature at the bottom of Fig. 5.6d corresponds to a surface leak of the ICG near the injection site.

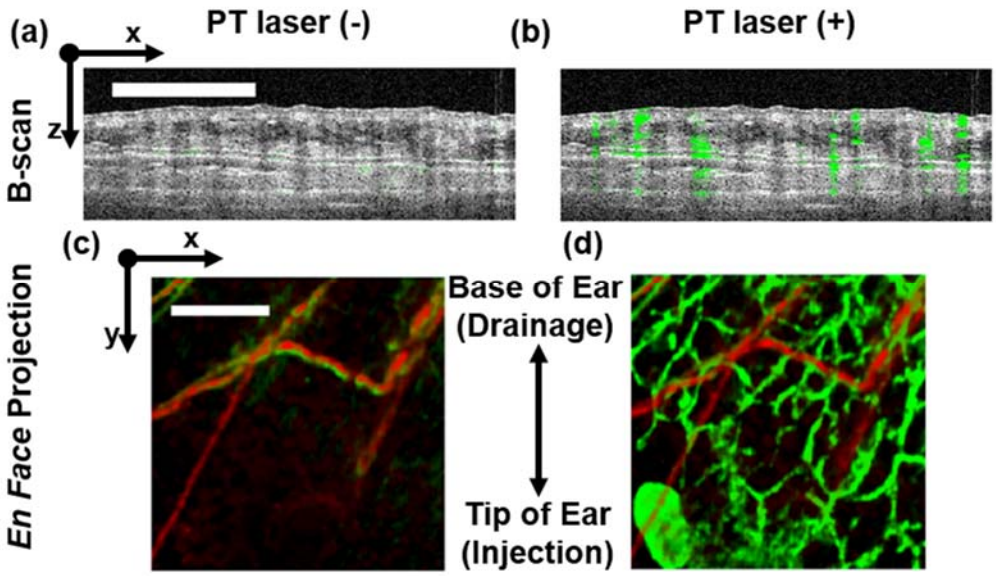

Fig. 5.6. *In vivo* poli-OCT of mouse ear lymphatics using ICG as a contrast agent. 3D image volumes were acquired of a mouse ear after intradermal injection of ICG. Representative B-scans containing tissue morphology (gray) and poli-OCT signal (green) with the PT laser (a) off and (b) on. (c) *En face* projections of the volume including the vasculature (red, speckle variance OCT) shows minimal extravascular poli-OCT signal (green) with the PT laser off. (d) With the PT laser on, the poli-OCT signal (green) increases in locations where the lymphatic vessels are draining ICG from the injection site. Scale bar = 1 mm.

To demonstrate the breadth of potential imaging contrast agents for poli-OCT, gold nanorods were also imaged *in vivo* at 10 times faster frame rates than previously reported for *in vivo* imaging of similar concentrations of gold nanorods using traditional PTOCT [11]. Injections of either Matrigel alone or Matrigel with 200 pM of gold nanorods were imaged over 2.5 mm by 2.5 mm volumes with poli-OCT (green, Fig. 5.7). Overlapping speckle variance OCT scans identified the locations of blood vessels (red, Fig. 5.7). After injection of Matrigel alone into the mouse ear, *en face* average intensity projections revealed no significant extra-vascular poli-OCT signal with either the PT Laser off (Fig. 5.7a) or the PT Laser on (Fig. 5.7b). Additionally, after gold nanorod injections into the mouse ear, there were no extra-vascular regions of poli-OCT signal with the PT Laser off (Fig. 5.7c). However, a significantly enhanced poli-OCT signal was present in the region surrounding the site of gold nanorod-loaded Matrigel injection (Fig. 5.7d). Unlike the ICG lymphatic imaging (Fig. 5.6), the gold nanorods remained localized near the injection site due to

the solidification of the Matrigel at body temperature.

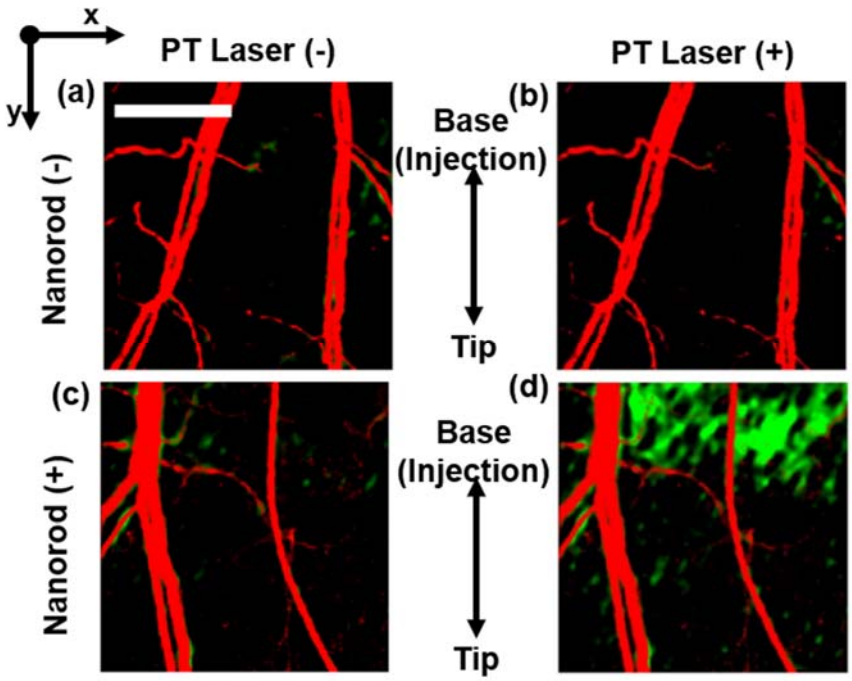

Fig. 5.7. *In vivo* poli-OCT imaging of subcutaneous injections of gold nanorods in two mice. 3D image volumes were acquired of a mouse ear after injection of Matrigel alone (top) or Matrigel plus 200 pM gold nanorods (bottom). *En face* average intensity projections contain the poli-OCT signal (green) and speckle variance OCT signal (red). With Matrigel alone, no poli-OCT signal is observed (a) without or (b) with the PT laser. (c) In the presence of gold nanorods, no extra-vascular poli-OCT signal is present without the PT laser. (d) Only with gold nanorods and the PT laser on, is there an observable poli-OCT signal. Scale bar = 1 mm.

5.5 Discussion

We have incorporated optical lock-in methods into traditional PTOCT, and for the first time demonstrated *in vivo* poli-OCT. The poli-OCT system and signal was characterized while imaging tissue-mimicking phantoms containing an FDA-approved small molecule fluorophore (ICG). We also assessed how motion artifact and blood flow, confounding factors unique to i*n vivo* imaging, affect the background signal in poli-OCT. Finally, two contrast agents were imaged *in vivo*, demonstrating the versatility of poli-OCT for use with small molecule and nanoparticle contrast agents. The ability to image fluorophores common to molecular imaging [34] as well as gold nanoparticles under development for molecular imaging and drug delivery [35] demonstrates the breadth of potential poli-OCT applications. Given the improvements enabled by poli-OCT, the

unique spatial imaging niche of OCT, and the range of potential contrast agents available for imaging, the optical lock-in techniques demonstrated in these studies could enable more widespread adoption of photothermal OCT for *in vivo* imaging.

In this study, poli-OCT was used to identify gold nanorods in real time at ten times faster frame rates and with 1000 times less digital data acquisition than a previous PTOCT study (Fig. 5.7 and [11]). The previous PTOCT study from our group imaged 400 pM gold nanorods subcutaneously injected into the mouse ear (2X higher concentration than the current study) using 200 Hz photothermal laser modulation frequency, 3.2 kW/cm^2 average irradiance, and 100 ms observation time at each A-scan position. In the current study, a photothermal modulation frequency of 500 Hz was used to avoid background signal contribution (Fig. 5.5d), and the average irradiance was increased to 15.5 kW/cm^2 to account for the signal decrease at faster modulation frequencies (Fig. 5.3a). Even with increased irradiance, the tenfold increase in poli-OCT imaging speed reduced the total radiant exposure at each A-scan position by a factor of two, from 320 J/cm^2 in the previous PTOCT study [11] to 155 J/cm^2 in the current poli-OCT study. To better understand the impact of these advances for *in vivo* imaging studies, scan length times and data burden were calculated and compared for poli-OCT and traditional PTOCT [11], assuming 1024 pixels per A-scan saved as 16 bit unsigned integers. For each A-scan position, poli-OCT acquired one A-scan over 10 ms, while a previously reported traditional PTOCT system acquired 1000 A-scans over 100 ms [11]. For a study including 10 mice imaged over a 300 by 300 rectangular scan volume repeated at five time points, the previously reported PTOCT system would require 7500 minutes (125 hours) and 9.2 TB of data acquisition, while poli-OCT would require only 750 total minutes (12.5 hours) and 9.2 GB of data acquisition. Thus, poli-OCT provides more streamlined *in vivo* time-course studies than previously reported PTOCT systems. GPU processing [36] could also be used to mitigate the data acquisition and offline signal analysis burden of traditional PTOCT, and offers reduced optical

complexity compared to poli-OCT. However, previous publications that implement the optical lock-in detection scheme used in poli-OCT have suggested significant SNR improvements over digital sampling of phase modulations [20], an advantage that GPU processing of traditional PTOCT data does not provide. Nevertheless, this paper demonstrates the first real time *in vivo* PTOCT images, at increased frame rates compared to previous publications that use traditional PTOCT to image similar samples [11, 17].

While this work demonstrates improvements of poli-OCT with respect to traditional PTOCT, the current poli-OCT design includes a few addressable shortcomings. The technical advancement from traditional PTOCT to poli-OCT has increased the complexity of the optical instrumentation. For example, the use of three AOMs to control the reference arm frequency shift (Ω_R) and photothermal laser intensity modulation (Ω_P) increases the cost and complexity over traditional PTOCT. AOMs are attractive for this application because they provide both frequency shifting and amplitude modulation, can be phase and frequency locked to each other, and supply a wide range of frequencies. However, as demonstrated in Fig. 5.4a, precise frequency matching of Ω_P and Ω_R may not be required for poli-OCT, so approaches that are less precise but more cost effective than AOMs could be implemented (e.g. moving reference arm [37], offset scanning reference mirror [38]). An additional source of poli-OCT imaging system complexity is the one way optical paths in both the reference and sample arms, which are used to reduce unwanted back-reflections acquired during long CCD acquisition times. Long CCD acquisition times are governed by the photothermal laser modulation frequency (Ω_P), which is slow due to the inverse relationship between photothermal signal magnitude and photothermal laser modulation frequency (Fig. 5.3b and [11]). Furthermore, for *in vivo* poli-OCT, focusing optics with a larger depth of focus and correspondingly larger spot sizes than microscopy are desirable. These larger spot sizes require slower photothermal modulation frequencies (e.g. hundreds of Hz) than photothermal microscopy

for optimal performance [18, 39]. Photothermal modulation frequencies (Ω_P) in the hundreds of Hz regime require millisecond CCD integration times (e.g. if $\Omega_R = \Omega_P = 500$ Hz, $\tau \geq 2$ ms). One-way optical paths help to reduce unwanted back-reflections that can consume a large portion of the CCD dynamic range at these long integration times.

In comparison to traditional PTOCT and OCT, poli-OCT requires additional unique considerations. First, the contribution of certain image signals is greatly enhanced in poli-OCT images compared to OCT. The poli-OCT cross-correlation signal due to photothermal heating is an attenuated version of the original OCT cross-correlation signal. However, the poli-OCT autocorrelation signal is not frequency shifted and therefore not attenuated compared to the original OCT image. Consequently, the intensity of the autocorrelation signal relative to the cross-correlation signal is large for poli-OCT compared to traditional PTOCT or OCT. In this work, the poli-OCT autocorrelation signal was attenuated using cross-polarized sample arm light that limited surface specular reflections [40-42]. Furthermore, the autocorrelation image remains largely unchanged with or without the PT laser, and therefore subtracting an image with the PT laser off from an image with the PT laser on can help minimize the autocorrelation signal and generate images with minimal artifact. Note that this was not required for these *in vivo* imaging applications (Fig. 5.6 and Fig. 5.7). In addition to the autocorrelation signal effects, the poli-OCT signal depends on the reflectivity of the sample and reference arms (Eq. 1) [19]. Therefore, variations in image parameters or tissue optical properties can affect images taken on different days or between samples. Dividing the poli-OCT image by the OCT image (Ω_R=0) can account for day-to-day inter-sample and intra-sample variations in reflectivity, and aid in maximizing contrast in the poli-OCT signal. If OCT images are desired in addition to poli-OCT images, an OCT scan must be acquired separately from the poli-OCT scan. However, the OCT data can be captured at significantly faster integration times than poli-OCT, thus minimally affecting overall acquisition time. A remaining

consideration is phase accumulation, or the integration of the PTOCT signal with depth [43]. Unlike traditional PTOCT, the poli-OCT signal is also a function of the OCT signal magnitude (Eq. 1). Therefore, phase accumulation does occur, but the signal first increases with depth due to phase accumulation then decreases with depth due to OCT signal falloff (data not shown). Algorithms are currently under development to address this issue.

In conclusion, for the first time, we have demonstrated *in vivo* poli-OCT for real time imaging of both small molecules and gold nanoparticles. Using poli-OCT, PTOCT data can be acquired faster, with orders of magnitude less data burden, and real time signal analysis. Mitigating the slow acquisition and high data burden of traditional PTOCT gives poli-OCT the potential to significantly impact preclinical *in vivo* molecular imaging. Higher volume acquisition rates and real time display of photothermal images could enable *in vivo* PTOCT applications that are not feasible with traditional PTOCT, such as time-course tomograms of small molecule drug delivery [4]. In addition, poli-OCT is attractive for other applications where the high resolution, wide field of view, and accompanying label-free imaging of tissue and vessel morphology provide significant advantages over traditional imaging techniques. Potential applications are numerous: molecular imaging in mammary, dorsal, abdominal, and cranial window models of cancer [34]; noninvasive imaging of drug delivery kinetics to assess the impact of drug vector size [44, 45], surface chemistry [46], and shape [47]; imaging drug clearance [48]; and imaging local drug diffusion and release [49, 50]. Overall, by leveraging the existing high resolution and wide field of view of OCT as well as its abilities to image tissue and vessel morphology, poli-OCT holds significant promise in studies of drug discovery and drug delivery, molecular imaging, and biological studies of pathogenesis.

5.6 Acknowledgements

This work was supported by grants from the National Institutes of Health under award numbers

R00CA142888 and R25CA136440. The authors would like to thank Kelsey R. Beavers and Dr. Craig L. Duvall for supplying gold nanorods.

5.7 References

1. M. de Jong, J. Essers, and W. M. van Weerden, "Imaging preclinical tumour models: improving translational power," Nature Reviews Cancer **14**, 481-493 (2014).

2. J. K. Willmann, N. van Bruggen, L. M. Dinkelborg, and S. S. Gambhir, "Molecular imaging in drug development," Nat Rev Drug Discov **7**, 591-607 (2008).

3. A. J. Walsh, R. S. Cook, H. C. Manning, D. J. Hicks, A. Lafontant, C. L. Arteaga, and M. C. Skala, "Optical Metabolic Imaging Identifies Glycolytic Levels, Subtypes, and Early-Treatment Response in Breast Cancer," Cancer research **73**, 6164-6174 (2013).

4. G. M. Thurber, K. S. Yang, T. Reiner, R. H. Kohler, P. Sorger, T. Mitchison, and R. Weissleder, "Single-cell and subcellular pharmacokinetic imaging allows insight into drug action in vivo," Nat Commun **4**(2013).

5. W. Drexler and J. G. Fujimoto, *Optical Coherence Tomography: Technology and Applications* (Springer, 2008).

6. T. Klein, W. Wieser, L. Reznicek, A. Neubauer, A. Kampik, and R. Huber, "Multi-MHz retinal OCT," Biomedical optics express **4**, 1890-1908 (2013).

7. A. Mariampillai, B. A. Standish, E. H. Moriyama, M. Khurana, N. R. Munce, M. K. K. Leung, J. Jiang, A. Cable, B. C. Wilson, I. A. Vitkin, and V. X. D. Yang, "Speckle variance detection of microvasculature using swept-source optical coherence tomography," Optics letters **33**, 1530-1532 (2008).

8. G. J. Liu, A. J. Lin, B. J. Tromberg, and Z. P. Chen, "A comparison of Doppler optical coherence tomography methods," Biomedical optics express **3**, 2669-2680 (2012).

9. M. C. Skala, M. J. Crow, A. Wax, and J. A. Izatt, "Photothermal optical coherence tomography of epidermal growth factor receptor in live cells using immunotargeted gold nanospheres," Nano letters **8**, 3461-3467 (2008).

10. D. C. Adler, S. W. Huang, R. Huber, and J. G. Fujimoto, "Photothermal detection of gold nanoparticles using phase-sensitive optical coherence tomography," Optics express **16**, 4376-4393 (2008).

11. J. M. Tucker-Schwartz, T. A. Meyer, C. A. Patil, C. L. Duvall, and M. C. Skala, "In vivo photothermal optical coherence tomography of gold nanorod contrast agents," Biomedical optics express **3**, 2881-2895 (2012).

12. Y. Jung, R. Reif, Y. Zeng, and R. K. Wang, "Three-dimensional high-resolution imaging of gold nanorods uptake in sentinel lymph nodes," Nano letters **11**, 2938-2943 (2011).

13. C. Zhou, T. H. Tsai, D. C. Adler, H. C. Lee, D. W. Cohen, A. Mondelblatt, Y. Wang, J. L. Connolly, and J. G. Fujimoto, "Photothermal optical coherence tomography in ex vivo human breast tissues using gold nanoshells," Optics letters **35**, 700-702 (2010).

14. A. Nahas, M. Varna, E. Fort, and A. C. Boccara, "Detection of plasmonic nanoparticles with full field-OCT: optical and photothermal detection," Biomedical optics express **5**, 3541-3546 (2014).

15. J. M. Tucker-Schwartz, T. Hong, D. C. Colvin, Y. Xu, and M. C. Skala, "Dual-modality photothermal optical coherence tomography and magnetic-resonance imaging of carbon nanotubes," Optics letters **37**, 872-874 (2012).

16. B. Yin, R. V. Kuranov, A. B. McElroy, S. Kazmi, A. K. Dunn, T. Q. Duong, and T. E. Milner, "Dual-wavelength photothermal optical coherence tomography for imaging microvasculature blood oxygen saturation," Journal of biomedical optics **18**, 56005 (2013).

17. J. M. Tucker-Schwartz, K. R. Beavers, W. W. Sit, A. T. Shah, C. L. Duvall, and M. C. Skala, "In vivo imaging of nanoparticle delivery and tumor microvasculature with multimodal optical coherence tomography," Biomedical optics express **5**, 1731-1743 (2014).

18. L. Cognet, C. Tardin, D. Boyer, D. Choquet, P. Tamarat, and B. Lounis, "Single metallic nanoparticle imaging for protein detection in cells," Proceedings of the National Academy of Sciences of the United States of America **100**, 11350-11355 (2003).

19. C. Pache, N. L. Bocchio, A. Bouwens, M. Villiger, C. Berclaz, J. Goulley, M. I. Gibson, C. Santschi, and T. Lasser, "Fast three-dimensional imaging of gold nanoparticles in living cells with photothermal optical lock-in Optical Coherence Microscopy," Optics express **20**, 21385-21399 (2012).

20. W. J. Eldridge, A. Meiri, A. Sheinfeld, M. T. Rinehart, and A. Wax, "Fast wide-field photothermal and quantitative phase cell imaging with optical lock-in detection," Biomedical optics express **5**, 2517-2526 (2014).

21. M. Wojtkowski, V. J. Srinivasan, T. H. Ko, J. G. Fujimoto, A. Kowalczyk, and J. S. Duker, "Ultrahigh-resolution, high-speed, Fourier domain optical coherence tomography and methods for dispersion compensation," Optics express **12**, 2404-2422 (2004).

22. S. Moon, S. W. Lee, and Z. P. Chen, "Reference spectrum extraction and fixed-pattern noise removal in optical coherence tomography," Optics express **18**, 24395-24404 (2010).

23. A. Oldenburg, F. Toublan, K. Suslick, A. Wei, and S. Boppart, "Magnetomotive contrast for in vivo optical coherence tomography," Optics express **13**, 6597-6614 (2005).

24. R. Leitgeb, C. K. Hitzenberger, and A. F. Fercher, "Performance of fourier domain vs. time domain optical coherence tomography," Optics express **11**, 889-894 (2003).

25. M. J. C. vanGemert, G. W. Lucassen, and A. J. Welch, "Time constants in thermal laser

medicine .2. Distributions of time constants and thermal relaxation of tissue," Phys Med Biol **41**, 1381-1399 (1996).

26. T. Hoshida, N. Isaka, J. Hagendoorn, E. di Tomaso, Y. L. Chen, B. Pytowski, D. Fukumura, T. P. Padera, and R. K. Jain, "Imaging steps of lymphatic metastasis reveals that vascular endothelial growth factor-C increases metastasis by increasing delivery of cancer cells to lymph nodes: therapeutic implications," Cancer research **66**, 8065-8075 (2006).

27. J. L. Li, C. C. Goh, J. L. Keeble, J. S. Qin, B. Roediger, R. Jain, Y. L. Wang, W. K. Chew, W. Weninger, and L. G. Ng, "Intravital multiphoton imaging of immune responses in the mouse ear skin," Nat Protoc **7**, 221-234 (2012).

28. W. W. Kilarski, E. Guc, J. C. M. Teo, S. R. Oliver, A. W. Lund, and M. A. Swartz, "Intravital Immunofluorescence for Visualizing the Microcirculatory and Immune Microenvironments in the Mouse Ear Dermis," Plos One **8**(2013).

29. S. Yousefi, J. Qin, Z. Zhi, and R. K. Wang, "Label-free optical lymphangiography: development of an automatic segmentation method applied to optical coherence tomography to visualize lymphatic vessels using Hessian filters," Journal of biomedical optics **18**, 86004 (2013).

30. N. L. Harvey, R. S. Srinivasan, M. E. Dillard, N. C. Johnson, M. H. Witte, K. Boyd, M. W. Sleeman, and G. Oliver, "Lymphatic vascular defects promoted by Prox1 haploinsufficiency cause adult-onset obesity," Nat Genet **37**, 1072-1081 (2005).

31. S. Kwon, G. D. Agollah, W. Y. Chan, and E. M. Sevick-Muraca, "Altered lymphatic function and architecture in salt-induced hypertension assessed by near-infrared fluorescence imaging," Journal of biomedical optics **17**(2012).

32. S. Kwon and E. M. Sevick-Muraca, "Mouse phenotyping with near-infrared fluorescence lymphatic imaging," Biomedical optics express **2**, 1403-1411 (2011).

33. C. V. Pastuskovas, E. E. Mundo, S. P. Williams, T. K. Nayak, J. Ho, S. Ulufatu, S. Clark, S. Ross, E. Cheng, K. Parsons-Reponte, G. Cain, M. Van Hoy, N. Majidy, S. Bheddah, J. dela Cruz Chuh, K. R. Kozak, N. Lewin-Koh, P. Nauka, D. Bumbaca, M. Sliwkowski, J. Tibbitts, F. P. Theil, P. J. Fielder, L. A. Khawli, and C. A. Boswell, "Effects of anti-VEGF on pharmacokinetics, biodistribution, and tumor penetration of trastuzumab in a preclinical breast cancer model," Molecular cancer therapeutics **11**, 752-762 (2012).

34. S. I. J. Ellenbroek and J. van Rheenen, "Imaging hallmarks of cancer in living mice," Nature Reviews Cancer **14**, 406-418 (2014).

35. E. C. Dreaden, L. A. Austin, M. A. Mackey, and M. A. El-Sayed, "Size matters: gold nanoparticles in targeted cancer drug delivery," Therapeutic delivery **3**, 457-478 (2012).

36. H. Y. Lee, P. D. Raphael, J. Park, A. K. Ellerbee, B. E. Applegate, and J. S. Oghalai, "Noninvasive in vivo imaging reveals differences between tectorial membrane and basilar membrane traveling waves in the mouse cochlea," Proceedings of the National Academy of

Sciences of the United States of America **112**, 3128-3133 (2015).

37. R. K. K. Wang, "In vivo full range complex Fourier domain optical coherence tomography," Appl Phys Lett **90**(2007).

38. M. Szkulmowski, I. Grulkowski, D. Szlag, A. Szkulmowska, A. Kowalczyk, and M. Wojtkowski, "Flow velocity estimation by complex ambiguity free joint Spectral and Time domain Optical Coherence Tomography," Optics express **17**, 14281-14297 (2009).

39. D. Boyer, P. Tamarat, A. Maali, B. Lounis, and M. Orrit, "Photothermal imaging of nanometer-sized metal particles among scatterers," Science **297**, 1160-1163 (2002).

40. J. M. Schmitt and S. H. Xiang, "Cross-polarized backscatter in optical coherence tomography of biological tissue," Optics letters **23**, 1060-1062 (1998).

41. P. Lenton, J. Rudney, R. Q. Chen, A. Fok, C. Aparicio, and R. S. Jones, "Imaging in vivo secondary caries and ex vivo dental biofilms using cross-polarization optical coherence tomography," Dent Mater **28**, 792-800 (2012).

42. R. S. Jones and D. Fried, "Remineralization of enamel caries can decrease optical reflectivity," J Dent Res **85**, 804-808 (2006).

43. G. Guan, R. Reif, Z. Huang, and R. K. Wang, "Depth profiling of photothermal compound concentrations using phase sensitive optical coherence tomography," Journal of biomedical optics **16**, 126003 (2011).

44. S. D. Perrault, C. Walkey, T. Jennings, H. C. Fischer, and W. C. W. Chan, "Mediating Tumor Targeting Efficiency of Nanoparticles Through Design," Nano letters **9**, 1909-1915 (2009).

45. L. Tang, T. M. Fan, L. B. Borst, and J. J. Cheng, "Synthesis and Biological Response of Size-Specific, Monodisperse Drug-Silica Nanoconjugates," Acs Nano **6**, 3954-3966 (2012).

46. Y. Akiyama, T. Mori, Y. Katayama, and T. Niidome, "The effects of PEG grafting level and injection dose on gold nanorod biodistribution in the tumor-bearing mice," J Control Release **139**, 81-84 (2009).

47. Arnida, M. M. Janat-Amsbury, A. Ray, C. M. Peterson, and H. Ghandehari, "Geometry and surface characteristics of gold nanoparticles influence their biodistribution and uptake by macrophages," Eur J Pharm Biopharm **77**, 417-423 (2011).

48. S. W. Jones, R. A. Roberts, G. R. Robbins, J. L. Perry, M. P. Kai, K. Chen, T. Bo, M. E. Napier, J. P. Y. Ting, J. M. DeSimone, and J. E. Bear, "Nanoparticle clearance is governed by Th1/Th2 immunity and strain background," J Clin Invest **123**, 3061-3073 (2013).

49. K. M. Poole, C. E. Nelson, R. V. Joshi, J. R. Martin, M. K. Gupta, S. C. Haws, T. E. Kavanaugh, M. C. Skala, and C. L. Duvall, "ROS-responsive microspheres for on demand antioxidant therapy in a model of diabetic peripheral arterial disease," Biomaterials **41**, 166-175 (2015).

50. C. E. Nelson, A. J. Kim, E. J. Adolph, M. K. Gupta, F. Yu, K. M. Hocking, J. M. Davidson, S. A. Guelcher, and C. L. Duvall, "Tunable delivery of siRNA from a biodegradable scaffold to promote angiogenesis in vivo," Advanced materials **26**, 607-614, 506 (2014).

CHAPTER 6

Conclusions and Future Directions

6.1 Summary and Conclusions

This dissertation represents anadvancement in molecular and functional imaging of cancer and allows researchers to image previously unexplored spatial regimes non-destructively. Current *in vivo* molecular imaging techniques are either high resolution with limited penetration depth or low resolution with deep sample penetration. PTOCT allows for imaging of contrast agents alongside other powerful functional extensions of OCT (microvessel structure, flow dynamics, tissue viability) at depths greater than microscopy (>1 mm) and at higher resolution than photoacoustic tomography; these metrics correspond to a key spatial regime for studying heterogeneities in cancer. This gives researchers an opportunity to relate molecular expression and drug delivery as a function of space and time to vascular remodeling and morphological transitions in microstructure, all of which are critical features during cancer drug discovery and for studies of pathogenesis. These endpoints are all visualized with deep and wide field of view optical imaging at a resolution that can identify cellular level spatial heterogeneities as well as microvessels. The potential of PTOCT for *in vivo* imaging applications has been demonstrated over three Specific Aims of work, encompassing four publications [1-4]. This work has demonstrated that PTOCT is sensitive to three different classes of contrast agents at concentrations relevant to *in vivo* imaging. Gold nanorods and fluorophores were both localized from within living mice, and the heterogeneous accumulation and distribution of gold nanorods into tumors was spatially tracked over time in multiple mice. Prior to this work, no group had demonstrated the use of PTOCT for *in vivo* imaging, making this research the benchmark for future *in vivo* studies using PTOCT.

Chapter 3 addresses Aim 1, laying the technical groundwork for *in vivo* imaging of contrast agents with PTOCT, and demonstrating pMsensitivity of PTOCT to gold nanorods, a highly

absorbing nanoparticle under development for molecular imaging [5] and drug delivery [6] applications in cancer. Prior to pursuing PTOCT imaging applications involving complex *in vivo* systems, it is important to characterize and optimize the imaging system in more controlled environments. Therefore, we characterized the photothermal signal using the bio-heat conduction equation [7], and directly compared modeled and experimental PTOCT data. The PTOCT signal closely matched theory and demonstrated appropriate sensitivity to gold nanorods for *in vivo* imaging of systemically delivered gold nanorods in mouse tumors [8]. In addition, pM concentrations of gold nanorods were successfully identified from within phantoms as well as *in vivo*, demonstrating a key first step towards sensitive *in vivo* imaging of gold nanorods using PTOCT. We demonstrated that PTOCT can image gold nanorods at depths approaching 1 mm *in vivo*, exceeding the *in vivo* imaging depths of traditional high resolution microscopy (including two-photon), while additionally supplying co-registered tissue and vessel features. In conclusion, Chapter 3 reports the technical insight required for *in vivo* PTOCT imaging and demonstrates the early promise of PTOCT for sensitive and specific imaging of contrast agents with an impressive combination of spatial resolution and imaging depth.

In Chapter 4, the use of PTOCT in more complex *in vivo* systems is demonstrated, and the potential of the imaging tool is showcased by imaging heterogeneities in the delivery of nanoparticles to tumors. Solid tumors contain pores in their newly formed microvasculature as well as an impaired lymphatic system that allow nano-sized particles to enter into and avoid clearance from the tumor tissue [9, 10]. These factors combined allow for significant uptake of nanoscale drugs into tumors and is the basis for a number of drug delivery strategies under development [11-14]. However, heterogeneities in the severely abnormal microenvironment cause regions of high interstitial fluid pressure, dense stroma, and other factors that physically constrain the delivery of these nanoscale particles throughout the tumor tissue [15, 16]. In Chapter 4 we have shown that *in*

vivo PTOCT can track the time-dependent spatial heterogeneities of nanoparticle delivery and uptake to a solid tumor alongside tissue structure using OCT and vessel morphology using SVOCT. In multiple mice bearing mammary tumors in a dorsal window chamber, PTOCT identified gold nanorod accumulation into the mouse tumors and was also able to characterize the spatial frequency dynamics of nanorod delivery as a function of time. The combined abilities of OCT, SVOCT, and PTOCT to capture co-registered images of tissue structure, vessel morphology, and contrast agent distribution could allow for more comprehensive analyses of drug delivery kinetics in tumors at high resolution, over a wide field of view, and deeper than microscopy techniques. This makes PTOCT part of a very attractive imaging tool for studying *in vivo* heterogeneities in drug delivery, molecular expression, and treatment response in cancer.

In Chapter 5, we attempted to increase the throughput of PTOCT and allow for real-time imaging by replacing offline digital frequency analysis with optical lock-in techniques. In addition, sensitivity to small molecule fluorophores was established, a class of contrast agents that are much smaller than their nanoparticle counterparts and thus allow for more broad biomedical applications. Optical lock-in was incorporated into the PTOCT system to create a poli-OCT imaging system. At the long integration times required for poli-OCT, the system displayed shot noise-limited performance, and the poli-OCT signal followed similar trends in photothermal signal strength compared to traditional PTOCT. Additionally, poli-OCT was able to identify ICG, an FDA-approved near infrared fluorophore, at concentrations relevant to those found in tumors after systemic delivery. The unique considerations of *in vivo* imaging with poli-OCT were explored and two examples of *in vivo* imaging were performed. First, lymphatics from within a mouse ear were identified after injection of ICG into the tissue. Lymphatics are an essential component of cancer; injection and imaging of dyes is commonly used to better characterize the impact of lymphatics on tumor development [17]. Second, similar to Chapter 3, subcutaneous injections of picomolar

concentrations of gold nanorods were identified using poli-OCT, although with poli-OCT all data was collected and displayed in real time at ten times faster scan rates compared to previously published PTOCT work. The work in Chapter 5 is the first to demonstrate *in vivo* imaging using photothermal optical lock-in techniques, and the first to demonstrate the potential of fluorophores for PTOCT imaging. The ability to image both fluorophores commonly used in molecular imaging [18] as well as gold nanoparticles under development for molecular imaging and drug delivery [6] demonstrates the breadth of potential poli-OCT applications.

Ultimately, the work in this dissertation has laid the technical groundwork for PTOCT as an *in vivo* imaging tool. The high resolution and deep imaging penetration of PTOCT makes it particularly unique. Additionally, the sensitivity to a range of contrast agents, as demonstrated in this dissertation, makes PTOCT broadly applicable in the research and drug development setting. The combination of PTOCT with OCT and SVOCT could allow for unique datasets for analysis of drug delivery, molecular imaging, and treatment response.

6.2 Future Directions

Future opportunities following the work in this dissertation can be separated into two distinct groups, technical improvements to PTOCT and biological studies that are immediately feasible and potentially impactful.

6.2.1 Potential Technical Improvements

Model-Based Optimization of PTOCT

As shown in Chapters 3 and 5, there are a number of PTOCT imaging parameters a user needs to optimize based on the selected *in vivo* application. However, not only are PTOCT imaging parameters important, the parameters of the OCT imaging system itself also impact the SNR of the PTOCT [3] and poli-OCT signal [4]. OCT imaging parameters including wavelength, integration time, and laser power all impact the SNR of the OCT image as a function of depth and tissue type

and, in turn, impact the SNR of the PTOCT signal. For example, imaging at 1310 nm as opposed to 860 nm as used in this dissertation could allow for deeper PTOCT imaging in tissue via the increased penetration depth of the OCT signal. Complete analytical models of the PTOCT signal as a function of OCT, PTOCT, and tissue parameters could aid researchers in optimization of their imaging systems or decisions in purchasing commercial systems based on the desired application. Currently, the imaging system parameters have been selected to match the imaging application using experimental validation. However, this optimization process could be more thoroughly undertaken and at a more rapid pace with the help of analytical signal models.

Phase Accumulation

Phase accumulation is an artifact in the axial dimension of the PTOCT image that impacts the accuracy of the system in the depth dimension [19]. In vessel imaging applications using OCT, artifacts in the depth dimension are attenuated using an exponential decay during post-processing [20]. However, this solution involves application of an arbitrary decay constant. In one previous publication, phase accumulation in PTOCT was addressed with a spatially averaged derivative operation [19]. This method relies on a number of assumptions, was only tested in fairly homogenous phantoms, and in our experience causes significant image artifacts in the absence of extensive signal averaging. Therefore, there is an opportunity to address phase accumulation in heterogenous tissues containing sparse PTOCT signals. Accurately accounting for phase accumulation is essential to ensure accuracy of PTOCT in the depth dimension and truly allow for high resolution imaging in all three dimensions. Models such as those suggested in the above section could potentially be used to account for phase accumulation.

Comparing PTOCT to Competing Technologies

Photoacoustic microscopy is currently under rapid development and able to achieve resolution and penetration depths on a similar scale to PTOCT. However, photoacoustic microscopy requires

direct contact with the sample and the incorporation of both optical and ultrasonic instrumentation. A direct comparison between PTOCT and photoacoustic microscopy with respect to cost, sensitivity, and imaging speed could be an important contribution to the field of molecular imaging and determine where each relative imaging tool could be improved. A complete analytical PTOCT model as proposed above could allow for both theoretical and matching experimental comparisons of the two systems.

Simultaneous Estimation of poli-OCT Background Signal

One strength of traditional PTOCT over the current implementation of poli-OCT is the ability to estimate the background signal (i.e. the signal without the photothermal laser) from one dataset. Poli-OCT does not allow for simultaneous estimates of the background signal, although spatial filtering does manage to attenuate a bulk of those artifacts *in vivo* (Chapter 5). An implementation of poli-OCT that allows for simultaneous estimates of the signal with and without the photothermal laser from the same dataset could greatly attenuate background signal artifacts *in vivo*. In Doppler OCT, quantitative flow metrics can be estimated by simultaneous imaging of multiple optical paths with the introduction of optical delays into the sample arm [21]. Achieving these optical delays requires only the addition of a transparent glass sample of known thickness to a portion of the sample arm light path. Incorporating color filters into the optical delay lines could potentially allow for the simultaneous acquisition of the sample signal both with and without the photothermal laser.

6.2.2 Preclinical Applications of PTOCT

Effect of Nanoparticle Size and Shape on Intra-Tumoral Delivery

As demonstrated in Chapter 4, nonspecific accumulation and delivery of nanorods is spatially heterogeneous. Nanoparticles of varying size, shape, and surface functionalization are under heavy development for cancer treatment through photothermal and drug-induced therapy pathways [6, 22-25]. However, optimal treatment affect requires a therapeutic drug dose throughout the entire solid

tumor, a difficult task considering the barriers to homogeneous drug delivery in cancer [16, 26, 27]. Therefore, researchers have developed a number of nanoparticle shapes and sizes, each with a particular strength. Gold nanoparticles are an especially attractive version of these nanoparticle solutions currently in human clinical trials, with nanoshells [11], nanorods [28], nanocages [29], and nanostars [30] among other shapes under development in the research community, and all of which can be imaged with PTOCT. A thorough analysis of the spatial heterogeneities in drug delivery over time as a function of nanoparticle size and shape would be a particularly impactful method for drug delivery optimization before these particles are considered for clinical research. A study similar to that found in Chapter 4 would allow researchers to noninvasively assess the delivery and clearance kinetics of both drug-loaded and blank nanoparticles of varying size and shape and compare their delivery kinetics to the vessel morphology and tumor viability, all with the same imaging tool. Also, limitations in tumor penetration into the tissue could be quantified by assessing nanoparticle diffusion distances from the delivery source (i.e. microvessels). Previous examples of this type of study can be found in the literature but most often using invasive methods to characterize bulk drug delivery metrics [23] or with invasive microscopy methods [31] that are depth-limited and do not supply the additional information unique to OCT (vessel morphology, tissue structure/viability). PTOCT could be used to supply the spatial and temporal dynamics of these different nanoparticles and aid in the development and optimization of novel drug delivery treatments.

Effect of Surface Functionalization on Nanoparticle Delivery

Nanoparticles have been proposed both as drug delivery agents of molecular-targeted drugs and as molecular imaging contrast agents. However, molecular imaging of non-vascular tissue targets is a challenge in tumors due to the nonspecific uptake and reduced clearance of all nanoparticles of a specific size, regardless of surface functionalization. While some research groups have identified significant differences in the kinetics of molecularly-targeted versus blank nanoparticle controls [32],

others have identified no differences between the two [33, 34]. PTOCT can noninvasively track contrast agent delivery to tumors in the context of tissue and vessel morphology with high resolution at depths greater than microscopy and could, therefore, be used to better understand the role of surface functionalization on contrast agent pharmacokinetics and drug delivery in cancer.

6.3 Contribution to the Field and Societal Impact

Contribution to Biophotonics

The studies in this dissertation have led to several contributions in the field of biophotonics including the first demonstrated use of PTOCT to image contrast agents *in vivo*. We characterized the PTOCT signal to understand the basics of system optimization and implemented PTOCT for *in vivo* imaging of nanoparticle uptake over multiple time points in a mouse model of cancer. While many molecular and functional extensions of OCT are relatively insensitive to contrast agents, we demonstrated pM sensitivity to gold nanoparticles and the ability to image trace concentrations *in vivo* after systemic delivery. This is beyond what others had demonstrated previously with PTOCT, making this work the benchmark for future *in vivo* imaging studies using PTOCT. In addition to gold nanorods, we demonstrated sensitivity to small molecule fluorophores and carbon nanotubes at levels that are physiologically meaningful in tumors after systemic delivery, two molecules that had yet to be established as potential PTOCT contrast agents. The ability to image fluorophores, carbon nanotubes, and gold nanoparticles that are all of unique size and shape allow for an expanded portfolio of potential imaging applications with PTOCT. As part of the PTOCT imaging platform, an automated image analysis algorithm was developed that allowed for supervision-free analysis of the large four dimensional datasets acquired using *in vivo* PTOCT. Considerations for image processing included phase derivatives to bound phase wrapping discontinuities, and automated phase referencing. Finally, this dissertation incorporated optical lock-in techniques to *in vivo* imaging in an attempt to increase throughput and perform imaging in real-time, identified the key points to

successfully construct optical lock-in instrumentation for *in vivo* applications, and, for the first time, demonstrated this technique *in vivo*.

Contributions to Cancer Research

Drug delivery and treatment efficacy in cancer is limited due to a number of factors including physical barriers to treatment delivery as well as heterogeneities in tumor molecular expression and the microenvironment [16, 26, 27, 35]. Simulating these complex interactions is especially difficult in an *in vitro* setting, making *in vivo* imaging essential for the development of new drugs and for understanding cancer pathogenesis [18, 36, 37]. PTOCT can allow for sensitive high resolution imaging in a spatial regime previously unexplored, adding a potentially significant tool to the arsenal of researchers who develop new drug and treatment strategies for cancer.

Specifically in this work, we have demonstrated that PTOCT can identify the spatial heterogeneities in nanoparticle delivery to solid tumors. Nanoparticles are under development for drug delivery and molecular imaging applications and most studies of their intratumoral delivery kinetics *in vivo* involve low resolution or destructive imaging [23, 31, 33, 34, 38]. As demonstrated specifically in Chapter 4, PTOCT identified that the mean signal due to nanoparticle accumulation in tumors followed a similar trend across mice, information that low resolution and destructive modalities could also achieve. However, unlike low resolution imaging modalities, PTOCT was also able to quantify that the dynamics in the spatial frequency did not follow the mean signal, and that each tumor exhibited its own unique spatial pattern of uptake. This information would be lost at lower resolution or from shallow penetrating imaging modalities, and would not be possible to track over time using invasive imaging tools. Noninvasive *in vivo* imaging performed over multiple time points in the same mouse allows for increased statistical power, reducing cost and saving time. For example, statistical differences from the work in Chapter 4 over multiple time points was achieved using only four mice in the experimental group. Finally, tissue and vessel morphology were acquired

in concert to the PTOCT data, supplying additional functional information without the need for additional contrast agents. The combination of these observations could be valuable to those developing new methods of drug delivery or attempting to understand the treatment response of cancer.

Bridging the Gap between Preclinical and Clinical Research

One primary goal of preclinical studies is to assess novel treatment strategies during the drug discovery process. Through preclinical studies of efficacy, candidate drugs can be carefully screened to maximize odds of success before implementation in human clinical trials. In cancer studies in particular, mouse studies can be expensive and time-consuming to undertake due to the large number of mice needed to achieve statistical power with invasive imaging. In addition, the complexities in spatial and temporal heterogeneities in tumors suggests that imaging multiple endpoints over time in the same animal is essential to fully understand treatment response and drug delivery. PTOCT could potentially allow for noninvasive high resolution *in vivo* imaging of drug delivery and molecular status, increasing the statistical power of mouse studies and saving both time and money. In addition, the tissue and vessel imaging capabilities of OCT and SVOCT allow for characterization of treatment affect alongside drug delivery or molecular expression, all in the same animal over time. This information could aid researchers in optimization of novel treatments and better understand how drug combinations impact cancer pathogenesis, allowing for new treatment strategies to reach the clinic faster and more efficiently.

PTOCT could also impact patients and clinical research through *in vivo* imaging of nanoparticle tumor delivery in humans. Gold nanoshells are currently in clinical trials for photothermal therapy treatment of a specific subset of tumors (clinicaltrials.gov identifier NCT00848042 and NCT01679470). After systemic injection of gold nanoshells, the nanoparticles accumulate into the tumor tissue due to the EPR effect, similar to the study presented in Chapter 4. An interstitial FDA

approved fiber-coupled laser source is then inserted directly into the tumor, and near infrared light is used to heat the nanoshells to the point of tumor cell death. Because OCT utilizes low NA optics, OCT instrumentation and, therefore, PTOCT instrumentation can be miniaturized to the scale of endoscopic and needle probes for internal site imaging. Therefore, PTOCT and OCT imaging could potentially be taken from within the same probes used to illuminate the tumor in order to identify the nanoparticle distribution and subsequent tumor cell death, respectively. This could allow researchers to not only better understand treatment efficacy in the clinical setting, but could also allow for real time alterations to laser irradiance dosing strategy to ensure complete tumor destruction.

6.4 References

1. J. M. Tucker-Schwartz, K. R. Beavers, W. W. Sit, A. T. Shah, C. L. Duvall, and M. C. Skala, "In vivo imaging of nanoparticle delivery and tumor microvasculature with multimodal optical coherence tomography," Biomed Opt Express **5**, 1731-1743 (2014).

2. J. M. Tucker-Schwartz, T. Hong, D. C. Colvin, Y. Xu, and M. C. Skala, "Dual-modality photothermal optical coherence tomography and magnetic-resonance imaging of carbon nanotubes," Opt Lett **37**, 872-874 (2012).

3. J. M. Tucker-Schwartz, T. A. Meyer, C. A. Patil, C. L. Duvall, and M. C. Skala, "In vivo photothermal optical coherence tomography of gold nanorod contrast agents," Biomed Opt Express **3**, 2881-2895 (2012).

4. J. M. Tucker-Schwartz, M. Lapierre-Landry, C. A. Patil, and M. C. Skala, "Photothermal optical lock-in optical coherence tomography for in vivo imaging " Biomed Opt Express **6**, 2268-2282 (2015).

5. P. C. Li, C. R. Wang, D. B. Shieh, C. W. Wei, C. K. Liao, C. Poe, S. Jhan, A. A. Ding, and Y. N. Wu, "In vivo photoacoustic molecular imaging with simultaneous multiple selective targeting using antibody-conjugated gold nanorods," Opt Express **16**, 18605-18615 (2008).

6. E. C. Dreaden, L. A. Austin, M. A. Mackey, and M. A. El-Sayed, "Size matters: gold nanoparticles in targeted cancer drug delivery," Therapeutic delivery **3**, 457-478 (2012).

7. M. J. C. vanGemert, G. W. Lucassen, and A. J. Welch, "Time constants in thermal laser medicine .2. Distributions of time constants and thermal relaxation of tissue," Phys Med Biol **41**, 1381-1399 (1996).

8. A. Agrawal, S. Huang, A. Wei Haw Lin, M. H. Lee, J. K. Barton, R. A. Drezek, and T. J. Pfefer, "Quantitative evaluation of optical coherence tomography signal enhancement with gold nanoshells," J Biomed Opt **11**, 041121 (2006).

9. J. Fang, H. Nakamura, and H. Maeda, "The EPR effect: Unique features of tumor blood vessels for drug delivery, factors involved, and limitations and augmentation of the effect," Advanced drug delivery reviews **63**, 136-151 (2011).

10. A. K. Iyer, G. Khaled, J. Fang, and H. Maeda, "Exploiting the enhanced permeability and retention effect for tumor targeting," Drug Discov Today **11**, 812-818 (2006).

11. J. A. Schwartz, A. M. Shetty, R. E. Price, R. J. Stafford, J. C. Wang, R. K. Uthamanthil, K. Pham, R. J. McNichols, C. L. Coleman, and J. D. Payne, "Feasibility Study of Particle-Assisted Laser Ablation of Brain Tumors in Orthotopic Canine Model," Cancer Res **69**, 1659-1667 (2009).

12. G. von Maltzahn, J. H. Park, A. Agrawal, N. K. Bandaru, S. K. Das, M. J. Sailor, and S. N. Bhatia, "Computationally guided photothermal tumor therapy using long-circulating gold nanorod antennas," Cancer Res **69**, 3892-3900 (2009).

13. A. M. Gobin, M. H. Lee, N. J. Halas, W. D. James, R. A. Drezek, and J. L. West, "Near-infrared resonant nanoshells for combined optical imaging and photothermal cancer therapy," Nano Lett **7**, 1929-1934 (2007).

14. S. K. Libutti, G. F. Paciotti, A. A. Byrnes, H. R. Alexander, Jr., W. E. Gannon, M. Walker, G. D. Seidel, N. Yuldasheva, and L. Tamarkin, "Phase I and pharmacokinetic studies of CYT-6091, a novel PEGylated colloidal gold-rhTNF nanomedicine," Clinical cancer research : an official journal of the American Association for Cancer Research **16**, 6139-6149 (2010).

15. R. K. Jain, L. L. Munn, and D. Fukumura, "Dissecting tumour pathophysiology using intravital microscopy," Nat Rev Cancer **2**, 266-276 (2002).

16. M. R. Junttila and F. J. de Sauvage, "Influence of tumour micro-environment heterogeneity on therapeutic response," Nature **501**, 346-354 (2013).

17. T. Hoshida, N. Isaka, J. Hagendoorn, E. di Tomaso, Y. L. Chen, B. Pytowski, D. Fukumura, T. P. Padera, and R. K. Jain, "Imaging steps of lymphatic metastasis reveals that vascular endothelial growth factor-C increases metastasis by increasing delivery of cancer cells to lymph nodes: therapeutic implications," Cancer Res **66**, 8065-8075 (2006).

18. S. I. J. Ellenbroek and J. van Rheenen, "Imaging hallmarks of cancer in living mice," Nat Rev Cancer **14**, 406-418 (2014).

19. G. Y. Guan, R. Reif, Z. H. Huang, and R. K. K. Wang, "Depth profiling of photothermal compound concentrations using phase sensitive optical coherence tomography," J Biomed Opt **16**(2011).

20. M. S. Mahmud, D. W. Cadotte, B. Vuong, C. Sun, T. W. Luk, A. Mariampillai, and V. X. Yang, "Review of speckle and phase variance optical coherence tomography to visualize microvascular networks," J Biomed Opt **18**, 50901 (2013).

21. L. M. Peterson, S. Gu, M. W. Jenkins, and A. M. Rollins, "Orientation-independent rapid pulsatile flow measurement using dual-angle Doppler OCT," Biomed Opt Express **5**, 499-514 (2014).

22. N. P. Truong, M. R. Whittaker, C. W. Mak, and T. P. Davis, "The importance of nanoparticle shape in cancer drug delivery," Expert opinion on drug delivery **12**, 129-142 (2015).

23. Arnida, M. M. Janat-Amsbury, A. Ray, C. M. Peterson, and H. Ghandehari, "Geometry and surface characteristics of gold nanoparticles influence their biodistribution and uptake by macrophages," European journal of pharmaceutics and biopharmaceutics : official journal of Arbeitsgemeinschaft fur Pharmazeutische Verfahrenstechnik e.V **77**, 417-423 (2011).

24. W. H. De Jong, W. I. Hagens, P. Krystek, M. C. Burger, A. J. A. M. Sips, and R. E. Geertsma, "Particle size-dependent organ distribution of gold nanoparticles after intravenous administration," Biomaterials **29**, 1912-1919 (2008).

25. S. D. Perrault, C. Walkey, T. Jennings, H. C. Fischer, and W. C. W. Chan, "Mediating Tumor Targeting Efficiency of Nanoparticles Through Design," Nano Lett **9**, 1909-1915 (2009).

26. J. H. Baker, K. E. Lindquist, L. A. Huxham, A. H. Kyle, J. T. Sy, and A. I. Minchinton, "Direct visualization of heterogeneous extravascular distribution of trastuzumab in human epidermal growth factor receptor type 2 overexpressing xenografts," Clinical cancer research : an official journal of the American Association for Cancer Research **14**, 2171-2179 (2008).

27. A. Marusyk, V. Almendro, and K. Polyak, "Intra-tumour heterogeneity: a looking glass for cancer?," Nat Rev Cancer **12**, 323-334 (2012).

28. X. H. Huang, S. Neretina, and M. A. El-Sayed, "Gold Nanorods: From Synthesis and Properties to Biological and Biomedical Applications," Adv Mater **21**, 4880-4910 (2009).

29. J. Chen, F. Saeki, B. J. Wiley, H. Cang, M. J. Cobb, Z. Y. Li, L. Au, H. Zhang, M. B. Kimmey, X. Li, and Y. Xia, "Gold nanocages: bioconjugation and their potential use as optical imaging contrast agents," Nano Lett **5**, 473-477 (2005).

30. S. Barbosa, A. Agrawal, L. Rodriguez-Lorenzo, I. Pastoriza-Santos, R. A. Alvarez-Puebla, A. Kornowski, H. Weller, and L. M. Liz-Marzan, "Tuning size and sensing properties in colloidal gold nanostars," Langmuir **26**, 14943-14950 (2010).

31. L. Tang, T. M. Fan, L. B. Borst, and J. J. Cheng, "Synthesis and Biological Response of Size-Specific, Monodisperse Drug-Silica Nanoconjugates," ACS Nano **6**, 3954-3966 (2012).

32. X. M. Qian, X. H. Peng, D. O. Ansari, Q. Yin-Goen, G. Z. Chen, D. M. Shin, L. Yang, A. N. Young, M. D. Wang, and S. M. Nie, "In vivo tumor targeting and spectroscopic

detection with surface-enhanced Raman nanoparticle tags," Nat Biotechnol **26**, 83-90 (2008).

33. D. B. Kirpotin, D. C. Drummond, Y. Shao, M. R. Shalaby, K. Hong, U. B. Nielsen, J. D. Marks, C. C. Benz, and J. W. Park, "Antibody targeting of long-circulating lipidic nanoparticles does not increase tumor localization but does increase internalization in animal models," Cancer Res **66**, 6732-6740 (2006).

34. X. Huang, X. Peng, Y. Wang, Y. Wang, D. M. Shin, M. A. El-Sayed, and S. Nie, "A reexamination of active and passive tumor targeting by using rod-shaped gold nanocrystals and covalently conjugated peptide ligands," ACS Nano **4**, 5887-5896 (2010).

35. J. Stingl and C. Caldas, "Molecular heterogeneity of breast carcinomas and the cancer stem cell hypothesis," Nat Rev Cancer **7**, 791-799 (2007).

36. J. R. Conway, N. O. Carragher, and P. Timpson, "Developments in preclinical cancer imaging: innovating the discovery of therapeutics," Nat Rev Cancer **14**, 314-328 (2014).

37. M. de Jong, J. Essers, and W. M. van Weerden, "Imaging preclinical tumour models: improving translational power," Nat Rev Cancer **14**, 481-493 (2014).

38. Y. Akiyama, T. Mori, Y. Katayama, and T. Niidome, "The effects of PEG grafting level and injection dose on gold nanorod biodistribution in the tumor-bearing mice," J Control Release **139**, 81-84 (2009).

APPENDIX A

Dual Modality Photothermal Optical Coherence Tomography and Magnetic Resonance Imaging of Carbon Nanotubes

Tucker-Schwartz JM, Hong T, Colvin DC, Xu Y, Skala MC. "Dual modality photothermal optical coherence tomography and magnetic resonance imaging of carbon nanotubes." *Optics Letters*. 2012; 37(5):872-874.

A.1 Abstract

We demonstrate polyethylene glycol coated single-walled carbon nanotubes (CNTs) as contrast agents for both photothermal optical coherence tomography (OCT) and magnetic resonance imaging (MRI). Photothermal OCT was accomplished with a spectral domain OCT system with an amplitude modulated 750 nm pump beam using 10 mW of power, and T2 MR imaging was achieved with a 4.7 T animal system. Photothermal OCT and T2 MR imaging achieved sensitivities of nM concentrations to CNTs dispersed in amine terminated polyethylene glycol, thus establishing the potential for dual-modality molecular imaging with CNTs.

A.2 Introduction

Preclinical molecular imaging of cancer has the potential to increase the understanding of fundamental cancer biology, elucidate mechanisms of cancer treatment resistance, and increase effectiveness of drug candidates. Imaging tools used for studying the molecular expression of cancer include PET, SPECT, MRI, photoacoustics, and a number of optical imaging techniques. Each imaging method provides unique levels of sensitivity, depth penetration, and resolution. MRI can provide better spatial resolution anatomical images than nuclear imaging with the ability to extract additional functional information including blood flow and cellularity. However, MRI suffers from poor sensitivity to molecular contrast agents and poor resolution compared to microscopic optical imaging techniques.

Optical coherence tomography (OCT) holds a specialized niche in optical imaging, providing

structural information at high resolution (~1-10 μm) with deep optical image penetration (1-3 mm). Recently, functional imaging instrumentation and dynamic contrast agents have expanded the abilities of OCT to image paramagnetic contrast agents using magnetomotive displacements for combined OCT / MRI studies [1] and plasmon resonant particles both due to increased backscattering [2] and photon absorption [3-5]. Photothermal OCT of gold nanoparticle contrast agents has been demonstrated both *in vitro* [3, 4] and *ex vivo* [5], and offers a particularly sensitive method for detecting molecular expression in biological systems. Photothermal OCT uses an amplitude-modulated laser to perturb the temperature (and therefore index of refraction) surrounding a highly absorbing contrast agent. OCT is then used to locate the contrast agent in three dimensions, independent of the scattering background, with the potential for mapping contrast agent concentration quantitatively.

The depth of OCT imaging is shallow compared to MRI due to optical scattering and attenuation. Combining the strengths of MRI and OCT allows for both gross full body scale molecular expression as well as local cellular-resolution imaging at a site of interest (e.g. primary tumor). We present below the novel use of single-walled carbon nanotubes (CNTs) as inherent multi-modal imaging contrasts for use with both MRI and photothermal OCT.

CNTs are cylindrically assembled sheets of carbon atoms. In optics, due to efficient optical absorption and fluorescence at a range of near infrared wavelengths, CNTs have been used as both an imaging contrast agent [6, 7] as well as a phototherapy transducer for targeted destruction of cancer cells [8]. In MRI, CNTs have been demonstrated as T_2 spin dephasing contrast agents [9]. Of great importance for *in vivo* translation as a contrast, due to their unique size and aspect ratio, CNTs have been shown to efficiently target and enter cancer cells from intravenous injections, at 15% of the injected dose per gram, making them more promising vehicles for both targeted imaging and therapeutics than spherical contrasts including iron oxide nanoparticles [6, 10]. The surface

functionalization chemistry of CNTs for biological targeting is well established [11], CNT safety and circulation dynamics have been demonstrated for *in vivo* chronic animal studies [8, 10], and nanotubes can be filled with or coated in contrasts which increase their optical and MR contrast capabilities including ICG [7] and gadolinium [12], respectively. Here, we demonstrate the potential of CNTs as inherent optical absorption and magnetic resonance dual modality contrast agents with photothermal OCT and MRI, respectively.

A.3 Methods and Results

Single-walled CNTs (HiPCO), with a typical diameter of 1 nm and length of 100 to 400 nm, were noncovalently coated and dispersed in amine terminated polyethylene glycol (PEG) solution according to established protocols [11]. Amine terminated PEG was chosen as the surfactant due to its use in surface functionalization chemistry and impact in biocompatibility and circulation time, making the nanotubes analyzed in this paper the precursor to functionalized particles to be used in targeted biological applications. The optical extinction spectrum of the CNT sample was acquired with a spectrophotometer (Cary 5000) from 400 to 1350 nm (Fig 1(a)). Spectrophotometry indicated broadband visible and near infrared attenuation with sharp localized peaks, indicating CNTs were well dispersed and not aggregated in solution [13]. Liquid samples were prepared with concentrations ranging from 0 nM to 168 nM for analysis (calculated from mass concentration assuming 150 nm length and 170 kDa molecular weight [6]), with mass concentration of the stock solution assessed by optical density at 808 nm with extinction coefficient of 0.0465 l mg $^{-1}$ cm^{-1} [11].

A commercial OCT system (Bioptigen Inc.) was altered for photothermal imaging. The imaging system contained an 860 nm center wavelength, 51 nm bandwidth, super luminescent diode source (axial resolution ~ 6.4 μm in air), with 8.5 μm lateral resolution and 100 μs integration time. A titanium sapphire laser served as the photothermal beam, which was fiber coupled and integrated

with the OCT system via a 50/50 fiber coupler (Fig. A.1(b)). The photothermal beam was tuned to 750 nm, and amplitude modulated with a 50% duty cycle square wave at 100 Hz with a mechanical chopper, with 10 mW of power on the sample. OCT and photothermal spot sizes were roughly equal. 1000 consecutive temporal scans were acquired for each A-scan during photothermal beam amplitude modulation. Phase (Fig. A.2(a)) and magnitude data was extracted from the interference data with a chirp-Z transform. Using a custom matlab file, phase data was processed with 5th order polynomial background subtraction to account for signal drift, windowed, zero padded, and Fourier transformed in the temporal direction (Fig. A.2(b)). The photothermal signal was set as the FFT magnitude at the chopping frequency (100 Hz), and the background signal was calculated as the mean magnitude of the next highest 50 Hz of frequencies.

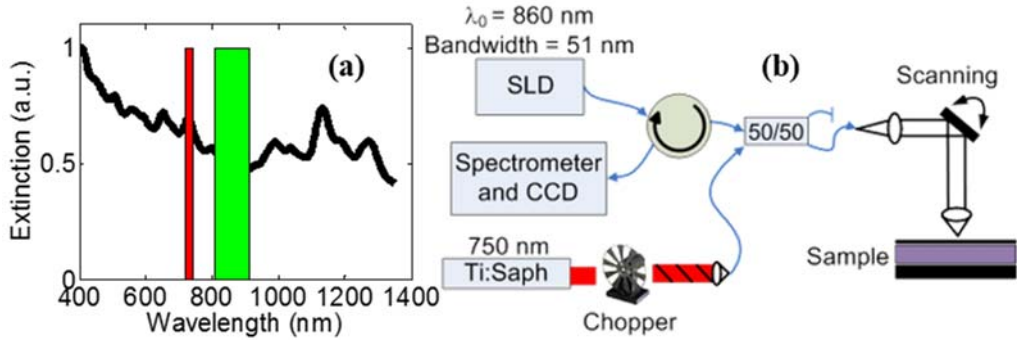

Fig. A.1. Contrast agents and instrumentation. (a) Vis-NIR attenuation spectrum of CNTs. With photothermal laser wavelength (red) and OCT imaging laser spectrum (green). (b) Photothermal OCT instrumentation used for imaging (SLD = super luminescent diode source).

To test for photothermal OCT signal linearity and sensitivity, 5 µl of CNT sample was placed into a PDMS well (~150 µm thick) on a microscope slide, covered with a coverslip, and imaged with common path OCT. The photothermal OCT signal was acquired at the base of the sample. The photothermal signal was linear with concentration (r^2 = 0.99), and the photothermal signal was significantly higher in the lowest concentration sample (10 nM) compared to a scattering control of polystyrene microspheres with μ_s = 100 cm^{-1} ($p<0.05$, Fig. A.2(c)). It is important to note that the

photothermal SNR increases with irradiance and chopping period, therefore the imaging sensitivity could increase with increased irradiance or decreased chopping frequency [4].

The ability of CNTs to alter native MRI contrast was assessed with a commercial 4.7 T horizontal bore animal scanner (Varian Inc.) by performing quantitative T_1 and T_2 relaxometry (Fig. A.2(d)). 200 µl CNT samples in NMR tubes were placed into a standard small animal RF coil (38 mm diameter, 33 mm length) and imaged in a 32 × 32 mm field of view with 250 µm in plane resolution and 1.5 mm slice thickness. T_1-weighted images were acquired using an inversion recovery flash imaging sequence with 5000 ms repetition time, 2.4 ms echo time, 8 degree flip angle, 16 acquisitions per inversion, and inversion times of 50, 200, 800, 2000, and 4500 ms. T_2-weighted images were collected with a multiple echo spin echo pulse sequence using 2000 ms repetition time, 6 acquisitions, 8 ms echo spacing, and 32 echoes starting at 8 ms. T_1 and T_2 maps were calculated by fitting the signal at each voxel across time to a mono-exponential model. R_1 ($\equiv 1/T_1$) and R_2 ($\equiv 1/T_2$) were calculated to generate linear concentration dependent relaxivity curves. The relaxivity (slope of the concentration curve) of CNTs was 19,945 s^{-1} mM^{-1} for T_2 contrast and 1,152 s^{-1} mM^{-1} for T_1 contrast. In MRI, *in vivo* sensitivity is a function of SNR and relaxivity of the tissues being imaged, although the concentration necessary to change the baseline relaxivity by 10% is a good estimate of *in vivo* sensitivity [14]. Assuming a standard tissue T_2 between 50 and 100 ms, the *in vivo* concentration of CNTs to induce a 10% change in signal, using T_2 imaging, is between 50 and 100 nM.

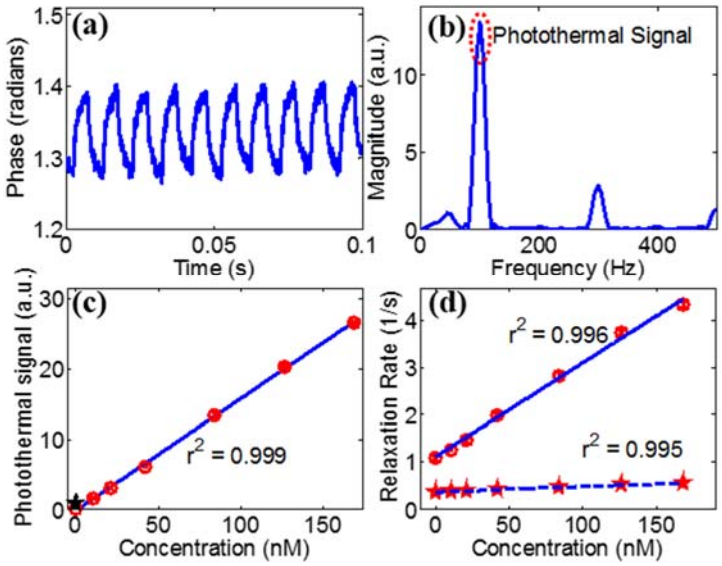

Fig. A.2. Photothermal and MRI signal analysis. (a) Example temporal phase data acquired from the base of 84 nM CNT phantom during photothermal modulation. (b) Fourier transform of processed phase data. (c) Photothermal signal as a function CNT concentration. The black star indicates the photothermal signal of a scattering control (μ_s = 100 cm^{-1}). (d) MRI relaxivity curves of carbon nanotubes for both T_1 (dashed) and T_2 contrast (solid).

Two dimensional images of solid phantoms were also acquired. Low gelling temperature agarose was mixed with either water as a negative control, or CNTs to create 2% agarose gels with either 0 or 84 nM nanotube concentrations. The CNT sample was added to two 1 mm capillary tubes via capillary action and allowed to cool at 4 degrees C while covered in parafilm to avoid water evaporation. The capillary tubes were then placed across a 15 ml falcon tube through drill holes and sealed. One tube was placed near the surface of the phantom while the other tube was placed deeper in the sample. After gelling, the majority of the glass surrounding the superficial capillary tube was removed to leave a bare cylindrical agarose gel of CNTs. The 15 ml tube was then filled with 2% agarose solution until covering the superficial CNT gel, and was allowed to gel at room temperature during a 10 minute 1000 rpm centrifugation to remove air bubbles.

The phantom was imaged with photothermal OCT using the system in Fig. A.1(b), with the addition of a reference arm mirror. A 1.2 mm lateral B-scan was imaged, and the final photothermal

image was average filtered to decrease noise. The same phantom was then imaged with MRI, using the instrument described above. A 100 μm lateral resolution, 1.5 mm coronal slice was imaged with T_2 weighting using a multiple spin-echo pulse sequence with a repetition time of 2 s, 10 ms echo spacing, with 40 echoes, and 6 acquisitions. Phantom images (Fig. A.3) confirmed both the capabilities and limitations of each imaging modality. Photothermal imaging was able to discriminate the agarose/CNT cylinder from the scattering agarose background, while the OCT magnitude image could not (Fig. A.3(a), A.3(b)). PT-OCT also allowed for high resolution targeted imaging, although to a limited depth (1.5 mm). The MR image of the phantom at the 50 ms echo indicates significant signal differences between the agarose and agarose/CNT regions of the image (Fig. A.3(c)) at all depths, although with in plane resolution two orders of magnitude less than OCT. The nanotube contrast effects with MRI are slightly higher in the image than expected, which is due to an increase in agarose concentration from water evaporation in the capillary tube sample.

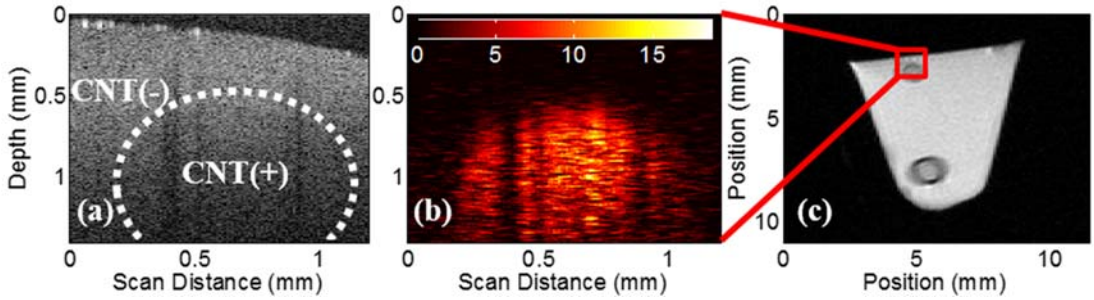

Fig. A.3. PTOCT and MRI imaging of phantoms. (a) OCT magnitude image of three dimensional agarose phantom, note a lack of contrast or any visual confirmation of the presence of CNTs. CNT(+) (~84 nM) and CNT(-) regions are highlighted. (b) Photothermal OCT of the same field of view, revealing the cylindrical CNT gel inclusion. Photothermal signal is in arbitrary units. (c) Full cross sectional MRI image (50 ms echo time) of the phantom revealing both the superficial and deep CNT gel phantoms. Only the deep nanotube phantom has a capillary tube surrounding it. The dark ring surrounding the lower inclusion is due to the glass capillary tube.

A.4 Discussion

We have demonstrated the ability of both MRI and photothermal OCT to distinguish CNTs from background at nM concentrations. Importantly, this concentration is approximately equivalent

to that demonstrated for marking cell receptors with systemic *in vivo* delivery of CNTs [6], and much less than the theoretical [2] and *in vitro* [15] targeting capabilities of CNTs. This study has shown the ability of a common contrast agent, which is an efficient biological targeting agent, to be sensitive to both functional OCT and MR imaging, thereby enabling multi-scale multi-modality preclinical molecular imaging.

A.5 Acknowledgements

This work was supported by funding from the NIH (grant R00 CA142888) and NSF (grant EECS-1055852).

A.6 References

1. R. John, R. Rezaeipoor, S. G. Adie, E. J. Chaney, A. L. Oldenburg, M. Marjanovic, J. P. Haldar, B. P. Sutton, and S. A. Boppart, "In vivo magnetomotive optical molecular imaging using targeted magnetic nanoprobes," Proc Natl Acad Sci U S A **107**, 8085-8090 (2010).

2. A. Agrawal, S. Huang, A. Wei Haw Lin, M. H. Lee, J. K. Barton, R. A. Drezek, and T. J. Pfefer, "Quantitative evaluation of optical coherence tomography signal enhancement with gold nanoshells," J Biomed Opt **11**, 041121 (2006).

3. M. C. Skala, M. J. Crow, A. Wax, and J. A. Izatt, "Photothermal optical coherence tomography of epidermal growth factor receptor in live cells using immunotargeted gold nanospheres," Nano Lett **8**, 3461-3467 (2008).

4. D. C. Adler, S. W. Huang, R. Huber, and J. G. Fujimoto, "Photothermal detection of gold nanoparticles using phase-sensitive optical coherence tomography," Opt Express **16**, 4376-4393 (2008).

5. C. Zhou, T. H. Tsai, D. C. Adler, H. C. Lee, D. W. Cohen, A. Mondelblatt, Y. Wang, J. L. Connolly, and J. G. Fujimoto, "Photothermal optical coherence tomography in ex vivo human breast tissues using gold nanoshells," Opt Lett **35**, 700-702 (2010).

6. A. De la Zerda, C. Zavaleta, S. Keren, S. Vaithilingam, S. Bodapati, Z. Liu, J. Levi, B. R. Smith, T. J. Ma, O. Oralkan, Z. Cheng, X. Chen, H. Dai, B. T. Khuri-Yakub, and S. S. Gambhir, "Carbon nanotubes as photoacoustic molecular imaging agents in living mice," Nat Nanotechnol **3**, 557-562 (2008).

7. A. de la Zerda, Z. Liu, S. Bodapati, R. Teed, S. Vaithilingam, B. T. Khuri-Yakub, X. Chen, H. Dai, and S. S. Gambhir, "Ultrahigh sensitivity carbon nanotube agents for photoacoustic molecular imaging in living mice," Nano Lett **10**, 2168-2172 (2010).

8. H. K. Moon, S. H. Lee, and H. C. Choi, "In vivo near-infrared mediated tumor destruction

by photothermal effect of carbon nanotubes," ACS Nano **3**, 3707-3713 (2009).

9. J. S. Ananta, M. L. Matson, A. M. Tang, T. Mandal, S. Lin, K. Wong, S. T. Wong, and L. J. Wilson, "Single-Walled Carbon Nanotube Materials as T(2)-Weighted MRI Contrast Agents," J Phys Chem C **113**, 19369-19372 (2009).

10. Z. Liu, W. Cai, L. He, N. Nakayama, K. Chen, X. Sun, X. Chen, and H. Dai, "In vivo biodistribution and highly efficient tumour targeting of carbon nanotubes in mice," Nat Nanotechnol **2**, 47-52 (2007).

11. Z. Liu, S. M. Tabakman, Z. Chen, and H. Dai, "Preparation of carbon nanotube bioconjugates for biomedical applications," Nat Protoc **4**, 1372-1382 (2009).

12. A. M. Tang, J. S. Ananta, H. Zhao, B. T. Cisneros, E. Y. Lam, S. T. Wong, L. J. Wilson, and K. K. Wong, "Cellular uptake and imaging studies of gadolinium-loaded single-walled carbon nanotubes as MRI contrast agents," Contrast Media Mol I **6**, 93-99 (2011).

13. M. J. O'Connell, S. M. Bachilo, C. B. Huffman, V. C. Moore, M. S. Strano, E. H. Haroz, K. L. Rialon, P. J. Boul, W. H. Noon, C. Kittrell, J. Ma, R. H. Hauge, R. B. Weisman, and R. E. Smalley, "Band gap fluorescence from individual single-walled carbon nanotubes," Science **297**, 593-596 (2002).

14. J. C. Gore, T. E. Yankeelov, T. E. Peterson, and M. J. Avison, "Molecular imaging without radiopharmaceuticals?," J Nucl Med **50**, 999-1007 (2009).

15. B. D. Holt, K. N. Dahl, and M. F. Islam, "Quantification of Uptake and Localization of Bovine Serum Albumin-Stabilized Single-Wall Carbon Nanotubes in Different Human Cell Types," Small (2011).